X rays from quasimolecules

R. Anholt

Department of Physics, Stanford University, Stanford, California 94305

In slow heavy-ion—atom collisions, inner-shell electrons with velocities larger than the projectile velocity form diatomic molecular orbitals around the projectile and target nuclei. If a vacancy exists in one of these orbitals, it can decay at some point during collision, emitting an x ray characteristic of the molecular transition energy at that internuclear distance. Since the projectile-target internuclear distance varies during the collision, x-ray continua are seen, which for $1s\sigma$ molecular-orbital x rays (transitions to vacancies in the lowest $1s\sigma$ orbital) stretch toward the united-atom K-shell binding energy. This paper reviews the theory of and the experimental evidence for molecular-orbital x-ray emission. A historical overview of the development of these studies is given, showing how the theory of quasimolecular x-ray emission has evolved from a semiclassical quasistatic model to a general dynamic theory, including the Coriolis coupling between molecular orbitals making up the initial and final states. X-ray cross section, angular distribution, and other measurements are discussed, and their impact on the development of the theory of molecular-orbital x-ray emission is illustrated.

CONTENTS

List of Symbols and Abbreviations 995
A. Abbreviations 995
B. Symbols 996
I. Introduction 996
II. Historical Overview 997
III. Theories of Molecular-Orbital X-ray Emission 1001
A. The quasistatic approximation 1001
B. Dynamic theories 1002
1. Separation of one- and two-collision MO x-ray emission 1002
2. The stationary-phase approximation 1004
C. The angular distribution of molecular-orbital x rays 1005
1. General theory 1005
2. Two-collision $1s\sigma$ MO x-ray production 1006
3. Comparison with previous theories 1007
D. Wave functions and matrix elements 1007
1. Methods of solving the molecular Schrödinger equation 1007
2. Correlation diagrams 1010
3. Molecular x-ray transition rates 1012
IV. X-ray Cross-Section Measurements 1013
A. Measuring continuum radiation 1013
B. Other radiative processes 1015
1. Overview 1015
2. Nucleus-nucleus bremsstrahlung 1016
3. Secondary-electron bremsstrahlung 1016
4. Primary bremsstrahlung 1017
5. γ-ray background 1018
6. Radiative electron capture 1018
C. $1s\sigma$ molecular-orbital x rays 1019
1. Two-collision MO x-ray production 1019
2. A scaling law for MO x-ray production 1021
3. One-collision MO x-ray production 1022
4. MO x-ray tails 1023
D. $2p\sigma$ molecular-orbital x rays 1024
1. Near-symmetric collisions 1024
2. Asymmetric collisions 1027
E. L molecular-orbital x rays 1027
F. M molecular-orbital x rays 1028
V. The Angular Distribution of Molecular-Orbital X Rays 1031
A. Doppler-velocity measurements 1031
B. Origin of the $1s\sigma$ molecular-orbital x-ray anisotropy 1032
1. Two-collision MO x rays 1032
2. The perfect electron-slip model 1033
C. Scaling laws and the spectroscopy of molecular-orbital x rays 1034
D. One-collision molecular-orbital x-ray anisotropies 1035
E. Other theories of molecular-orbital x-ray anisotropies 1036
1. Induced MO x-ray transitions 1036
2. Radiative electron capture to molecular orbitals (RECMO) 1037
3. The kinematic dipole model 1037
F. $2p\sigma$ molecular-orbital x-ray anisotropies 1037
G. L and M molecular-orbital x-ray anisotropies 1039
VI. Other Measurements 1040
A. The impact-parameter dependence of molecular-orbital x-ray production 1040
1. Quasimolecular interferences 1040
2. Solid-target measurements 1041
B. The azimuthal angular distribution 1043
C. Linear polarization measurements 1044
D. Molecular-orbital x-ray separated-atom K x-ray coincidences 1044
E. Compound-nucleus x-ray emission 1045
F. Molecular Auger electron emission 1046
VII. Conclusions 1048
Acknowledgments 1049
References 1049

LIST OF SYMBOLS AND ABBREVIATIONS

A. Abbreviations

AO	atomic orbital
BIB	beam-induced background
c.m.	center of (nuclear) mass
CN	compound nucleus
HF	Hartree-Fock
lab	laboratory
MO	molecular orbital
NNB	nucleus-nucleus bremsstrahlung
PB	primary bremsstrahlung
REC	radiative electron capture
RECMO	radiative electron capture to molecular orbitals
RHFS	relativistic Hartree-Fock-Slater

SA	separated atom
SEB	secondary-electron bremsstrahlung
UA	united atom
TCD	two-center Dirac
VSM	variable screening model

B. Symbols

a_{KL}	K radius of the lighter collision partner
A_0	alignment parameter
b	collision impact parameter
$D_{if}(R)$	dipole transition matrix element
$D_{if}(\omega)$	its Fourier transform
E_x	x-ray energy
E_c	c.m. nuclear kinetic energy
$\mathbf{k}$	photon momentum
m	electron mass
n_2	target-atom density
q	$\omega_0 a_{KL}/v$, the scaled collision velocity
$\mathbf{r}$	the electron coordinate
$\mathbf{R}$	the internuclear coordinate
t	time
v	ion velocity
v_K	the SA K electron velocity
Z_1	the projectile atomic number
Z_2	the target atomic number
Z_L	the atomic number of the lighter collision partner
Z_H	the atomic number of the heavier collision partner
Z_u	the UA atomic number
α	fine-structure constant
β	ratio of the ion velocity to the speed of light
Γ	the total radiative and Auger decay rate
ζ	Z_H/Z_L
$\lambda_{if}(R)$	the MO x-ray transition rate
η	the MO x-ray anisotropy, $\sigma(90°)/\sigma(0°)-1$
η_φ	the azimuthal MO x-ray anisotropy
θ	the photon emission angle from the beam axis
Θ	the projectile scattering angle or the angle between $\mathbf{R}$ and $\mathbf{v}$
$\Psi(t)$	the total wave function
ω	x-ray emission frequency
ω_0	characteristic frequency in the scaling laws for $1s\sigma$ or $2p\sigma$ MO x-ray production
ν	ω/ω_0
$\chi(\mathbf{r},\mathbf{R})$	molecular electronic wave function

I. INTRODUCTION

In recent years, the molecular model of ion-atom collisions has been widely applied to analyze inner-shell vacancy production and electronic excitation (Kessel and Fastrup, 1973; Meyerhof and Taulbjerg, 1977; Mokler and Folkmann, 1978; Vincent, 1985). In part this development has been furthered by the application of accelerators formerly used exclusively by nuclear physicists to atomic collision physics studies. Despite the fact that very energetic particles, up to 2 GeV, are often available from these machines, the velocities of heavy projectiles are usually smaller than the velocities of the inner-shell electrons. Therefore, in the relatively slow collisions studied, the electron clouds around the projectile and target nuclei are perturbed by the presence of the additional nuclear charge: the projectile nucleus distorts the target atom, and the target nucleus distorts the projectile ion. The most convenient way of describing this distortion is by assuming the inner-shell electrons form diatomic molecular orbitals (MO's) around the projectile and target nuclei.

One of the great successes of the molecular model is the explanation of the very pronounced structure seen in projectile and target K x-ray production cross sections plotted against target atomic number Z_2 for constant projectile atomic number Z_1 and velocity v (Kubo *et al.*, 1973; Meyerhof, 1973; Meyerhof *et al.*, 1976). Peaks seen in the x-ray cross sections where Z_1 is approximately equal to Z_2 and $Z_2/2$ are due to the sharing of inner-shell vacancies created in promoted MO's [MO's having a lower united-atom (UA) than separated-atom (SA) binding energy] between the projectile K shell and the target K and L shells. This qualitative explanation is widely accepted, and the K-K vacancy sharing mechanism is understood quantitatively (Meyerhof, 1973). The quantitative understanding of some molecular excitation mechanisms is presently better understood than others (Meyerhof *et al.*, 1977).

Most collision physics studies measure the products of a collision; K, L, and M x rays characteristic of the separated target and projectile atoms indicate that vacancies are made, and that electrons are excited during the collision. An implication of the molecular model is the possibility of observing x rays created during the collision. If a vacancy exists in an inner-shell MO, an electron from a higher-lying MO can fill it, emitting an x ray characteristic of the molecular energy-level separation at that internuclear distance. Unlike MO's of nearly stationary molecules (neglecting vibrations and rotations), MO's created during the collision are highly transitory; the internuclear distance, and therefore the molecular energy-level separation, changes continuously, hence MO emission is manifested by x-ray continua.

One of the major objectives of the study of quasimolecular x-ray emission is the deduction of spectroscopic information, especially for superheavy quasimolecules (MacDonald *et al.*, 1973; Müller *et al.*, 1975; Stoller *et al.*, 1977,1980). For transitions to vacancies in the lowest $1s\sigma$ MO, the continua should stretch as far as the UA $K\alpha$ or $K\beta$ transition energy, suggesting that these energies could be obtained from careful measurements of continuum end points. The discovery and elucidation of collision broadening of the MO x-ray continua voided this proposal, however (Macek and Briggs, 1974). Subsequent measurements found that MO x-ray emission is anisotropic, and that the spectrum of the anisotropy coefficient peaks near the UA $K\alpha$ transition energy (Greenberg

et al., 1974). Theory confirmed this observation, and scaling laws confirmed that independent of the projectile and target charge over a limited range of relative velocities, the peak will always occur at the same place relative to the UA $K\alpha$ energy (Anholt, 1978a,1978b). However, theory also predicted that (1) the scaling laws break down for superheavy quasimolecules, and (2) the anisotropy is nearly zero for those collisions. These predictions were confirmed for Pb + Pb collisions (Stoller *et al.*, 1980). Recently, a new method has been used for obtaining molecular transition energies from measurements of the interference between MO x-ray emission on the incoming and outgoing parts of the collision (Tserruya *et al.*, 1983; Schuch *et al.*, 1985; Meron *et al.*, 1985). Although this method has been successfully applied to Cl + Ar collisions, the difficulty of creating incoming vacancies in very high-Z projectiles may limit its applicability in determining spectroscopic quantities in superheavy quasimolecules.

More important than the application of quasimolecular emission studies to spectroscopy is the information obtainable about atomic collision mechanisms. An x ray emitted during the collision carries information about the state of the molecule at the point of emission. The interpretation of this information is difficult because its clarity is fundamentally limited by collision broadening considerations. However, these studies have revealed important insights into heavy-ion—atom collisions. We can deduce which electrons form MO's, and under what conditions the MO's follow the rotation of the internuclear axis. This kind of information about the evolution of an atomic collision is available from one other kind of measurement, that of the effects associated with time delays due to the formation of nuclear composite systems (Anholt, 1985).

There are two other ways a vacancy in a MO can decay: by Auger emission in most many-electron collisions (Liesen *et al.*, 1982) and, in the special case of U + U and other collisions where the UA charge exceeds 170, by spontaneous positron emission (Müller, 1976). If the binding energy of the $1s\sigma$ MO exceeds $2mc^2$, a vacancy in that orbital can decay by capturing an electron from the vacuum, leaving an observable positron. Just as MO x-ray continua are expected, a continuum positron spectrum is also predicted, and has been observed (Bokemeyer *et al.*, 1983; Kienle, 1983). Recently, however, positron peaks possibly indicating the formation of long-lived ($>10^{-19}$ sec) superheavy nuclear quasimolecules have been observed (Bokemeyer *et al.*, 1983; Kienle, 1983). This review, however, is limited to a discussion of quasimolecular x-ray and Auger electron emission, the subject of positron emission having been discussed in several other review articles (Müller, 1976; Reinhart *et al.*, 1980; Greiner and Hamilton, 1980; Backe and Müller, 1985).

One of the most useful things a paper of this scope can do is to review such studies from a historical perspective. This is particularly valuable in the case of quasimolecular x-ray emission, where a number of incorrect experimental claims and theories in the early literature require disposal or at least clarification. Section II provides a historical overview, which briefly touches on the intellectual foundations, but defers the discussion and elaboration of some ideas to later sections. Section III outlines the theory of MO x-ray emission, beginning with the simplest semiclassical quasistatic theory of MO x-ray emission, and evolving toward the general theory of emission by a transient molecule. Aside from noting the relationships between various theories, we postpone the discussion of the theoretical predictions until later sections where we compare them with measurements of MO x-ray cross sections (Sec. IV), angular distributions (Sec. V), and other quantities (Sec. VI).

II. HISTORICAL OVERVIEW

The search for MO x-ray emission could have commenced as early as 1931, when Mott (1931) formulated the method of perturbed stationary states for electronic excitation in slow ion-atom collisions. Mott realized that if atomic electrons travel much faster than the projectile, they could adjust their motion to the presence of the other nucleus, so the appropriate basis wave function for calculating excitation processes should approximate a diatomic MO around the projectile and target nuclei. This model was first used to calculate charge exchange processes in H and He collisions, and was used subsequently in a number of other calculations (Mott and Massey, 1965).

As experimenters began studying collisions between more complicated ions and atoms, correlation diagrams of

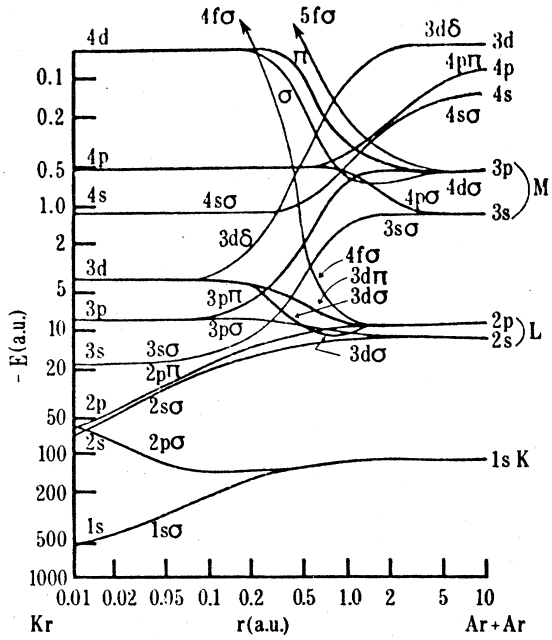

FIG. 1. Diabatic molecular level diagram for Ar+Ar collisions, as presented by Fano and Lichten (1965). The energies for large internuclear distance R (here marked r) are the atomic levels of Ar, and for small R the energy levels are the atomic levels of the combined atom, Kr.

the type calculated by quantum chemists (Mulliken, 1928) were introduced to interpret features seen in excitation cross sections. Correlation diagrams suggested pathways for electronic excitation; e.g., $1s$ to $2p$ excitation occurs due to the degeneracy at close internuclear distances of the $2p\sigma$ (correlating to the $1s$ orbital at infinite internuclear distance) and the $2p\pi$ MO (correlating to the $2p$ orbital). However, as heavy-ion—atom experiments progressed, it soon became apparent that the quantum chemists' adiabatic correlation diagrams were inadequate because some expected degeneracy-mediated transitions failed to occur. A significant breakthrough occurred with the introduction by Lichten (Fano and Lichten, 1965; Lichten, 1967; Barat and Lichten, 1972) of the diabatic correlation diagram (Fig. 1). In an adiabatic diagram, electrons choose the path of lowest energy at any crossing, but in a diabatic diagram electrons choose the path that preserves the orbital symmetry.

Given the widespread use of MO correlation diagrams to explain inner-shell excitation in ion-atom collisions (see reviews from that period by Kessel, 1969, and Garcia *et al.*, 1973), it is not surprising that attention turned to the possibility of x-ray transitions into inner-shell vacancies created in MO's during collisions. Molecular-orbital x-ray studies began in 1972 with the publication of a paper by Saris *et al.* (1972) reporting the observation of 0.5-keV to 1.5-keV noncharacteristic continuum x-ray emission in Ar + Ar collisions (Fig. 2).

In retrospect, it is surprising that the paper of Saris *et al.* triggered so much attention, because the measurement reported was difficult to interpret and required several leaps in understanding. First, the measurements were not made with Ar targets, but with Si targets. Atoms of Ar build up in the target as the result of ion implantation during the course of the measurements. The distinction between x-ray emission in collisions of Ar + Si and Ar + implanted Ar was consequently a major concern. Second, Saris *et al.* proposed that the continuum x-ray emission is due to the radiative filling of vacancies in the $2p\pi$ MO during the collision. MO x-ray emission with these energies is not simple to interpret, because of possible contributions from $2s\sigma$ and $3d\sigma$ x-ray emission, and because of the strong $2p\sigma$-$2p\pi$ rotational coupling. Theorists have still not attempted calculations of this particular MO x-ray emission. Third, a two-collision mechanism was introduced to explain the production of these x rays. An Ar $2p$ vacancy is made in a collision with an Ar or Si atom, which lives long enough to enter the $2p\pi$ MO in a second collision, where it radiates. Multiple-collision mechanisms in solid targets are presently well understood (e.g., Gray *et al.*, 1976; Meyerhof *et al.*, 1977), having been observed in many instances in ion-atom collisions. The first indication of the two-collision mechanism for the production of x rays in collisions where the molecular model is applicable appeared later in that year (Macek *et al.*, 1972). Finally, there was the question of the shape of the continuum seen by Saris *et al.* A broad peak was seen because the low-energy side (<0.6 keV) of the continuum emission was cut off due to x-ray attenuation by the window on the x-ray detector (Briggs, 1974). With higher-energy Ar ions the continuum extends to larger x-ray energies and appears, due to the low-energy cutoff, to shift in position. Higher-energy Ar ions penetrate to closer internuclear distances, allowing, because the $2p\pi$ binding energy increases with decreasing internuclear distance, higher-energy continuum x rays to be emitted. The continuum end point could not be observed at high energies, though, because of the presence of Si K x rays at 1.74 keV.

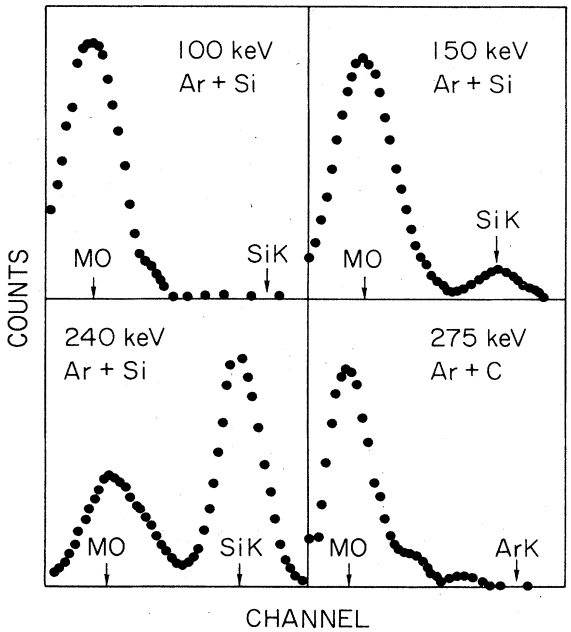

FIG. 2. Typical recorded spectra when argon ions are incident on thick silicon and carbon targets. The position of the peak thought to be due to L MO x-ray production in collisions of Ar + implanted Ar, and the positions of SA K x rays of Si and Ar, are shown (adapted from Saris *et al.*, 1972).

One reason why the work of Saris *et al.* produced great excitement and subsequent reevaluation, which continued for many years (MacDonald and Brown, 1972; Bissinger and Feldmann, 1973; Cairns *et al.*, 1974; Lurio *et al.*, 1975; see Sec. IV.E), was that other applications of quasimolecular emission were being proposed. Greiner and co-workers and Popov *et al.* (for a review see Zel'dovich and Popov, 1972, Müller, 1976, or Backe and Müller, 1985) had speculated on the possibility of spontaneous positron emission in superheavy atoms ($Z>170$) when the binding energy of the unfilled $1s$ orbital exceeds $2mc^2$. An electron-positron pair could be created, where the electron fills the K vacancy and the positron is emitted. Since stable $Z=170$ nuclei could not be made, attention turned to the molecular model for producing transiently a superheavy quasimolecule such as U + U, where the lowest $1s\sigma$ MO dives into the Dirac negative-energy sea (exceeds $2mc^2$ in binding energy) at close internuclear distances during the collision (Gerstein and Zel'dovich, 1969; Rafelski *et al.*, 1971). As the proposed U + U collision experiment could not be done until approximately

1977, when accelerators capable of producing the requisite ~1200-MeV uranium ions first became available, those interested in such measurements turned instead to MO x-ray emission studies, which could be done for many different ions and atoms using then existing accelerators.

If the end points of quasimolecular x-ray spectra could be measured accurately, information about united-atom (UA) binding energies in superheavy atoms could conceivably be obtained. There is precedent for this, which many nuclear physicists then turning to these studies were well aware of. For instance, β-decay Q values can be measured by extrapolating $\beta^{\pm}$ continuum spectra or internal-bremsstrahlung spectra to their end points. The idea of measuring superheavy binding energies was first apparent in the publication in 1972 of observations of quasimolecular M MO x-ray spectra in I + Au collisions with a UA charge Z_u equal to 132 (Mokler, Stein, and Armbruster, 1972; see Sec. IV.F). Although this work failed to produce an end-point energy for comparison with calculated superheavy binding energies (Fricke and Waber, 1973), it demonstrated the possibility of observing MO x rays in collisions with superheavy UA's.

A major drawback of the measurements of Saris *et al.* and Mokler *et al.* is that continuum x rays were observed in areas of high molecular level density; although Saris *et al.* singled out $2p\pi$ emission and Mokler *et al.* molecular $4f \rightarrow 3d$ transitions, many other nearby MO transitions could occur. Also, even if, for example, only $4f \rightarrow 3d$ transitions occurred, a theorist must account for the $4f\sigma$, $4f\pi$, $4f\delta$, and $4f\varphi$ initial MO's and the $3d\sigma$, $3d\pi$, and $3d\delta$ final MO's, a complicated calculational problem. Therefore, a significant milestone was reached when measurements of the simplest possible MO x-ray emission were made: transitions to vacancies in the lowest $1s\sigma$ MO (MacDonald *et al.*, 1973). This work produced the first evidence that MO x-ray end points would be difficult to interpret. MacDonald *et al.* measured continuum end-point energies while varying the beam bombarding energy in C + C collisions, thereby obtaining the $1s\sigma$ binding energy or a relevant MO x-ray transition energy as a function of the internuclear distance of closest approach $R_{\min}$ in a head-on collision. The small-R limit of this curve, however, exceeded the $1s$ binding energy of the UA Mg by ~300 eV. MacDonald *et al.* suggested that this reflected the existence of several additional L-shell vacancies in the quasimolecular system, which tend to shift to the $1s$ binding energy from the neutral-atom value, 1.4 keV in Mg, toward the one-electron value, 1.95 keV. However, it was not known at that time (nor is it known today) how to assess the binding energy in low-Z, highly ionized collisions. For this reason, attention was directed toward high-Z_u ion-atom collisions, where the energy levels are less sensitive to the charge state of the ions, and the MO x rays could conceivably be calculated with one-electron MO's. Meyerhof *et al.* (1973) reported the observation of $1s\sigma$ MO x rays in Br + Br collisions whose end points matched that expected for the UA ($Z=70$). This work was challenged by Davis and Greenberg (1974), most seriously on the grounds that the end-point energy is not a sufficient clue to the identity of the continuum x rays: first, because high-energy nucleus-nucleus bremsstrahlung (NNB) and x-ray continuum backgrounds (see Sec. IV.B) tend to obscure the end-point position, and second, because continua plotted on a semilogarithmic scale in the absence of such backgrounds show no apparent end point at all (Greenberg *et al.*, 1974).

Subsequently, attention turned to the proof of the quasimolecular identity of the observed continuum x rays. Several background continuum photon emission processes can contribute: NNB, secondary-electron bremsstrahlung (SEB), and primary bremsstrahlung (PB, also called radiative ionization; see Sec. IV.B). Also, the possibility of electronic pulse pileup and x-ray and γ-ray Compton scattering in the target, chamber, and experimental room must be taken into account. Meyerhof *et al.* (1974) attempted to calculate the absolute MO x-ray intensities and also the intensities of some of the simpler background processes using, in some cases, vastly oversimplified models. This approach may have been overly ambitious, because although two-collision MO x-ray production and NNB are calculable continua, most other processes have still not been quantitatively understood. Simultaneously, Müller and co-workers (Müller and Greiner, 1974; Müller, Smith, and Greiner, 1974,1975) suggested that an MO x-ray signature might be found in the angular distribution of the continuum radiation. Given the historical importance of photon angular distributions in nuclear physics, and the number of ex-nuclear physicists then involved in MO x-ray studies (Greiner, Meyerhof, Greenberg, Armbruster, and MacDonald, to name a few), it is hardly surprising that angular distribution measurements were made. Müller and co-workers formulated a theory of induced transitions between MO's due to the rotational current in the quasimolecule as the projectile passes by the target nucleus. It was suggested that the rotational-current radiative interaction gives anisotropic MO x-ray emission, while the usual electron current part gives approximately isotropic emission (see Sec. V.E.1). The rotational current is largest at the small impact parameters, where the highest-energy x rays are emitted; therefore the anisotropy should peak near the UA K x-ray transition energy, in agreement with the results of Greenberg *et al.* (1974) and Kraft *et al.* (1974).

A more basic proof of the quasimolecular origin of these x rays occurred to Meyerhof *et al.* (1975) as a consequence of these studies. The continuum x rays emitted in the laboratory have a forward-backward anisotropy due to the Doppler shift. Therefore, a measurement of the continuum x rays at 45° and 135° provides a measure of the velocity of the emitting system, which is required to be the center-of-mass (c.m.) velocity for MO x rays. Several measurements of the Doppler shift of continuum x rays found a c.m. emitter velocity (see Sec. V.A).

Meanwhile, substantial progress was made toward calculating $1s\sigma$ molecular x-ray emission. Briggs (1974) and Meyerhof *et al.* (1974) used a quasistatic model of two-

collision MO x-ray emission (Sec. III.A), predicting an x-ray continuum end point at the UA $K\alpha$ or $K\beta$ transition energy. The exponential falloff beyond the expected UA limit of the MO x-ray spectra was explained by Macek and Briggs (1974), who applied the Fourier-transform method of Weisskopf (1933) to calculate the dynamic collision broadening of MO x rays (Sec. III.B). They derived a simple equation for the intensity falloff beyond the UA limit, which was subsequently compared to much data by Betz *et al.* (1975,1976; see Sec. IV.C.4). A similar formula was devised by Müller (1975) and Fritsch and Wille (1979).

Macek and Briggs separated the radiation amplitude into a part due to MO x rays and a Lorentzian amplitude,

$$D(E_x)\sim\Gamma\left[E_x-E_{\mathrm{SA}}+\frac{i\Gamma}{2}\right]^{-1}, \tag{2.1}$$

centered on the separated-atom (SA) $K\alpha$ or $K\beta$ x-ray energy at E_{SA}. In heavy-ion—atom collisions, continua seen at x-ray energies E_x-E_{SA} much in excess of the linewidth Γ are less intense than the SA Lorentzian intensity. Anholt (1976; Sec. III.B) rederived the Macek-Briggs formulas, obtaining, instead of a Lorentzian amplitude, an amplitude for one-collision MO x-ray production, in which the $1s\sigma$ vacancy is made in the same collision where it radiates. Such "one-collision" MO x-ray production had been proposed earlier. Meyerhof *et al.* (1974) derived a simple formula relating the one-collision MO x-ray cross section to the product of the probability of producing a $1s\sigma$ vacancy in a collision with impact parameter b, $P_{1s\sigma}(b)$ and the probability of radiative decay in the internuclear distance interval ΔR, which is approximately $\lambda(R)\Delta R/v$, $\lambda(R)$ being the radiative decay rate, and v the ion velocity. The calculations of Meyerhof *et al.* were incorrect on three counts: First, Anholt's work demonstrated that one must multiply amplitudes for $1s\sigma$-vacancy production and radiative decay, and not probabilities. Second, because virtually nothing was then known about $1s\sigma$-vacancy production, Meyerhof *et al.* chose an impact-parameter dependence for $P_{1s\sigma}$, which although fitting the MO x-ray spectra, is now known to be incorrect (Bang and Hansteen, 1959; Müller *et al.*, 1978). Finally, the $1s\sigma$ cross sections used to normalize the magnitude of $P_{1s\sigma}(b)$ were later found to be incorrect, due to contributions from the internal conversion of nuclear Coulomb-excited γ rays (Meyerhof *et al.*, 1976).

The calculation of one-collision $1s\sigma$ MO x-ray production has continued to elude theorists, although firm evidence of its presence has been found in gas-target experiments where two-collision MO x rays are not present (Bell *et al.*, 1975; Laubert *et al.*, 1976; Schmidt-Böcking *et al.*, 1978b; Sec. IV.C.3). The shapes of one- and two-collision MO x-ray spectra are very similar, although the anisotropy spectra are quite different (Stoller *et al.*, 1981; Sec. V.D). Because fundamental theories of the ionization of $1s\sigma$ electrons are lacking, few attempts to calculate one-collision MO x rays have been made [with the exception of one model calculation for $H^+ + H$ collisions by Thorson and Choi (1977) and one calculation for Pb + Pb collisions by Kirsch *et al.* (1978)].

The theory of the angular distribution of two-collision MO x rays continued to be developed. Müller and coworkers (Müller and Greiner, 1974; Müller, Smith, and Greiner, 1974,1975) and Smith *et al.* (Smith, Müller, and Greiner, 1975) made a number of increasingly refined calculations with their induced and spontaneous radiative-interaction Hamiltonians, but the existence of induced transitions was finally disproven by Gros *et al.* (1977), who showed that one must account for Coriolis forces in the rotating molecule by considering the effect on the initial and final electronic wave functions instead of on the radiative-interaction Hamiltonian. Gros *et al.* (1977) used perturbation theory to couple the $2p\sigma$ and $2p\pi$ wave functions, but this coupling is so strong that perturbation theory is only applicable at extremely low projectile energies, of little practical interest.

A more fundamental problem with the MO x-ray calculations made prior to the publication of the papers by Gros *et al.* and Briggs and Dettmann (1977) is that the calculations were made in a noninertial frame. Macek and Brigg's (1974) dynamic theory assumes that the transition dipole lies parallel or antiparallel to the rotating internuclear axis. (They Fourier-transformed the magnitude of the dipole transition vector, neglecting its direction.) Such calculations are appropriate for stable diatomic molecules rotating at a constant velocity, but not in a collision where the rotation is accelerated. The rotational velocity is small at large internuclear distances, and reaches a maximum at the distance of closest approach of the projectile and target nuclei. The induced transition term, proportional to the rotational velocity, is a spurious contribution due to the use of a noninertial frame. The main contribution of Gros *et al.* and Briggs and Dettmann, therefore, was the realization that for quasimolecular x-ray emission, calculations must be made in an inertial frame. The theory of Macek and Briggs (1974) is sometimes valid, however, and is useful in many approximate calculations, as long as the detailed angular distribution of MO x rays is not of primary concern. Its validity can be understood using the perfect electron-slip model (Sec. V.B.2).

Due to numerical miscalculations, Briggs and Dettmann (1977) failed to discover an important effect on MO x-ray emission: Coriolis coupling prevents the MO's from rotating with the internuclear axis, keeping them aligned with respect to the beam axis during the collision (Anholt, 1978a). Because the wave function for an electron initially in the $2p\sigma$ MO remains oriented along the beam axis, its transition dipole is oriented along the beam axis, and radiation is emitted predominantly perpendicular to the beam axis. If there are an equal number of σ and π electrons, no MO x-ray anisotropy is seen, because radiation from the electron initially occupying the $2p\pi$ MO is emitted parallel to the beam axis. An unequal number of σ and π electrons cause the observed positive $1s\sigma$ MO x-ray anisotropy (Anholt, 1978a; Briggs *et al.*, 1979; see Sec. V.B).

The *ab initio* calculation of the MO x-ray anisotropy marked the point where theory caught up with experiments. Subsequently, theory could explain and even predict experimental results. It was suggested in 1977 that the anisotropy peak position could be used to predict UA K binding energies in superheavy collisions (Stoller *et al.*, 1977). However, Anholt (1978a) predicted near-zero MO x-ray anisotropies in superheavy quasimolecules Pb + Pb and U + U, a result subsequently found experimentally by Stoller *et al.* (1980; see Sec. V.C). Also, while scaling laws certainly agreed that the anisotropy peak position should scale with UA transition energies, it is clear that the nonrelativistic one-electron scaling laws break down for collisions with superheavy UA's, precisely because of the relativistic and quantum-electrodynamical effects which make the measurement of those transition energies interesting (Anholt, 1979a).

Several other results corroborating theoretical expectations have been obtained. X rays due to the filling of $2p\sigma$ vacancies were identified by Heinig *et al.* (1976), and their intensity and anisotropy have been quantitatively calculated by Anholt (1979a) and Jäger *et al.* (1981) (see Secs. IV.D and V.F). A few simple calculations for L and M MO x-ray emission have been made (Morovic *et al.*, 1977), but full dynamic calculations have proved too difficult. The impact-parameter dependence of $1s\sigma$ MO x rays was measured by Tserruya *et al.* (1976) for Cl + Cl collisions and subsequently for 90-MeV Ni + Ni collisions by Schmidt-Böcking *et al.* (1982) and for low-velocity Cl + Ar collisions by Tserruya *et al.* (1983) (see Sec. VI.A). The low-velocity Cl + Ar measurements are of special interest because interference between MO x-ray emission on the incoming and outgoing parts of the collision at a given impact parameter produces an oscillatory MO x-ray spectrum, predicted by Lichten (1974) and Macek and Briggs (1974). Also, as a test of the dynamic MO x-ray calculations, measurements of the azimuthal MO x-ray anisotropy (Schuch *et al.*, 1981; Bürgy *et al.*, 1981; Sec. VI.B) and MO x-ray—SA K x-ray coincidences (O'Brien *et al.*, 1980; Zouros *et al.*, 1984; Sec. VI.D) were found to be in reasonable agreement with theory. Calculations of MO x-ray—compound-nucleus (CN) K x-ray interferences in collisions where long-lived UA's are formed have been made (Anholt, 1979b). Although CN x rays have been seen only in H^+ + In and H^+ + Sn collisions (Chemin *et al.*, 1979; Röhl *et al.*, 1981) where MO x rays are unimportant, this work has a bearing on time-delay experiments in heavy-ion—atom collisions where long-lived nuclear complexes are made (Anholt, 1985).

III. THEORIES OF MOLECULAR-ORBITAL X-RAY EMISSION

A. The quasistatic approximation

The quasistatic model of MO x-ray emission was first proposed by Briggs (1974) and Meyerhof *et al.* (1974), although its use was originally applied to spectral line broadening in plasmas by Kuhn (1934). Correlation diagrams (Fig. 1; Fano and Lichten, 1965; Lichten, 1967; Barat and Lichten, 1972) give a one-to-one relation between the internuclear distance R and the transition energy $\Delta E_{if}(R)$. A number of possible transitions $i \rightarrow f$ can occur at any internuclear distance. For K or $1s\sigma$ MO x rays, the most intense transition is the $2p\pi \rightarrow 1s\sigma$ one. The quasistatic theory assumes that x rays of energy E_x are emitted only at the internuclear distance R_g where $E_x = \Delta E_{if}(R_g)$. The emission probability $\Delta P_{if}(E_x)$ is then given by

$$\Delta P_{if} = \frac{2\lambda_{if}(R_g)\Delta R}{v_R} , \tag{3.1}$$

where $\lambda_{if}(R_g)$ is the radiative transition rate assuming a single vacancy in the initial state, v_R is the radial component of the ion velocity v given by

$$v_R = v\left[1 - \frac{U(R)}{E_c} - \frac{b^2}{R^2}\right]^{1/2} , \tag{3.2}$$

b is the impact parameter, $U(R_g)$ is the internuclear potential, and E_c is the c.m. kinetic energy. The factor of 2 in Eq. (3.1) is present because there are two places along the trajectory where the ion passes the point where the internuclear distance is equal to R_g. The x-ray emission cross section is obtained by integrating Eq. (3.1) over the impact parameters

$$\Delta\sigma_{if}(E_x) = \int_0^{R_g} 2\pi b\, db\, \Delta P_{if}(E_x) , \tag{3.3}$$

giving

$$\frac{d\sigma_{if}}{dE_x} = 4\pi R_g^2 \frac{dR_g}{d\Delta E_{if}}\left[1 - \frac{U(R_g)}{E_c}\right]^{1/2} \frac{\lambda_{if}(R_g)}{v} , \tag{3.4}$$

where we have divided both sides by $dE_x = d\Delta E_{if}$.

Equations (3.1)—(3.4) assume the presence of a vacancy in the initial MO. As fully stripped projectiles usually cannot be used,[1] the vacancy must either be made in the same collision where it radiates (one-collision MO x rays) or have been made in a prior collision (two-collision MO x rays). In a solid target, inner-shell vacancies are constantly being made, which normally decay by the emission of SA x rays or Auger electrons, or by collision quenching (Gray *et al.*, 1976; Meyerhof *et al.*, 1977). For a projectile vacancy formation cross section σ_v and a total decay rate λ_v, the equilibrium number of projectile vacancies is given by the ratio of the formation rate to the total rate:

$$N_v = \frac{n_2\sigma_v v}{\lambda_v + n_2\sigma_v v} \approx \frac{n_2\sigma_v v}{\lambda_v} , \tag{3.5}$$

since the vacancy decay rate is normally much smaller

[1]To strip an ion fully requires that the ion velocity be larger than all electron velocities (Bohr, 1948), which violates the condition for the formation of MO's. However, it is possible to strip a projectile fully then slow it down sufficiently to allow the inner shells to form MO's. These experiments are discussed in Sec. VI.A.

than the rate of formation ($N_v \ll 1$). Inserting N_v into Eq. (3.4) we obtain the MO x-ray cross section

$$\frac{d\sigma_{if}}{dE_x}=4\pi n_2 R_g^2 \frac{dR_g}{dE_{if}}\frac{\lambda_{if}}{\lambda_x}\left[1-\frac{U(R_g)}{E_c}\right]^{1/2}\sigma_{px}W\ , \quad (3.6)$$

where we have substituted the projectile K x-ray cross section σ_{px} divided by the radiative decay rate λ_x in place of the vacancy formation cross section divided by the sum of the radiative, Auger, and collision quenching rates. Two-collision MO x-ray production can thus be calculated from the measured projectile K x-ray cross section without regard to uncertainties in projectile K-shell fluorescence yields in solid targets. The total MO x-ray cross section is given by summing Eq. (3.6) over all significant transitions $i \rightarrow f$.

One additional factor has been included in Eq. (3.6): W is the probability that the projectile inner-shell vacancy goes into the MO of interest. To make $1s\sigma$ MO x rays, a projectile K vacancy must be made which goes into the $1s\sigma$ MO with a probability $W=1-w$ if the projectile is the heavier collision partner of w if it is the lighter. Here w is the K-vacancy sharing probability given by (Meyerhof, 1973)

$$w=[1+\exp(2x)]^{-1}\ , \quad (3.7)$$

where

$$2x=\pi\frac{[(U_{KH})^{1/2}-(U_{KL})^{1/2}]}{(\frac{1}{2}mv^2)^{1/2}}\ , \quad (3.8)$$

U_{KH} and U_{KL} are the K-shell binding energies of the heavier and lighter collision partners and m is the electron mass.

Equation (3.6) has another interpretation. The ratio of MO x rays emitted with energy E_x to the total number of projectile K x rays is given by

$$\frac{1}{\sigma_{px}}\frac{d\sigma_{if}}{dE_x}=\left[4\pi n_2 R_g^2\frac{dR_g}{dE_x}\right]\left[\frac{\lambda_{if}}{\lambda_x}\right]\left[1-\frac{U(R_g)}{E_c}\right]^{1/2}W\ , \quad (3.9)$$

where the first factor on the right-hand side is the probability that the projectile can be found at an internuclear distance R_g to $R_g+\Delta R_g$ from another target atom. This is the volume element for that distance $4\pi R_g^2\Delta R_g$ divided by the total volume each target atom occupies n_2^{-1}. The second factor weights this probability by the ratio of the radiative transition rates at that distance compared to projectile rate. The third factor accounts for the possibility that internuclear repulsion due to the potential $U(R_g)$ may prevent the projectile with energy E_c from penetrating to the distance R_g. The final factor assures that the vacancy is in the $1s\sigma$ and not in the $2p\sigma$ MO (for $1s\sigma$ MO x rays).

Equation (3.6) assumes that the target atoms remain stationary and that only the projectile is able to carry vacancies from one collision to the next in solid targets. In fact, target atoms can recoil in the initial collision, and make MO x rays in subsequent target-target collisions. This can be important in some exceptional cases, as discussed by Meyerhof and Anholt (1979).

The quasistatic model gives a sharp cutoff of the MO x-ray emission cross section at or below the transition energy where $U[R_g(E_x)]/E_c=1$. The exception to this is for MO x rays where the transition energy is larger at intermediate internuclear distances than at small internuclear distances, e.g., for $2p\sigma$ MO x rays, as discussed in Sec. IV.D. That such end points in the MO x-ray spectra were not observed experimentally (Greenberg *et al.*, 1974) stimulated the formulation of dynamic theories of MO x-ray emission.

B. Dynamic theories

1. Separation of one- and two-collision MO x-ray emission

Experimental MO x-ray spectra extend beyond their UA end points because of collision broadening. The x-ray energy E_x need not be exactly the MO transition energy: any energy excess or deficit can be obtained by converting translational kinetic energy into electromagnetic energy. Weisskopf (1933) showed that the line shape for the transition $i \rightarrow f$ can be calculated from the Fourier transform of the dipole velocity matrix element $D_{if}[R(t)]=\langle\chi_i(\mathbf{r},\mathbf{R})\,|\,p\,|\,\chi_f(\mathbf{r},\mathbf{R})\rangle$:

$$D_{if}(\omega)=\frac{1}{\sqrt{2\pi}}\int_{-\infty}^{+\infty}dt\,a_i(t)D_{if}[R(t)] \times\exp\left[i\int_0^t[\omega-\omega_{if}(t')]dt'\right]\ , \quad (3.10)$$

where $\hbar\omega_{if}[R(t)]=\Delta E_{if}(R)$ is the transition energy and $\hbar\omega=E_x$ is the x-ray energy. Unlike Weisskopf (1933) or Macek and Briggs (1974), we introduce a factor $a_i(t)$, which is the amplitude for the presence of the inner-shell vacancy (Anholt, 1976). In practical calculations, $a_i(t)$ depends on quantum numbers which must be summed over incoherently. For example, if K MO's are considered, $a_i(t)$ is the amplitude for the formation of a $1s\sigma$ vacancy, which is the amplitude for the excitation of $1s\sigma$ electrons into a continuum state of energy ε and angular quantum numbers L and M (Thorson and Choi, 1977). $D_{if}(\omega)$ then becomes a function of ε, L, and M, and the total MO emission rate probability is given by

$$\frac{dP_{if}}{d\omega}=\tfrac{4}{3}\alpha^3\omega\int_0^\infty d\varepsilon\sum_{LM}|D_{if}(\omega,\varepsilon LM)|^2\ . \quad (3.11)$$

If the Fourier transforms are carried out along a Coulomb trajectory with impact parameter b, the total MO x-ray emission cross section is obtained by integrating P_{if} over impact parameters as in Eq. (3.3).

As in the quasistatic approximation, MO x rays with energies significantly different from SA transition energies are made in the vicinity of small internuclear distances R_g, where ω is approximately equal to $\omega_{if}(R_g)$.

To obtain both one- and two-collision MO x-ray production, let us choose a value of T defining the collision time such that $R(T) \gg R_g$. Then the time integral in Eq. (3.10) can be written as

$$\int_{-\infty}^{+\infty} dt \cdots = \int_{-\infty}^{-T} + \int_{-T}^{T} + \int_{T}^{t_c - T} + \int_{t_c - T}^{t_c + T} + \int_{t_c + T}^{\infty} , \tag{3.12}$$

where t_c is the time between collisions. The first integral gives zero because the vacancy amplitude a_i is zero before the first collision has occurred. The third integral gives the contribution between collisions, where $\omega_{if}(t)$ is the SA transition energy $\omega_{if}(\infty)$. During this time the vacancy amplitude decays exponentially, with a decay rate Γ given by the sum of the x-ray and Auger decay rates. This part gives only SA K x rays, hence we neglect it in calculating MO x rays with $\omega \gg \omega_{if}(\infty)$. The fourth contribution gives two-collision MO x rays. Since MO x-ray production in third and further collisions becomes increasingly unlikely, we drop the fifth integral. The MO x-ray amplitude is therefore given by

$$D_{if}(\omega,b) = D_{if}^{(1)}(\omega,b) + a_i(\infty)\exp\{i[\omega - \omega_{if}(\infty)]t_c - \Gamma t_c/2\} \times D_{if}^{(2)}(\omega,b) , \tag{3.13}$$

where the one-collision amplitude is given by

$$D_{if}^{(1)}(\omega,b) = \frac{1}{\sqrt{2\pi}} \int_{-T}^{T} dt\, a_i(t) D_{if}[R(t)] \times \exp\left[i \int_0^t [\omega - \omega_{if}(t')] dt' \right] . \tag{3.14}$$

The two-collision amplitude is given by

$$D_{if}^{(2)}(\omega,b) = \frac{1}{\sqrt{2\pi}} \int_{-T}^{T} dt\, D_{if}[R(t)] \times \exp\left[i \int_0^t [\omega - \omega_{if}(t')] dt' \right] , \tag{3.15}$$

where we have neglected the exponential decay factor during the collision, since $\Gamma T \ll 1$. The value of T is immaterial as long as $\omega_{if}(T) \sim \omega_{if}(\infty)$. The impact parameter b_2 in the second collision will surely be different from that in the first, so to obtain the MO x-ray emission cross section, we average $|D_{if}(\omega)|^2$ over the time between collisions t_c and over b_2. In averaging over t_c, we use a perfect gas model, which assumes that the distances between collisions are randomly distributed, with an average value l^* given by

$$l^* = \frac{1}{n_2 \sigma_c} , \tag{3.16}$$

where σ_c is the collision cross section defined below. The average over collision time t_c is given by

$$\frac{dP_{if}}{dE_x} = \tfrac{4}{3}\alpha^3 \omega \int_0^{\infty} \frac{dl}{l^*} \exp(-l/l^*) \left| D_{if}^{(1)} + a_i(\infty)\exp[i\Delta l/v - \Gamma l/(2v)] D_{if}^{(2)} \right|^2 , \tag{3.17}$$

where $\Delta = \omega - \omega_{if}(\infty)$. Cross terms in this average, proportional to

$$\frac{D_{if}^{*(1)} D_{if}^{(2)}}{1 + \frac{\Gamma l^*}{2v} - \frac{i\Delta l^*}{v}} ,$$

tend to be much smaller than the term in $|D_{if}^{(1)}|^2$ or

$$\frac{|D_{if}^{(2)}|^2}{1 + \frac{\Gamma l^*}{v}} ,$$

because $\Delta = \omega - \omega_{if}(\infty)$ is always much greater than $\Gamma/2$. Dropping the cross terms we obtain

$$\frac{dP_{if}(b)}{d\omega} = \tfrac{4}{3}\alpha^3 \omega \left[|D_{if}^{(1)}(\omega,b)|^2 + \frac{n_2 \sigma_c v}{\Gamma} |a_i(\infty,b)|^2 |D_{if}^{(2)}(\omega,b_2)|^2 \right] . \tag{3.18}$$

We average over the impact parameter in the second collision, introducing the probability of having an impact parameter b_2 as

$$P(b_2) = \begin{cases} 2\pi b_2 db_2/\sigma_c & \text{for } \pi b_2^2 < \sigma_c \\ 0 & \text{for } \pi b_2^2 > \sigma_c . \end{cases} \tag{3.18a}$$

The total MO x-ray production cross section is then given by integrating over the initial and second impact parameters,

$$\frac{d\sigma_{if}}{d\omega} = \tfrac{4}{3}\alpha^3 \omega \sum_{LM} \int_0^{\infty} d\varepsilon \int_0^{\infty} 2\pi b\, db\, |D_{if}^{(1)}(\omega,b,\varepsilon LM)|^2 + \frac{\sigma_K n_2 v}{\Gamma} \tfrac{4}{3}\alpha^3 \omega \int_0^{\infty} 2\pi b\, db\, |D_{if}^{(2)}(\omega,b)|^2 , \tag{3.19}$$

where σ_K is given by

$$\sigma_K = \int_0^\infty 2\pi b\, db \sum_{LM} \int_0^\infty d\varepsilon \,|\, a_i(\infty, \varepsilon LM) \,|^2 . \quad (3.20)$$

The numerical value chosen for the collisional cross section σ_c is inconsequential as long as the maximum impact parameter in Eq. (3.18a) is such that $|\, D_{if}^{(2)}(\omega, b_{2\max}) \,|^2$ is negligibly small, hence we can put $b_{2\max} = \infty$.

The cross section σ_K appearing in the two-collision MO x-ray term in Eq. (3.19) is the $1s\sigma$-vacancy production cross section, because we required that a vacancy be made in the $1s\sigma$ MO. Equation (3.19) neglects the electronic excitation from the $2p\sigma$ MO in the first encounter. In general σ_K should be replaced by

$$\sigma_K = w(1-w)\sigma_{2p\sigma} + W'^2 \sigma_{1s\sigma} , \quad (3.21)$$

where W' is w^2 if the projectile is the lighter collision partner or $(1-w)^2$ if it is the heavier one, and w is given by Eq. (3.7). One can generally neglect the $1s\sigma$ contribution. Then if normalization to the projectile K-vacancy production cross section is desired, σ_K can be replaced by

$$\sigma_K = W\sigma_v , \quad (3.22)$$

where W was defined after Eq. (3.6). In fact, it is the $2p\sigma$-vacancy production contribution that makes the two-collision process dominant over the one-collision process in some cases. The one-collision term is very roughly proportional to the $1s\sigma$ ionization probability

$$P_{1s\sigma}(b=0) = \int_0^\infty d\varepsilon \sum_{LM} |\, a_i(b=0, \infty, \varepsilon LM) \,|^2 , \quad (3.23)$$

while the comparable proportional term for two-collision MO x-ray production is given by $\sigma_K n_2 v/\Gamma$. Both of these factors are small, the second being much smaller if the $1s\sigma$ cross section is used for σ_K. However, because $2p\sigma$-vacancy production is so much more likely than $1s\sigma$-vacancy production (see Fig. 3), the two-collision contribution may be as large as or larger than the one-collision contribution. As in the quasistatic theory, we can write σ_v/Γ as σ_{px}/λ_x.

The exception to the use of the perfect gas model or the random-phase approximation to separate the one- and two-collision MO x-ray contributions occurs in collisions in oriented single crystals, where the time between collisions can be nearly fixed. Coherence between one- and two-collision MO x-ray production, or two- and more-collision MO x-ray production is difficult to observe, however (Gros and Greiner, 1975).

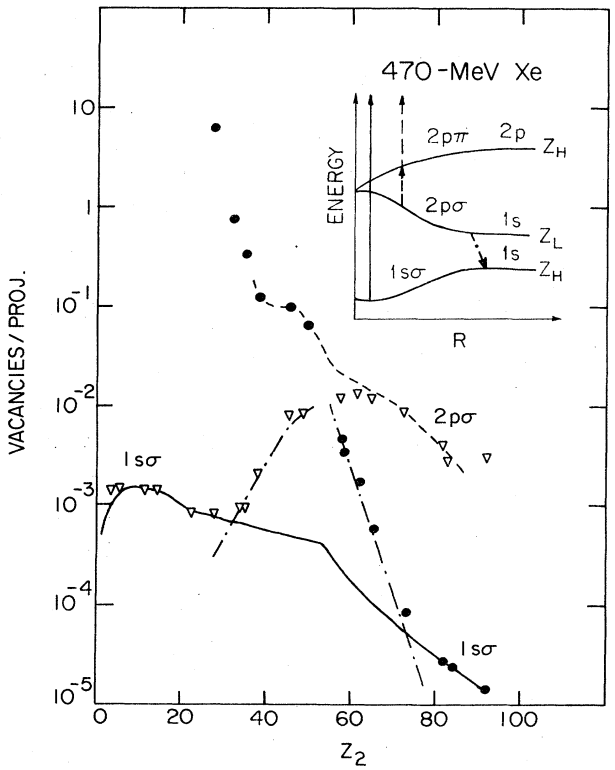

FIG. 3. Projectile (▽) and target (●) thick-target K-vacancy production yields in 470-MeV/amu Xe collisions. The dashed curve shows schematically the yield of vacancies created in the $2p\sigma$ MO, and the solid curve shows the yield of vacancies created in the $1s\sigma$ MO. The dot-dashed curve shows the yield of $2p\sigma$ vacancies shared with the higher-Z collision partner on the outgoing part of the collision (Meyerhof *et al.*, 1976).

2. The stationary-phase approximation

The quasistatic approximation results of Sec. III.A can be recovered from the dynamic theory using the stationary-phase approximation (Macek and Briggs, 1974). The phase factor

$$\varphi(t) = \int_0^t [\omega - \omega_{if}(t')]dt' , \quad (3.24)$$

varies rapidly with time except near $t = t_g$, where $\omega = \omega_{if}$. Since the integrand is proportional to the oscillatory factor $\exp[i\varphi(t)]$, positive and negative contributions to the integral tend to cancel out except in the region where the phase becomes stationary. Expanding $\varphi(t)$ around t_g

$$\varphi(t) = \varphi(t_g) - \frac{1}{2}\frac{d\omega_{if}}{dt}(t-t_g)^2 , \quad (3.25)$$

we obtain

$$D_{if}^{(2)}(\omega) = \frac{D_{if}[R(t_g)]}{(\dot{\omega}_{if})^{1/2}} 2\cos\left[\varphi(t_g) + \frac{\pi}{4}\right] . \quad (3.26)$$

The cosine term comes from the interference between the two points along the trajectory where the projectile intersects the distance $R(t_g)$. The MO x-ray emission probability is then given by

$$\frac{dP_{if}}{dE_x} = \tfrac{4}{3}\alpha^3\omega \frac{|\, D_{if}(t_g) \,|^2}{\dot{\omega}_{if}} [2 + 2\sin 2\varphi(t_g)]$$

$$= \frac{2\lambda_{if}(R_g)}{v}\frac{\Delta R}{\Delta E_x}[1 + \sin 2\varphi(t_g)] . \quad (3.27)$$

The quasistatic result, Eq. (3.1), is obtained except for the oscillatory factor $\sin 2\varphi(t_g)$ due to the interference be-

tween x-ray emission on the incoming and outgoing paths. This has little effect on the total MO x-ray emission cross section, since the sine term nearly averages to zero when one integrates over the impact parameter. However, the MO x-ray emission probability oscillates with x-ray energy for fixed b (Lichten, 1974; Macek and Briggs, 1974) or with impact parameter for fixed x-ray energy (Anholt, 1982a). The frequency of oscillation in x-ray energy $\Delta\omega$ is calculated from

$$2\varphi(t_g)=2\int_0^{t_g}[\Delta\omega-\omega_{if}(t')]dt'=2\pi\ , \tag{3.28}$$

giving approximately

$$\Delta\omega\approx\frac{\pi v}{R_g}\ . \tag{3.29}$$

To obtain many oscillations (small $\Delta\omega$), a very small ion velocity or a large value of R_g is required. One calculates that one full oscillation over the $1s\sigma$ MO x-ray energy spectrum should be seen in 20-MeV Ni + Ni collisions (Anholt, 1982a). According to the scaling laws discussed in Sec. IV.C.2, such oscillations should also be present in 4-MeV Cl + Cl collisions or 219-keV N + N collisions. Oscillations have recently been observed for $1s\sigma$ MO x-ray production in low-velocity collisions with fully stripped projectiles (Sec. VI.A), and for analogous Auger electron emission in Kr + Kr collisions (Sec. VI.F).

C. The angular distribution of molecular-orbital x rays

1. General theory

The angular anisotropy spectrum is one of the most interesting features of MO x-ray emission, and has strongly supported the quasimolecular identity of the continuum x rays. Its calculation requires considerably more detail than that given in the preceding section. One must take into account not only the direction of the transition dipole in the Fourier transform, but also the strong Coriolis coupling between the Born-Oppenheimer basis functions describing the initial and final molecular states. As with any semiclassical theory of photon emission (Sakurai, 1967; Schiff, 1968), first-order perturbation theory is used to obtain the rate of change of the amplitude for the transition of an electron from state i to state f with the emission of a photon with polarization $\hat{\varepsilon}_\lambda$ (Briggs and Dettmann, 1977; Anholt, 1978a):

$$\dot{f}_{\lambda ij}=\frac{i}{2\pi\sqrt{\omega}}\langle\Psi_f^-(t)\,|\,\mathbf{p}\cdot\hat{\varepsilon}_\lambda e^{i\omega t}\,|\,\Psi_i^+(t)\rangle\ , \tag{3.30}$$

where $\mathbf{p}$ is the electron momentum operator. The wave functions $\Psi^\pm(t)$ are solutions to the full time-dependent Schrödinger equation

$$H_s\Psi^\pm(t)=i\frac{\partial\Psi^\pm}{\partial t}\ , \tag{3.31}$$

where H_s is the scattering Hamiltonian. Generally, $\Psi^\pm(t)$ are expanded in a set of adiabatic MO wave functions χ_n:

$$\Psi_i^\pm(t)=\sum_n a_{ni}^\pm(t)\chi_n(\mathbf{r},\mathbf{R},t)\exp\left[i\int^t\varepsilon_n(t')dt'\right]\ , \tag{3.32}$$

satisfying

$$H_{\rm MO}\chi_n(\mathbf{r},\mathbf{R})=\left[-\frac{\nabla^2}{2}-\frac{Z_1}{\left|\mathbf{r}-\frac{\mathbf{R}}{2}\right|}-\frac{Z_2}{\left|\mathbf{r}+\frac{\mathbf{R}}{2}\right|}\right]\chi_n$$

$$=\varepsilon_n\chi_n\ , \tag{3.33}$$

where ∇^2 is the electron kinetic energy operator, ε_n is the electronic energy eigenvalue, and $\mathbf{r}$ is the electron coordinate. Inserting Eq. (3.32) into Eq. (3.30) we have

$$f_{\lambda if}=\frac{i}{2\pi\sqrt{\omega}}\hat{\varepsilon}_\lambda\cdot\mathbf{D}_{if}(b,\omega)\ , \tag{3.34}$$

where

$$D_{if}(b,\omega)=\int_{-\infty}^{\infty}dt\,e^{i\omega t}\sum_{nm}a_{nf}^-(t)a_{mi}^+(t)\langle\chi_n(\mathbf{r},\mathbf{R})\,|\,\mathbf{p}\,|\,\chi_m(\mathbf{r},\mathbf{R})\rangle\exp\left[i\int^t[\varepsilon_n(t')-\varepsilon_m(t')]dt'\right]\ . \tag{3.35}$$

Since the angular distribution is measured relative to the beam velocity direction $\mathbf{v}$, it is natural to decompose $\mathbf{D}_{if}$ into a component D_{zif} parallel to $\mathbf{v}$, a component D_{xif} parallel to $\mathbf{b}$, and a component D_{yif} parallel to the direction $\mathbf{y}=\mathbf{b}\times\mathbf{v}$, perpendicular to the collision plane:

$$\mathbf{D}_{if}=D_{xif}\hat{\mathbf{b}}+D_{zif}\hat{\mathbf{v}}+D_{yif}\hat{\mathbf{y}}\ . \tag{3.36}$$

The probability for a transition between states i and f with the emission of an x ray into the solid angle $d\Omega$ is given by

$$\frac{dP_{if}}{d\omega\,d\Omega}=\frac{\omega^2}{c^3}\sum_\lambda|f_{\lambda if}|^2$$

$$=\frac{\omega}{4\pi^2c^3}(|\mathbf{D}_{if}|^2-|\mathbf{D}_{if}\cdot\hat{\mathbf{k}}|^2)\ . \tag{3.37}$$

In most measurements where the emission probability or cross section is determined, the azimuthal angle between the photon direction $\hat{\mathbf{k}}$ and the collision plane is not determined (for an exception, see Sec. VI.B). Averaging over the azimuthal angle, we obtain

$$\frac{d^2P_{if}(\omega)}{d\omega\, d\Omega}=\frac{\omega}{6\pi^2c^3}[\,|\,\mathbf{D}_{if}\,|^2-(3\,|\,D_{zif}\,|^2-|\,\mathbf{D}_{if}\,|^2)\times\tfrac{1}{2}P_2(\cos\theta)]\,, \quad (3.38)$$

where $P_2=\frac{1}{2}\,(3\cos^2\theta-1)$. Integrating this probability over impact parameters and summing over possible transitions $i\to f$, we obtain

$$\frac{d^2\sigma(\omega,\theta)}{d\omega\, d\Omega}=\frac{\omega}{3\pi c^3}I_0[1-A_0P_2(\cos\theta)]\,, \quad (3.39)$$

where

$$I_0=\sum_{if}\int_0^\infty b\,db\,|\,\mathbf{D}_{if}\,|^2\,,$$
$$I_z=\sum_{if}\int_0^\infty b\,db\,|\,D_{zif}\,|^2\,, \quad (3.40)$$

and

$$A_0=\frac{3I_z-I_0}{2I_0}\,. \quad (3.41)$$

A_0 is a parameter that varies from $-\frac{1}{2}$ to 1. Normally, one measures the MO x-ray anisotropy defined by

$$\eta(E_x)=\frac{d^2\sigma(90°)}{d^2\sigma(0°)}-1=\frac{1.5A_0}{1-A_0}\,. \quad (3.42)$$

This parameter varies from $-\frac{1}{2}$ to infinity.

2. Two-collision $1s\sigma$ MO x-ray production

Equations (3.30)—(3.42) constitute the general theory of x-ray emission during a collision. For the emission of MO x rays in a transition between a given initial state i and a final state f, one must specify the electron and hole amplitudes a_{mi}^{+} and a_{nf}^{-} in Eq. (3.35). For the specific case of two-collision $1s\sigma$ MO x rays, the amplitude a_{nf}^{-} is identical to the amplitude a_i in Eq. (3.10). The separation of the emission amplitude $\mathbf{D}_{if}(\omega,b)$ into one- and two-collision MO x-ray contributions proceeds in the same way as Eqs. (3.12)—(3.20). For two-collision MO x-ray production, we can take a_{nf}^{-} to be constant; $|\,a_{nf}^{-}\,|^2$ is just the number of $1s\sigma$ vacancies in Eq. (3.5) or the factor $\sigma_K n_2 v/\Gamma$ in Eq. (3.19).

For the electron amplitudes a_{mi}^{+}, we have to account for the strong Coriolis coupling between the $p\sigma$ and $p\pi$ MO's (Bates and Williams, 1964; Thorson and Levy, 1969; Briggs and Macek, 1972). The total wave function $\Psi_i(t)$ is given by

$$\Psi_i(t)=a_{\sigma i}\chi_\sigma\exp\left[i\int_0^t\varepsilon_\sigma(t')dt'\right]+(a_{\pi xi}+a_{\pi yi})\chi_\pi\exp\left[i\int_0^t\varepsilon_\pi(t')dt'\right]\,, \quad (3.43)$$

where $a_{\sigma i}=a_{2p\sigma i}$ or $a_{3p\sigma i}$, depending on the radiative transition being considered. Coriolis coupling is very strong; the weak coupling between the $2p$ and $3p$ MO's and between the $2p$ or $3p$ MO's and the continuum or loosely bound states can be neglected. The amplitudes are obtained by simultaneously solving the differential equations (Briggs and Macek, 1972)

$$\frac{da_{\sigma i}}{dt}=a_{\pi xi}\dot{\Theta}\left\langle\chi_\sigma\left|\frac{\partial}{\partial\Theta}\right|\chi_\pi\right\rangle\times\exp\left[-i\int_0^t[\varepsilon_\pi(t')-\varepsilon_\sigma(t')]dt'\right]\,,$$
$$\frac{da_{\pi xi}}{dt}=-a_{\sigma i}\dot{\Theta}\left\langle\chi_\sigma\left|\frac{\partial}{\partial\Theta}\right|\chi_\pi\right\rangle\times\exp\left[i\int_0^t[\varepsilon_\pi(t')-\varepsilon_\sigma(t')]dt'\right]\,,$$

and

$$\frac{da_{\pi yi}}{dt}=0\,, \quad (3.44)$$

with the initial conditions

$$a_{mi}^{+}(-\infty)=\delta_{mi}\,. \quad (3.45)$$

Here $\Theta(t)$ is the angle between the internuclear axis and the beam axis, and $\langle\chi_\sigma\,|\,\partial/\partial\Theta\,|\,\chi_\pi\rangle$ is the rotational coupling matrix element which approaches unity at $R=0$ and can generally be taken to be equal to unity at all relevant internuclear distances (Taulbjerg *et al.*, 1976). Because the molecule rotates about the y axis, the $2p\pi_y$ MO cannot couple to either the σ or the π_x MO, hence $a_{\pi yi}$ remains constant.

Substituting these amplitudes into Eq. (3.35), we can write the components of $\mathbf{D}_{if}$ as

$$D_{zi}=\int_{-\infty}^{+\infty}dt[a_{\sigma i}\cos\Theta(t)D_\sigma e^{i\Delta\sigma}+a_{\pi xi}\sin\Theta(t)D_\pi e^{i\Delta\pi}]\,,$$
$$D_{xi}=\int_{-\infty}^{+\infty}dt[-a_{\sigma i}\sin\Theta(t)D_\sigma e^{i\Delta\sigma}+a_{\pi xi}\cos\Theta(t)D_\pi e^{i\Delta\pi}]\,, \quad (3.46)$$
$$D_{yi}=\int_{-\infty}^{+\infty}dt\,a_{\pi y}D_\pi e^{i\Delta\pi}\,,$$

where we have abbreviated

$$D_\sigma e^{i\Delta\sigma}=\langle\chi_{1s\sigma}\,|\,p\,|\,\chi_\sigma\rangle\times\exp\left[i\int_0^t[\omega-\varepsilon_{1s\sigma}(t')+\varepsilon_\sigma(t')]dt'\right]\,, \quad (3.47)$$

and similarly for $D_\pi e^{i\Delta\pi}$. Taking the $1s\sigma$-vacancy normalization constant from Eqs. (3.19)—(3.22), we have the cross section

$$\frac{d^2\sigma(\omega,\theta)}{d\omega\, d\Omega}=\frac{n_2vW\sigma_{px}}{\lambda_x}\frac{\omega}{3\pi c^3}I_0[1-A_0P_2(\cos\theta)]\,. \quad (3.48)$$

Once electron slip or Coriolis coupling between the $p\sigma$ and $p\pi$ MO's is included, we can no longer speak of, say, $2p\sigma\to1s\sigma$ and $2p\pi\to1s\sigma$ transitions; we can only speak of transitions from the coupled $2p\sigma$-$2p\pi$ MO. To label the coupled wave function we use greek capital letters:

2Σ, $2\Pi_x$, $2\Pi_y$, 3Σ, etc. (though this notation is usually reserved for multielectron molecular states). In this notation, for example, the 2Σ MO is the one where the electron initially was in the $2p\sigma$ MO [$a^+_{m2\Sigma}(-\infty)=\delta_{m2p\sigma}$].

This formalism has also been applied to the problem of $2p\sigma$ MO x-ray production (transitions to vacancies in the $2p\sigma$ MO during the collision; Sec. IV.D).

3. Comparison with previous theories

The main difference between the present theory and the dynamic theory of Macek and Briggs (1974) is the expression used for the radiation emission amplitude. Equation (3.46) can be compared with Eq. (3.15), which can be rewritten in the same notation as

$$D_{fi}^{(2)}(\omega,b)\sim\int_{-\infty}^{\infty}dt\,D_i\exp(i\Delta_i)\ , \tag{3.15'}$$

where $D_\sigma\exp(i\Delta_\sigma)$ is given by Eq. (3.47). The dynamic theory of Macek and Briggs does not take into account the direction of the transition dipole nor the rotational coupling between the σ and π orbitals. One way of interpreting this is that the dynamic theory assumes that electron slip is absent, so the orbitals follow the rotation of the internuclear axis. The emission amplitude is then calculated in the molecular frame; one can write $D_{1s\sigma\text{-}2p\sigma}$ in Eq. (3.15) as $D_{1s\sigma\text{-}2p\sigma}\hat{R}$, $D_{1s\sigma\text{-}2p\pi x}$ as $D_{1s\sigma\text{-}2p\pi x}\hat{R}_x$, and so on, where $\hat{R}$ is the unit vector parallel to the internuclear quantization axis, and $\hat{R}_x$ and $\hat{R}_y$ are perpendicular to this axis. Since the quantization axis rotates during the collision with a varying velocity, this corresponds to making the calculation in an accelerated frame. If one wishes to calculate the angular distribution of the radiation in the laboratory frame, additional considerations must be applied, which is what is done if one uses the kinematic dipole approximation (Hartung and Fricke, 1978; Hartung *et al.*, 1979) discussed in Sec. V.E.3.

We shall compare calculations using the dynamic and electron-slip models in a number of places in this paper. The perfect electron-slip model discussed in Sec. V.B.2 indicates that the dynamic theory is approximately valid if one interprets the direction of the Fourier-transformed transition dipole as the direction of the dipole *before* the collision in the laboratory frame. In the perfect electron-slip model, $D_\sigma\exp(i\Delta_\sigma)$ is approximately equal to $D_\pi\exp(i\Delta_\pi)$, and the remaining amplitudes, e.g., $a_{\sigma i}\cos\Theta(t)+a_{\pi xi}\sin\Theta(t)$, give approximately unity or zero, so that for a given transition, $\mathbf{D}_i$ will be aligned perfectly with $\hat{z}$, $\hat{b}$, or $\hat{y}$. In the dynamic theory, therefore, if one also neglects the difference between $D_\sigma\exp(i\Delta\sigma)$ and $D_\pi\exp(i\Delta_\pi)$, and takes $D_{1s\sigma\text{-}2p\sigma}$ to be $D_{1s\sigma\text{-}2p\sigma}\hat{z}$, $D_{1s\sigma\text{-}2p\pi x}$ to be $D_{1s\sigma\text{-}2p\pi x}\hat{b}$, and so on, one obtains identical results. The difference between the two models appears in calculations of the individual contributions to the radiation intensity (Sec. IV.C.1), the angular distribution of the MO x rays (Sec. V.B), and MO x-ray—SA K x-ray coincidences (Sec. VI.D). The perfect electron-slip model works best in collisions with small impact parameters. There it is valid to use the simpler dynamic theory for the total cross section (see Sec. IV.C.4 on MO x-ray tails from small-impact-parameter collisions and Sec. VI.E on compound nucleus x-ray emission in zero-impact-parameter collisions).

D. Wave functions and matrix elements

1. Methods of solving the molecular Schrödinger equation

Calculations of MO x-ray emission require molecular binding energies $\varepsilon_n[R(t)]$ [Eq. (3.35)] or derivatives of the binding energy differences $d\Delta E_{if}/dR$ [Eq. (3.4)], and dipole-velocity matrix elements $\mathbf{D}_{if}[R(t)]$ [Eq. (3.14)] or transitions rates $\lambda_{if}(R)\sim|\mathbf{D}_{if}|^2$ [Eq. (3.4)]. Four kinds of wave functions have been used in studies of the molecular model of inner-shell vacancy production: two-center, nonrelativistic, one-electron (hydrogenic) wave functions, Hartree-Fock (HF) or Hartree-Fock-Slater (HFS) wave functions, variable screening model (VSM) wave functions, and two-center Dirac wave functions.

A basic approximation made in most MO x-ray calculations, independent of whether one-electron or many-electron HF wave functions are used, is the treatment of the many-electron problem as a one-electron or one-hole problem. Even when electronic configurations or electron occupancies are considered (Anholt, 1978a; Briggs *et al.*, 1979), multiplet structure is never taken into account. This is partly because the multiplet energy splittings are negligible compared to the energy uncertainty due to collision broadening. As a consequence, the transition rates can be considered as sums of one-electron rates; the possibility that, say, a double-hole configuration may couple into a forbidden decay state, seriously affecting the transition probabilities, is never considered.

The Hamiltonian for a single electron is given in the nonrelativistic case by

$$H_i=-\frac{\nabla_i^2}{2}-\frac{Z_i}{\left|\mathbf{r}_i-\frac{\mathbf{R}}{2}\right|}-\frac{Z_2}{\left|\mathbf{r}_i+\frac{\mathbf{R}}{2}\right|}+\sum_{j\neq i}\frac{1}{|\mathbf{r}_i-\mathbf{r}_j|}\ , \tag{3.49}$$

where H_i differs from that given in Eq. (3.33) by the inclusion of the electrostatic term proportional to $|\mathbf{r}_i-\mathbf{r}_j|^{-1}$. One-electron wave functions are obtained by solving this Hamiltonian with the omission of this term. The exact solution of the nonrelativistic, two-center, one-electron problem in prolate spheroidal coordinates is discussed by Bates *et al.* (1953), Slater (1963), and Helfrich and Hartmann (1970). The prolate spheroidal coordinates are defined by

$$\xi=\frac{r_1+r_2}{R},\quad \eta=\frac{r_1-r_2}{R},\quad \varphi\ ,$$

where r_1 and r_2 are shown in Fig. 4. The Hamiltonian, Eq. (3.33), is then separable in these coordinates:

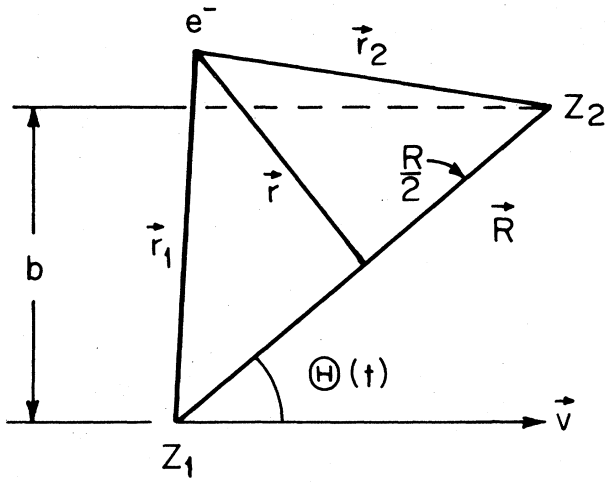

FIG. 4. The molecular-based coordinate system, showing the position of the projectile nucleus Z_1, the target nucleus Z_2, and the active electron e^-.

$$\left[\frac{d}{d\xi}\left[(\xi^2-1)\frac{d}{d\xi}\right]+\left[\Lambda+2R\xi-p^2\xi^2-\frac{m^2}{\xi^2-1}\right]\right]\chi=0\,,$$

$$\left[\frac{d}{d\eta}\left[(1-\eta^2)\frac{d}{d\eta}\right]+\left[-\Lambda+p^2\eta^2-\frac{m^2}{1-\eta^2}\right]\right]\chi=0\,, \tag{3.50}$$

so the MO wave function can be written as the product

$$\chi_{\rm MO}(\mathbf{r},R)=L(\xi)M(\eta)e^{im\varphi}\,. \tag{3.51}$$

The wave functions L and M are then expanded according to

$$M=\sum_s f_s(\Lambda,m,p)P^m_{m+s}(\eta)\,,$$

$$L=(\xi^2-1)^{m/2}(\xi+1)^{\sigma}e^{-p\xi}\sum_t g_t\left[\frac{\xi-1}{\xi+1}\right]^t\,,$$

where $\sigma=R/p-m-1$. Insertion into Eq. (3.50) gives a tridiagonal matrix equation for the expansion coefficients f and g of the type

$$\mathbf{A}f=\Lambda f \quad\text{and}\quad \mathbf{B}g=-\Lambda g\,. \tag{3.52}$$

These are two coupled nonlinear eigenvalue equations to be solved simultaneously in the eigenvalues Λ (the separation constant) and $p=-R^2\varepsilon_i/4$, where ε_i is the molecular binding energy. The equations are solved by a Newton-Raphson algorithm (Helrich and Hartmann, 1970). One makes an initial guess for the values of p and Λ, calculates the determinant of $\mathbf{A}-\Lambda\mathbf{1}$ and $\mathbf{B}+\Lambda\mathbf{1}$ and the derivatives of the determinants with respect to Λ and p, then calculates new values of Λ and p until convergence is obtained. In practice, one begins the calculation of the correlation diagram at small internuclear distances where Λ and p can be inferred from their UA values. For every step taken in R, the initial guess for p and Λ is obtained by extrapolating previous values, so the convergence of the iterations is very fast (one to three passes for a relative precision of 10^{-7}). Reasonably accurate initial values of Λ and p are required, because convergence onto incorrect values of Λ and p is easily possible, especially in regions of the correlation diagrams of high molecular level density.

The nonrelativistic hydrogenic molecular wave functions are useful for interpreting many heavy-ion—atom collisions with medium heavy projectiles and target atoms with $10\lesssim Z_1,Z_2\lesssim 50$. However, they cannot be used for superheavy quasimolecules with $Z_1+Z_2>130$, which are of interest because of possible spontaneous positron production (Müller, 1976) and the possibility of measuring superheavy binding energies. For this reason, Müller and Greiner (1976) solved the relativistic, one-electron, two-center problem for which the electronic Hamiltonian for the ith electron is given by

$$H=c\boldsymbol{\alpha}\cdot\mathbf{p}+\beta mc^2-\frac{Z_1}{\left|\mathbf{r}-\frac{\mathbf{R}}{2}\right|}-\frac{Z_2}{\left|\mathbf{r}+\frac{\mathbf{R}}{2}\right|}\,, \tag{3.53}$$

where $\boldsymbol{\alpha}$ and β are Dirac matrices (Schiff, 1968). The Schrödinger equation with this Hamiltonian is likewise solved in prolate spheroidal coordinates; unfortunately, unlike for the nonrelativistic one-electron Hamiltonian, the Dirac Hamiltonian is not exactly separable, except in the equation for φ. The four-component MO wave functions are solved by expanding in a Hylleraas (1931) basis set

$$\chi^m_s=\sum_{n,l}c_{nl}\psi^m_{nls}\,,$$

with

$$\psi^m_{nls}=e^{-x/2}L_n^{m\pm1/2}(x)P_l^{m\pm1/2}(\eta)\varphi(s)\,, \tag{3.54}$$

where $x=(\xi-1)/a$, a is a convergence parameter, $L_n^m(x)$ are associated Laguerre polynomials, P_l^m are associated Legendre polynomials, and $\varphi(s)$ is the spin wave function. Taking the matrix elements of the two-center Dirac Hamiltonian, one obtains an eigenvalue equation

$$\mathbf{H}_{\rm TCD}\mathbf{C}=E\mathbf{S}\mathbf{C}\,, \tag{3.55}$$

where $\mathbf{S}$ is the overlap matrix. $\mathbf{H}_{\rm TCD}$ is then diagonalized, so one obtains in addition to the eigenvectors $\mathbf{C}$ describing the molecular states, eigenvalues ε_n relating to the electronic binding energy.

As $j=\frac{1}{2}$ eigenstates of the atomic Hamiltonian with the point nuclear potentials described by the potentials in Eq. (3.53) cease to exist for $Z>137$, finite-nuclear-size potentials must be used. For a homogeneous spherical nuclear-charge distribution, the electronic potential is given by

$$\frac{Z_i}{r_i}\rightarrow\begin{cases}-\dfrac{Z_i}{2R_N}\left[3-\left[\dfrac{r_i}{R_N}\right]^2\right] & \text{for } r_i<R_N\\[2ex] -\dfrac{Z_i}{r_i} & \text{for } r_i>R_N\,,\end{cases} \tag{3.56}$$

where R_N is the nuclear radius of either the projectile or the target nucleus. For atoms, the use of finite-nuclear-size potentials alters the point where the $1s$ energy level dives into the Dirac negative-energy sea from $Z=137$ to $Z\sim 170$. Likewise, the $1s\sigma$ binding energy exceeds $2mc^2$ at $R\approx 0$ for collisions with $Z_1+Z_2>170$.

The nonrelativistic and Dirac two-center wave functions neglect electronic electrostatic repulsion terms, which tend to lower electron binding energies. These effects are most important in collisions with low UA charges or for the outer-shell molecular binding energies. To account for electrostatic repulsion approximately, Eichler and Wille (1974,1975) developed a variable screening model (VSM) based on the Thomas-Fermi quasi-one-electron model. Because of electrostatic repulsion, an electron in an atom sees, instead of the full nuclear charge Z, a smaller screened nuclear charge Z^*, depending on whether it is an inner-shell electron closest to the nucleus ($Z\sim Z^*$) or an outer-shell electron furthest from the nucleus ($Z^*\ll Z$). Therefore, instead of including the electrostatic terms exactly, the Thomas-Fermi approach reduces the electron-nuclear potential, using the function $\Phi(x)$ below, which depends on the relative distance between the electron and the nucleus.

The application of the Thomas-Fermi model to molecular wave functions requires the interpolation, using the functions f_i and y_i given below, between the screening of the UA charge Z_1+Z_2 at $R=0$ and the screening of the SA charges Z_1 or Z_2 at large internuclear distances. The potentials $V_1\sim Z_1/r_1$ and $V_2\sim Z_2/r_2$ in Eq. (3.33) are replaced by

$$V_i=\begin{cases} -\dfrac{Z_i}{r_i}\left[\Phi(x_i)+\dfrac{3\sqrt{2}}{4\pi}[r_i f_i \Phi(x_i)]^{1/2}\right] & \\ \qquad\qquad \text{if } |V_i|>\dfrac{Z_i}{r_i}f_i & \\ -\dfrac{Z_i}{r_i}f_i \quad \text{otherwise}, & \end{cases} \tag{3.57}$$

where

$$\begin{aligned} x_i&=\frac{r_i Z_i^{1/3}}{0.8853}\frac{\lambda^2+y_i^{1/2}\rho_i}{\lambda^2+\rho_i^2}, \\ y_i&=\frac{Z_u}{Z_i}, \\ \rho_i&=\frac{r_i}{R}, \\ f_i&=\frac{1}{Z_i}\frac{\lambda^2+\rho_i^2}{\lambda^2+y_i\rho_i^2}, \end{aligned} \tag{3.58}$$

Φ is an analytical function given by

$$\begin{aligned}\Phi(x)=&(1+0.027\,47\sqrt{x}+1.243x-0.1486x^{3/2} \\ &+0.2302x^2+0.007\,298x^{5/2}+0.006\,944x^3)^{-1},\end{aligned} \tag{3.59}$$

and λ^2 is a parameter between 3 and 3.5. Note that as $r_i\to 0$, $\Phi(x)\to 1$, and $V_i\to -Z_i/r_i$, so the electron correctly sees an unscreened charge. If $r_i\gg R$, however, x_i approaches $r_i(Z_1+Z_2)^{1/3}/0.8853$, hence the electron sees a screened UA.

The VSM Schrödinger equation is solved in prolate spheroidal coordinates, but is not separable in these coordinates, so the solutions are expanded in a Hylleraas basis set. The Hamiltonian is diagonalized to obtain the eigenvectors and molecular binding energies. Perturbative relativistic effects have been incorporated into the VSM by Kaufman and Wille (1976).

Molecular Hartree-Fock (HF) and relativistic Hartree-Fock-Slater (RHFS) wave functions account for the electron repulsion contribution to the Hamiltonian [Eq. (3.49)]. The MO wave functions are expanded in atomic wave functions centered on both nuclei Z_1 and Z_2 (or on one center in between)

$$\chi_i(\mathbf{r},R)=\sum_{k=1}^{m} c_{ki}u_k(\mathbf{r}), \tag{3.60}$$

where c_{ki} are expansion coefficients obtained by diagonalization. The matrix elements of the two-center Hamiltonian are given by

$$\begin{aligned}H_{nk}=&\int u_n^*(\mathbf{r}_i)\left[-\frac{\nabla^2}{2}-\frac{Z_1}{r_{1i}}-\frac{Z_2}{r_{2i}}\right]u_k(\mathbf{r}_i)d^3\mathbf{r}_i \\ &+\sum_{j=1}^{N}\sum_{p,q=1}^{m}2c_{pj}^*c_{qj}(\langle nk\,|\,pq\rangle-\tfrac{1}{2}\langle np\,|\,kq\rangle),\end{aligned} \tag{3.61}$$

where N is the number of electrons, and the electron-electron repulsion matrix elements are given by

$$\begin{aligned}\langle nk\,|\,pq\rangle=&\int\int u_n^*(\mathbf{r}_i)u_k(\mathbf{r}_i)\,|\,\mathbf{r}_i-\mathbf{r}_j\,|^{-1} \\ &\times u_p^*(\mathbf{r}_j)u_q(\mathbf{r}_j)d^3\mathbf{r}_i d^3\mathbf{r}_j.\end{aligned} \tag{3.62}$$

In this approach, the Hamiltonian H_{nk} depends on the eigenvectors c_{qi}, which are then formed by diagonalizing H_{nk}. To obtain a self-consistent set of eigenvalues and eigenvectors, one initially guesses at the eigenvectors (e.g., by diagonalizing the Hamiltonian, omitting the $\langle nk\,|\,pq\rangle$ terms), then calculates H_{nk} and diagonalizes to obtain a new set of vectors, and so on until the eigenvalues converge. For low-Z_u molecules, quantum chemists have developed several efficient HF codes, e.g., POLYATOM (Dunning, 1970), which have been used in a number of MO x-ray and other molecular model calculations (Larkins, 1972; Briggs and Hayns, 1973; Albat *et al.*, 1975).

For high-Z_u collisions, RHFS wave functions are available (Rosen and Ellis, 1974,1975). The RHFS Hamiltonian is given by

$$H_i=c\alpha_i\cdot\mathbf{p}_i+\beta_i mc^2-\frac{Z_1}{r_{1i}}-\frac{Z_2}{r_{2i}}+V_{ee}(\mathbf{r}_i)+V_{\text{exc}}(\mathbf{r}_i), \tag{3.63}$$

where the first four terms are identical to those in Eq.

(3.53), and the electron-electron repulsion term has been written as the sum of a term V_{ee} given by

$$V_{ee}(\mathbf{r}) = \int d^3\mathbf{r}'\rho(\mathbf{r}')\,|\,\mathbf{r}-\mathbf{r}'\,|^{-1}, \tag{3.64}$$

and an exchange term which can be written as

$$V_{\rm exc}(r) = -3C\left[\frac{3\rho(r)}{8\pi}\right]^{1/3}, \tag{3.65}$$

where C is a parameter between $\frac{2}{3}$ and unity. These two terms originate from the two repulsion terms in the HF equations, Eq. (3.61), coming from the direct repulsion between two electrons V_{ee} and the exchange between two electrons in the matrix element $\langle np\,|\,kq\rangle$. As in the HF method, the wave functions are expanded in atomic orbitals centered on the nuclei Z_1 and Z_2, and eigenvectors are obtained by diagonalizing the Hamiltonian matrix. A self-consistent field iteration is also required because the electron densities $\rho(r)$ depend on the eigenvectors. The electron-nuclear potentials may also be modified to include finite nuclear size, as in Eqs. (3.56). These MO energies have been used in MO x-ray calculations by Fricke *et al.* (1976) and Hartung *et al.* (1979).

2. Correlation diagrams

Figures 5—8 show correlation diagrams for Kr + Xe collisions, calculated with nonrelativistic one-electron wave functions (Fig. 5), for Kr + Xe with VSM wave functions (Fig. 6), for Xe + Ag with RHFS wave functions (Fig. 7), and for Pb + Pb with relativistic two-center Dirac wave functions (Fig. 8). The molecular energy levels are denoted differently in the various diagrams. For hydrogenic wave functions, the MO energy levels are denoted by σ, π, or δ, depending on the m quantum number (0, 1, or 2) and by the UA orbital to which the level correlates, $1s$, $2p$, $2s$, $3d$, etc. [Also, in collisions with $Z_1 = Z_2$ the orbitals can either be symmetric (gerade) or antisymmetric (ungerade) with respect to a plane perpendicular to the internuclear axis.] In the VSM calculations, the orbitals are numbered from bottom (higher binding energy) to top according to the m quantum number and the g and u symmetry in symmetric collisions. This scheme is also used in the Xe + Ag RHFS diagram. For one-electron relativistic MO's, Müller and Greiner (1976) denote the MO's by the UA j value, e.g., $2p\frac{1}{2}$, because the spin-orbit splitting is larger than the electrostatic σ-π splittings. Orbitals with good j values can have m_j values between $+j$ and $-j$. Orbitals with $m_j = \pm\frac{1}{2}$ are denoted by σ's; orbitals with $m_j = \pm\frac{3}{2}$ are denoted by π's, and so on.

The main qualitative difference between these correlation diagrams concerns the crossings or avoided crossings between various molecular energy levels. The hydrogenic $2s\sigma$ and $3d\sigma$ energy levels cross, but the same but other-

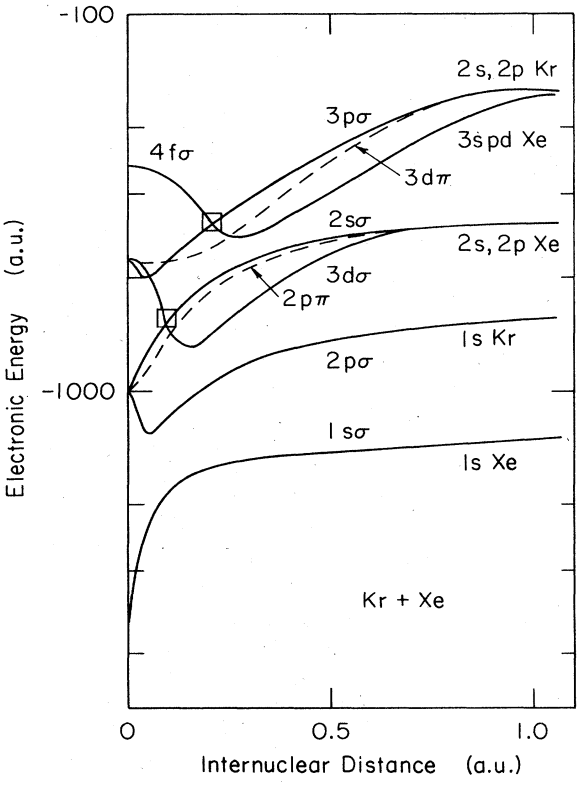

FIG. 5. A one-electron correlation diagram for Kr + Xe collisions, as in Fig. 1. The solid lines are for σ MO's, and the dashed lines are for π MO's. The boxes correspond to regions of interest noted in Fig. 6.

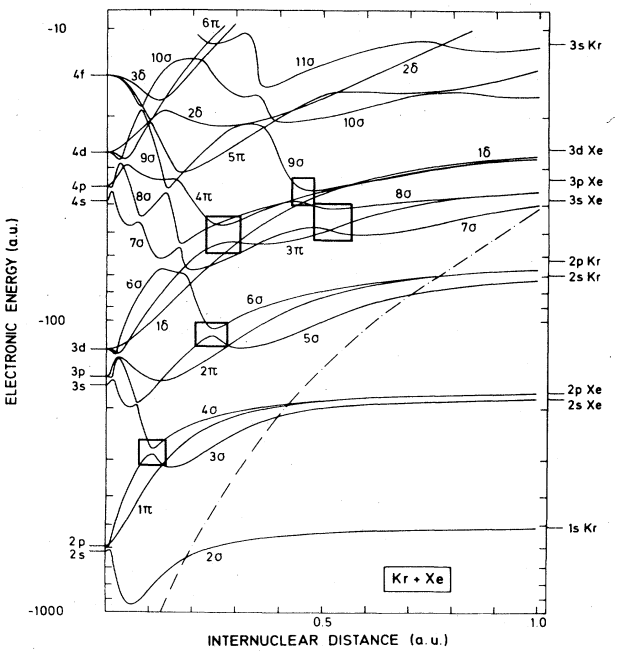

FIG. 6. A variable screening model correlation diagram for Kr + Xe collisions (Eichler *et al.*, 1976). The avoided crossings between the 3σ and 4σ and the 5σ and 6σ curves, which are marked by boxes, are not predicted by the correlation rules of Barat and Lichten. The height of the potential barrier between the two nuclei is given by the dot-dashed curve. The region below this curve may be called "atomic" and the region above the curve "molecular" (Eichler and Wille, 1975).

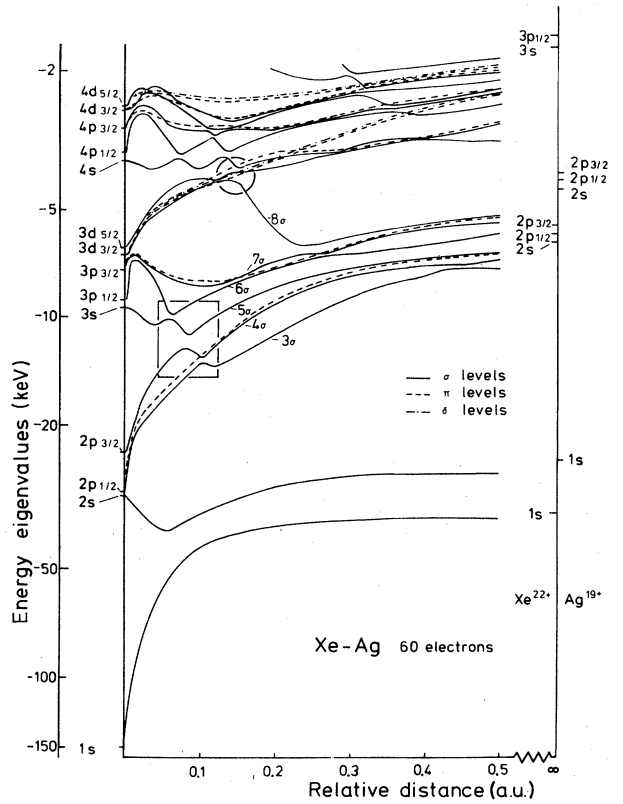

FIG. 7. A self-consistent relativistic correlation diagram for Xe + Ag collisions with 60 electrons. The σ levels are drawn as solid curves, the π levels as dashed curves, and the δ levels as dot-dashed curves. In the box, the 3σ-4σ crossing is avoided, as in the VSM calculations, Fig. 6 (from Morovic *et al.*, 1977).

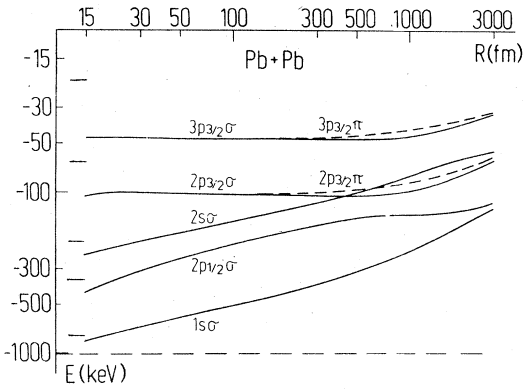

FIG. 8. Correlation diagram for Pb + Pb collisions (Müller and Greiner, 1976). The horizontal lines at $R=15$ fm represent the screened values of the united-atom energies (Fricke and Soff, 1977). Here, the solid lines show levels with $m_j=\pm\frac{1}{2}$, and the dashed lines show levels with $m_j=\pm\frac{3}{2}$.

wise denoted 3σ and 4σ energy levels in the asymmetric VSM, TCD, and RHFS diagrams (also called the $2\sigma_g$ and $3\sigma_g$ levels in the symmetric diagrams) undergo avoided crossings. Avoided crossings are seen in degenerate perturbation theory. When two levels mix by a perturbative potential, the levels repel one another, so there is never a point where the energy difference is zero. This mixing occurs automatically in the VSM, HF, RHFS, and TCD calculations, where exact solutions to the respective Hamiltonians are not possible to obtain. If the MO wave functions are expanded in a set of basis functions, Hylleraas or atomic, avoided crossings are always seen. One can interpret the crossings as being due to the perturbative electrostatic repulsion interaction in the low-Z_u collisions (Eichler *et al.*, 1976) or spin-orbit, Darwin, or relativistic kinetic energy interactions in the TCD diagrams (Müller and Greiner, 1976). Fewer avoided crossings are seen in symmetric collisions where g and u MO's do not mix.

In a collision, adiabatic levels showing avoided crossings will remix due to the dynamic Coriolis or radial coupling interactions

$$H_{\rm dyn}=\dot{\Theta}\frac{\partial}{\partial\Theta}+\dot{R}\frac{\partial}{\partial R}\ . \tag{3.66}$$

An electron in, say, a 3σ MO in Kr + Xe collisions can make a Landau-Zener transition (Zener, 1932) to the 4σ MO. In this case, the orbitals are coupled via the radial coupling operator. In MO x-ray calculations for a transition to the 3σ MO, we must consider transitions to both the 3σ and 4σ MO's, writing two coupled MO's as

$$\begin{aligned}\Psi_a&=a_{3\sigma,a}(t)\chi_{3\sigma}+a_{4\sigma,a}\chi_{4\sigma}\ ,\\ \Psi_b&=a_{3\sigma,b}(t)\chi_{3\sigma}+a_{4\sigma,b}\chi_{4\sigma}\ ,\end{aligned} \tag{3.67}$$

TABLE I. Landau-Zener parameters and the critical velocity v_c above which the crossing is diabatic (see text) for the $2\sigma_g$-$3\sigma_g$ crossing in Ne+Ne, Ar + Ar, Kr + Kr, and Xe + Xe collisions and the 3σ-4σ crossing in Kr + Xe (Eichler *et al.*, 1976). The values of the crossing radius R_c and the coupling matrix element H_{12} were taken from the adiabatic VSM calculations. The energy corresponding to the critical velocity and typical energies where $1s\sigma$ MO x-ray measurements have been made are shown. All quantities are in atomic units, except as noted.

	R_c	H_{12}	v_c	E_c (keV)	$E_{\rm MO}$
^{20}Ne+Ne	0.560	0.55	0.12	7	> 100 keV
^{40}Ar+Ar	0.271	1.1	0.07	5	> 5 MeV
^{84}Kr+Kr	0.124	2.2	0.023	1.1	> 30 MeV
^{136}Xe+Xe	0.08	3.0	0.013	0.57	> 100 MeV
^{84}Kr+Xe	0.107	3.5	0.04	3.3	> 100 MeV

where the mixing coefficients are obtained from equations similar in character to Eq. (3.44) with the Coriolis operator replaced by the radial operator.

Eichler *et al.* (1976) have analyzed the 3σ-4σ or $2\sigma_g$-$3\sigma_g$ crossings in detail and have calculated, with the Landau-Zener formula, the ion velocity at which $|a_{3\sigma,a}(t)|^2$ or $|a_{4\sigma,a}(t)|^2$ vary by more than one-half across the crossing. Their results, shown in Table I, indicate that this velocity is much smaller than those being used to study $1s\sigma$ MO x-ray production, indicating that at the avoided crossing t_x one can assume that the amplitudes are step functions:

$$\Psi_a = \begin{cases} \chi_{3\sigma} & \text{for } t < t_x \\ \chi_{4\sigma} & \text{for } t > t_x \end{cases}, \tag{3.68}$$

and similarly for Ψ_b. Thus the orbitals cross and the appropriate "diabatic" MO's are either hydrogenic orbitals (Fig. 5) or orbitals interpolated across avoided crossings (diabatized orbitals). For a complete description of the diabatization procedure, see Taulbjerg and Briggs (1975).

Hydrogenic MO's have the desired feature that the orbitals freely cross, so that the diabatization procedures are unnecessary. The disadvantage, that the hydrogenic energies do not account for relativistic or screening effects, can be ameliorated, except for outer-shell MO's and in high-Z_u collisions, by adjusting the one-electron energies using measured atomic binding and transition energies.

3. Molecular x-ray transition rates

In prolate spheroidal coordinates with the origin of the electron coordinate shown in Fig. 4, the dipole transition matrix element is given by

$$\langle \chi_i(\mathbf{r},\mathbf{R}) \,|\, \mathbf{r} \,|\, \chi_f(\mathbf{r},\mathbf{R}) \rangle = \frac{R}{2} \int \left[\frac{R^3}{8} (\xi^2-\eta^2) d\xi\, d\eta\, d\varphi \right] L_i(\xi) M_i(\eta) L_f(\xi) M_f(\eta)$$
$$\times \exp[i(m_i - m_f)\varphi][\xi\eta\hat{\mathbf{R}} + \cos\varphi B\hat{\mathbf{R}}_x + \sin\varphi B\hat{\mathbf{R}}_y] , \tag{3.69}$$

where $B=[(1-\eta^2)(\xi^2-1)]^{1/2}$. The first term in large parentheses is the volume element, and the wave functions are given by Eq. (3.51). The transition dipole matrix element $\langle \,|\, \mathbf{r} \,|\, \rangle$ will be parallel to $\hat{\mathbf{R}}$ if $m_f = m_i$ (e.g., σ-σ or π-π transitions) and perpendicular to $\mathbf{R}$ (parallel to $\hat{\mathbf{R}}_x$ or $\hat{\mathbf{R}}_y$) if $m_f - m_i = \pm 1$ (σ-π or π-δ transitions). Also, one usually combines the π orbitals into π_x and π_y orbitals, so that

$$\exp(\pm i\varphi) \rightarrow \cos\varphi \text{ or } \sin\varphi . \tag{3.70}$$

The π_x-σ element will then be parallel to $\hat{\mathbf{R}}_x = \hat{\mathbf{b}}$ and the π_y-σ element to $\hat{\mathbf{R}}_y = \hat{\mathbf{y}}$. These considerations have already been used in deriving Eq. (3.46). Although hydrogenic MO wave functions are used in Eq. (3.69), similar expressions can be used with TCD, VSM, HF, and RHFS wave functions.

Decay rates for $1s\sigma$ vacancies in Br + Zr collisions and $2p\sigma$ vacancies in Xe + Sn collisions are shown in Figs. 9 and 10. The behavior of these transition rates at small R can be understood by comparison with UA transition rates (Bethe and Salpeter, 1957; Scofield, 1969). The atomic $2p \rightarrow 1s$ and $3p \rightarrow 1s$ x rays are most intense, so the $2p\pi$, $2p\sigma$, $3p\sigma$, and $3p\pi \rightarrow 1s\sigma$ transition rates are largest at small R in Fig. 9. Since the $3d \rightarrow 1s$ and $2s \rightarrow 1s$ transitions in atoms are very weak, the $3d\sigma \rightarrow 1s\sigma$, $3d\pi \rightarrow 1s\sigma$, and $2s\sigma \rightarrow 1s\sigma$ transition rates are near zero at small R, but become larger as these levels approach Stark-mixed $2s$-$2p$ levels at large R. The $3p\sigma \rightarrow 1s\sigma$ rate has a node; the matrix element changes sign at intermediate internuclear distances. For $2p\sigma$ MO x rays (Fig. 10), the $3d \rightarrow 2p$ and $4p \rightarrow 2p$ atomic transition rates are largest, so the $3d\sigma,\pi \rightarrow 2p\sigma$ and $4d\sigma,\pi \rightarrow 2p\sigma$ are largest at small R. Although $3s \rightarrow 2p$ and $4s \rightarrow 2p$ transitions are allowed in atoms, their matrix elements are not very large, so the $3s\sigma \rightarrow 2p\sigma$ and $4s\sigma \rightarrow 2p\sigma$ rates are small at small R.

Comparison of molecular transition rates indicates which MO x-ray transitions can be neglected in practical calculations. The best rule one can deduce is that the MO x-ray transition should be included if the corresponding UA x-ray intensity is significant. For example, $K\alpha(2p \rightarrow 1s)$ and $K\beta$ $(3p \rightarrow 1s)$ x rays are the most intense features in atomic x-ray spectra, hence inclusion of the $2p\sigma$, $2p\pi$, $3p\sigma$, and $3p\pi$ MO's to calculate $1s\sigma$ MO x rays is required; the $3p$ MO's may be less important in low-Z_u ($\lesssim 30$) collisions; the $4p$ MO's may be important in high-Z_u ($\gtrsim 130$) collisions, and even $2s\sigma$-$1s\sigma$ transitions must be included if $Z_u > 160$ (Anholt and Rasmussen, 1974; Kirsch *et al.*, 1978). Inclusion of, say, $3d\sigma \rightarrow 1s\sigma$ transitions, which are important at large R, affects only the x-ray region near the SA K x-ray lines, which is generally obscured by continuum emission from other processes.

Atomic $L\alpha$ and $L\beta$ x rays from $3d \rightarrow 2p$ and $4d \rightarrow 2p$ transitions are the most prominent features in L x-ray spectra, thus $3d\sigma,\pi,\delta \rightarrow 2p\sigma,\pi$ and $4d\sigma,\pi,\delta \rightarrow 2p\sigma,\pi$ transitions should be included in calculations of $2p\sigma$ and $2p\pi$ MO x rays. The $4d$ transitions may be of less importance for $Z_u < 80$. The $3p \rightarrow 2p$ and $4p \rightarrow 2p$ transition rates are large at large R, but these only affect the MO x-ray intensity near the SA L x-ray lines. The $3s \rightarrow 2p$ and $4s \rightarrow 2p$ transition rates are an order of magnitude smaller than the $3d \rightarrow 2p$ rates, and hence can be neglected. One can predict that MO x-ray transitions to the $2s\sigma$ MO are unimportant because the $2s$ fluorescence yield is so small

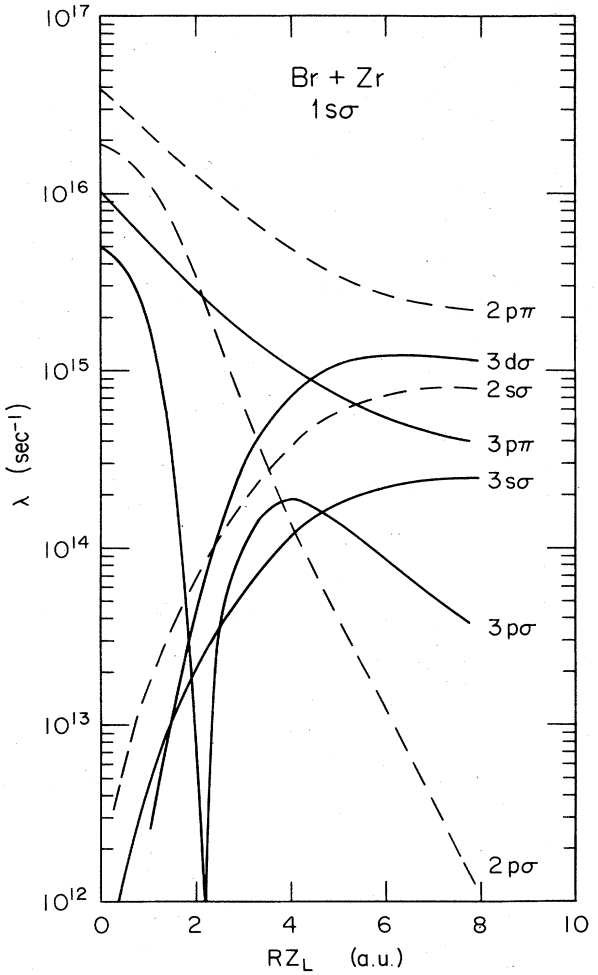

FIG. 9. Electronic radiative transition rates to single vacancies in the $1s\sigma$ MO in Br + Zr collisions. The dashed lines indicate transitions from the $2s$ and $2p$ MO's, and the solid lines transitions from $3s$, $3p$, and $3d$ MO's.

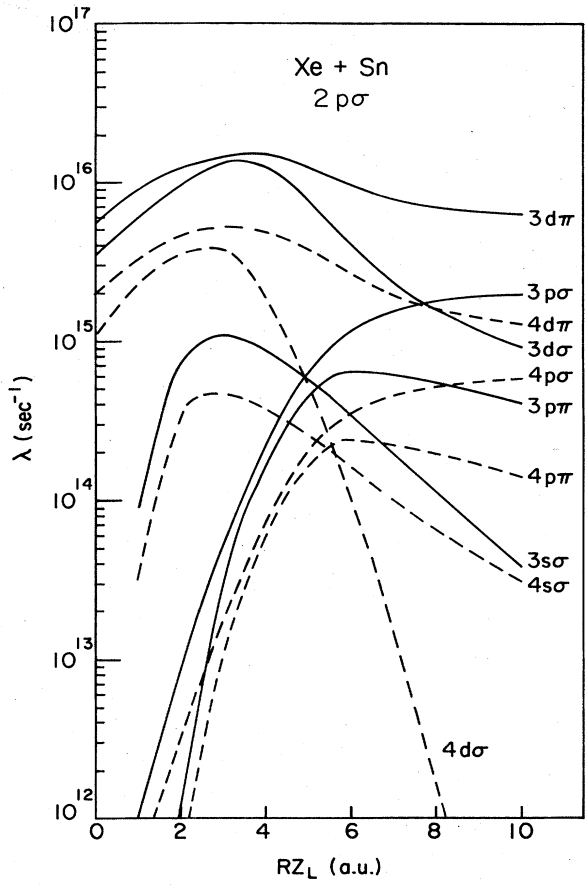

FIG. 10. Electronic radiative transition rates to single vacancies in the $2p\sigma$ MO in Xe + Sn collisions. The solid lines indicate transitions from the $3s$, $3p$, and $3d$ MO's, and the dashed lines transitions from $4s$, $4p$, and $4d$ MO's (Anholt and Meyerhof, 1977).

in atoms. In atoms, most of the L x rays seen are transitions to $2p$ vacancies. This occurs because the Koster-Kronig transitions transfer the $2s$ vacancy to the $2p$ levels before it radiates. Whether this is true in molecules, however, is not known. Such an argument is the basis of the claim by Saris *et al.* (1972) to have seen $2p\pi$ MO x rays in Ar + Ar collisions, neglecting the nearby presence of the $2s\sigma$ MO.

IV. X-RAY CROSS-SECTION MEASUREMENTS

A. Measuring continuum radiation

X-ray continua can be measured like SA x-ray production cross sections, using either beam current integration [Fig. 11(a); Merzbacher and Lewis, 1958] or Rutherford scattering normalization techniques [Fig. 11(b); McDaniel *et al.*, 1977]. With beam current integration, a beam enters an electrically isolated chamber through several collimators, impinging on a target viewed by an energy-dispersive x-ray detector such as a lithium-drifted silicon, a lithium-drifted germanium, an intrinsic Ge, a proportional counter, or a NaI x-ray detector. The detector produces an electrical pulse proportional to the x-ray energy, which is measured by an analog-to-digital converter (ADC) and counted in a channel or a memory location in a multichannel analyzer or computer, so one obtains an x-ray spectrum like that in Fig. 12. The number of projectiles incident on the target are counted by the charge collected on the chamber Q (in coulombs). An electron suppressor ring with voltage between -200 and -1000 V allows projectiles into the chamber, but keeps charged secondary electrons from leaving it. Since the SA x-ray intensity is usually orders of magnitude higher than the continuum x-ray intensity, an absorber is placed between the chamber and x-ray detector to attentuate low-energy x

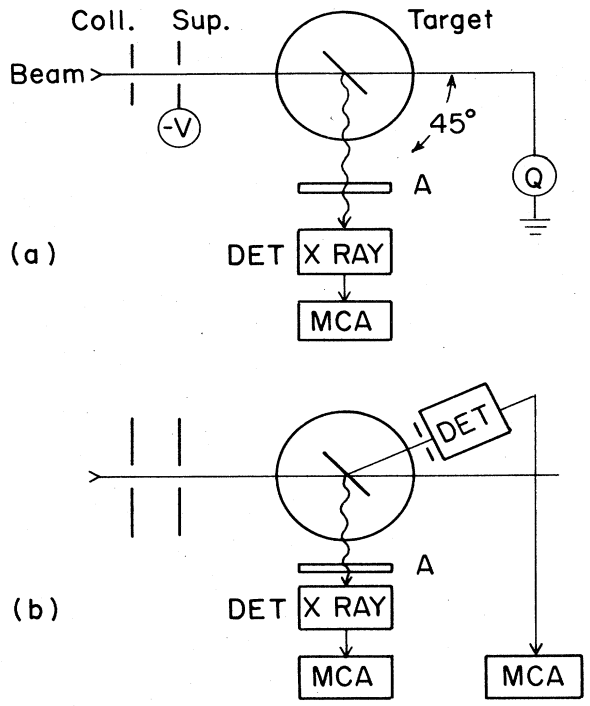

FIG. 11. Schematic diagram of apparatus used to measure MO x rays: (a) for measuring thick-target yields or beam current normalization; (b) for Rutherford scattering normalization, where a particle detector (DET) is shown at approximately 30°. Abbreviations: Collimator (Coll.), Electron Suppressor (Sup.) with $V=-200$ to -1000 V, beam current integrator (Q), x-ray detector (DET), multichannel analyzer or computer (MCA), x-ray attenuator (A).

rays by orders of magnitude while attenuating the higher-energy continuum x-ray intensity by a small factor (Fig. 12). It is a good practice to ensure the purity of the absorber material (Meyerhof *et al.*, 1973 erratum) by calibrating the attenuation factor $A=\exp[+\mu(E_x)x]$ with radioactive sources, where μ is the x-ray absorption cross section (McMaster *et al.*, 1969) and x is the absorber thickness. Because the electron pulses from the x-ray detector have a finite time width, they can add together before being measured by the ADC, which, for high counting rates, can produce a background continuum spectrum. The attenuator keeps the x-ray counting rate sufficiently small (<400 Hz) to prevent this electronic pulse pileup. Pileup rejectors, which inspect the fast electronic pulse train and reject pulses when pileup occurs, have also been used.

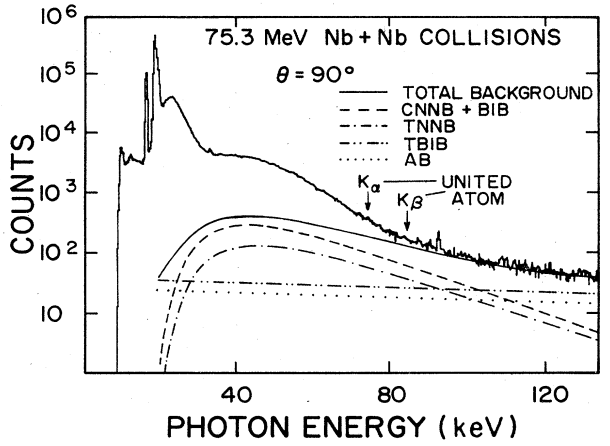

FIG. 12. MO x-ray spectrum seen in 75.3-MeV Nb + Nb collisions at a detector angle of 90° (Vincent, 1977). Continua from the room background (AB), target NNB (TNNB), target beam-induced background (TBIB), and carbon-backing NNB and beam-induced backgrounds (CNNB + BIB) are shown. The $1s\sigma$ MO x-ray spectrum of interest extends from approximately 30 keV to the position of the UA $K\alpha$ and $K\beta$ x-ray lines.

The continuum x-ray cross section, differential in x-ray energy, is obtained from the yield or the number of photons per projectile using

$$\frac{d\sigma^2(E_x,\theta)}{dE_x d\Omega}=\frac{d^2Y(E_x,\theta)}{dE_x d\Omega}\frac{1}{n_2 T}\ , \tag{4.1}$$

where n_2 is the target-atom density and T is the target thickness (for thick targets, see below). The yield is calculated from the number of counts per channel C, using

$$\frac{d^2Y}{dE_x d\Omega}=\frac{Cq}{cQ}D\frac{A}{\varepsilon d\Omega_x}a\ , \tag{4.2}$$

where q is the charge on each projectile, $c=6.25\times10^{18}$ charges per coulomb, a is the number of channels per unit energy E_x (since C is the number of counts per channel), D is the dead-time correction factor of the electronic counting system, and $\varepsilon d\Omega_x$ is the photoelectric efficiency and solid angle of the x-ray detector, obtained from counting a known intensity of x rays and low-energy γ rays from radioactive sources placed at the target position. Usually $d\Omega_x$ is the fraction of 4π sr subtended by the x-ray detector, so the MO x-ray cross section has the units of per 4π sr. The x-ray detector efficiency is less easily determined for high-energy (>100 keV) MO x rays. If the photoelectric absorption cross section for a photon of energy E_x in the detector material (Si, Ge, or NaI, or proportional counter gas) is much larger than the Compton scattering cross section, one can unambiguously identify an electronic pulse of relative energy E_x with a photon of energy E_x. However, if photons Compton scatter in the detector, leaving only part of their energy, a nontrivial unfolding of the continuum spectrum is required (Meyerhof *et al.*, 1979; Stoller *et al.*, 1980).

One can also measure a continuum x-ray spectrum by Rutherford scattering normalization, Fig. 11(b). Here one measures with a thin target the number of x rays (C_x in counts per channel) and simultaneously the total number C_p of projectiles elastically scattered into an angle Θ. C_p is proportional to the Rutherford scattering cross section $d\sigma_R(\Theta)/d\Omega$. The MO x-ray production cross section is derived from

$$\frac{d^2\sigma(E_x,\theta)}{dE_x d\Omega}=\frac{d\sigma_R}{d\Omega}\frac{C_x}{C_p(\Theta)}\frac{D_x}{D_p}\frac{\Delta\Omega_p A a}{\varepsilon d\Omega_x}\ , \tag{4.3}$$

where $\Delta\Omega_p$ is the solid angle subtended by the particle detector. It is sometimes possible to multiplex the x-ray

and particle-detector pulses through the same electronic counting system (MCA), so that the x-ray and particle dead times D_x and D_p are identical. This method is preferred to the beam current integration method, because measuring low beam currents accurately is somewhat difficult, and knowledge of the target thickness T is not required. As the Rutherford cross section varies rapidly with the scattering angle Θ, a careful measurement of the angle is required, usually by measuring $C_p(\Theta)$ on either side of the beam axis. One must ensure, as well, that nuclear reactions do not take place at the angle Θ.

Thin targets with the Rutherford scattering normalization method have been used only in a few cases for measuring MO x rays. Molecular-orbital x-ray production cross sections are small, so the use of thicker targets is advantageous, especially if room x-ray background is significant. In angular distribution measurements with thin targets, the beam emerging from behind the target must be disposed of without increasing the continuum x-ray background and without preventing x-ray measurements at small angles or very large angles. This obstacle is not present if the beam stops in a thick target. Greenberg and Vincent (Vincent, 1977) use relatively thin targets ($\sim 100\ \mu g/cm^2$) on infinitely thick carbon backings, so the beam is disposed of in the backing without severely increasing the beam-induced backgrounds. Also, since this backing material does not attenuate the MO x rays of interest, the x-ray detector can view the target at any angle.

Many experimenters (Meyerhof *et al.*, 1974,1979; Anholt, 1978b) use targets thick enough to stop the beam. There are two ways of interpreting thick-target measurements. By measuring thick-target yields at several beam energies E, one can convert the yields to cross sections, using the formula of Merzbacher and Lewis (1958). Using the target-detector arrangement in Fig. 11(a), the cross section is given by

$$\frac{d^2\sigma}{dE_x d\Omega} = \frac{1}{n_2}\left[\frac{d}{dE}\left[\frac{d^2Y}{dE_x d\Omega}\right]\frac{dE}{dx} + \mu(E_x)\frac{d^2Y}{dE_x d\Omega}\right], \tag{4.4}$$

where dE/dx is the ion stopping power (Northcliffe and Schilling, 1970) and μ is the absorption cross section for x rays of energy E_x in the target material (McMaster *et al.*, 1969). For two-collision MO x rays one can also compare thick-target yields directly with experiment. One can substitute the thick-target projectile x-ray yield into Eqs. (3.6) or (3.48) in place of the projectile x-ray cross section, since most other factors in those equations are approximately independent of the ion velocity. If normalization to measured x-ray cross sections is not done (e.g., for one-collision MO x rays), the theoretical thick-target yield must be calculated from the expression

$$\frac{d^2Y}{dE_x d\Omega} = \int_E^0 dE' \frac{dx}{dE}\frac{d^2\sigma(E')}{dE_x d\Omega}\exp[-\mu x(E-E')], \tag{4.5}$$

where $x(E-E')$ is the distance the ion travels in the target while losing an energy $E-E'$.

To analyze two-collision MO x-ray cross sections, it is desirable to measure simultaneously MO x rays, projectile SA K x rays, and spectroscopic features of the projectile K x-ray spectra (Kaufmann *et al.*, 1973). Line shapes taken with bent-crystal spectrometers, line shifts (Greenberg *et al.*, 1977), or $K\alpha$ to $K\beta$ intensity ratios give information about the L and M shell populations which affect the projectile K x-ray decay rates in Eq. (3.48) and the occupation of the molecular energy levels during the collision (Anholt, 1978a). In practice this is done so rarely that theory is handicapped in explaining many MO x-ray results in detail.

B. Other radiative processes

1. Overview

Since the MO x-ray spectrum is a continuum spectrum, it is important to determine the magnitude of other radiative processes giving continuum spectra. These emissions fall into three classes: bremsstrahlung background, γ-ray background, and background from other atomic processes.

In a many-body collision like that of a heavy ion with a heavy atom, several possible bremsstrahlung processes can occur. Nucleus-nucleus bremsstrahlung (NNB) can be produced in the collision between the projectile and target nuclei. Target-atom electrons colliding with the projectile nucleus can produce electron-nucleus bremsstrahlung called primary bremsstrahlung (PB; Schnopper *et al.*, 1974), which is also called "radiative ionization" (Jakubassa and Kleber, 1975; Anholt and Saylor, 1976) or "quasifree bremsstrahlung" (Chu *et al.*, 1981; Yamadera *et al.*, 1981). The collision of the projectile electrons with the target nucleus can likewise make electron-target-nucleus bremsstrahlung, and the collision of ionized electrons with other target nuclei in solid targets can make secondary-electron bremsstrahlung (SEB). Binary collisions between the bound projectile and target electrons themselves do not produce bremsstrahlung directly, but the dynamic polarization of the atomic clouds by an incoming particle can induce a dipole, producing atomic bremsstrahlung (Amusia, 1982; Ishii and Morita, 1984) or quasimolecular bremsstrahlung (Anholt and Salin, 1977), depending on the applicable collision model.

The excitation of γ rays by nuclear reactions or Coulomb excitation (Alder *et al.*, 1956) can produce sharp, low-energy γ-ray lines in MO x-ray spectra. Often, high-energy γ rays are produced which Compton scatter in the thin x-ray detectors, leaving a flat continuous photon distribution. Quasimolecular x-ray emission is usually studied at projectile energies where nuclear reactions are not allowed classically, but beam-induced γ-ray background from Coulomb excitation and room background are usually present.

Most atomic collisions give sharp SA x-ray lines,

which, although inhibiting the observation of MO x-ray continua in some parts of the spectrum, allow MO x-ray observation in most regions of interest. However, radiative electron capture (REC) can produce a broad peak which tails into the MO x-ray region (Betz *et al.*, 1975).

2. Nucleus-nucleus bremsstrahlung

In a small-impact-parameter heavy-ion–atom collision, the projectile-target-nucleus electric dipole is accelerated, causing the emission of radiation. Classically, the energy $E(\omega)$ radiated into a solid angle $d\Omega$ is obtained by Fourier-transforming the dipole velocity $\mathbf{V}_\nu(t)$ (Reinhardt *et al.*, 1976)

$$\frac{d^2E(\omega)}{d\omega\, d\Omega}=\frac{\omega^2}{4\pi^2c^3}\left|\int_{-\infty}^{\infty}dt\, e^{i\omega t}\sum_\nu q_\nu e^{-i\mathbf{k}\cdot\mathbf{R}_\nu(t)}\mathbf{V}_\nu(t)\times\hat{\mathbf{k}}\right|^2, \tag{4.6}$$

where $\mathbf{k}$ is the photon momentum, and the sum ν is over the projectile and target nuclear charges q_ν. Expanding the factor $\exp(-i\mathbf{k}\cdot\mathbf{R}_\nu)=1-i\mathbf{k}\cdot\mathbf{R}_\nu+\cdots$, one obtains

$$\frac{d^2E(\omega)}{d\omega\, d\Omega}=\frac{\omega^2}{4\pi^2c^3}\left|\dot{\mathbf{d}}(\omega)\times\hat{\mathbf{k}}-\frac{i}{2}\dot{\mathbf{Q}}(\omega)\times\mathbf{k}+\cdots\right|^2, \tag{4.7}$$

where $\dot{\mathbf{d}}(\omega)$ is the Fourier transform of the electric dipole velocity, and $\dot{\mathbf{Q}}(\omega)$ is that of the quadrupole velocity.

Retention at the quadrupole term is important. While the dipole radiation varies as the difference between the projectile and target charge-to-mass ratios,

$$\frac{d^2\sigma_{\rm dip}}{d\omega\, d\Omega}\sim\left[\frac{Z_1}{A_1}-\frac{Z_2}{A_2}\right]^2, \tag{4.8}$$

the quadrupole intensity varies as the sum

$$\frac{d^2\sigma_{\rm quad}}{d\omega\, d\Omega}\sim\left[\frac{Z_1}{A_1^2}+\frac{Z_2}{A_2^2}\right]^2 \tag{4.9}$$

(Jakubassa and Kleber, 1975; Reinhardt *et al.*, 1976). In an ion-atom collision where $Z_1/A_1\approx Z_2/A_2\approx\frac{1}{2}$, the dipole intensity is suppressed relative to the quadrupole intensity, making up for the fact that the quadrupole intensity is normally smaller by a factor of α^2.

Dipole NNB has been calculated by Alder *et al.* (1956), and dipole and quadrupole NNB have been calculated by Malkov and Shmushkevich (1961), Jakubassa and Kleber (1975), and Reinhardt *et al.* (1976). Figure 13 compares measurements of NNB in asymmetric 13-MeV $^{18}O+{}^{58}Ni$ collisions (Trautvetter *et al.*, 1976) with calculations by Reinhardt *et al.* (1976). In these very asymmetric collisions, MO x-ray emission is nearly absent. Equation (4.7) indicates that, for a given photon direction, the dipole and quadrupole terms interfere, so that the total x-ray emission probability is not just the sum of dipole and quadrupole intensities. Vincent (1977) has measured

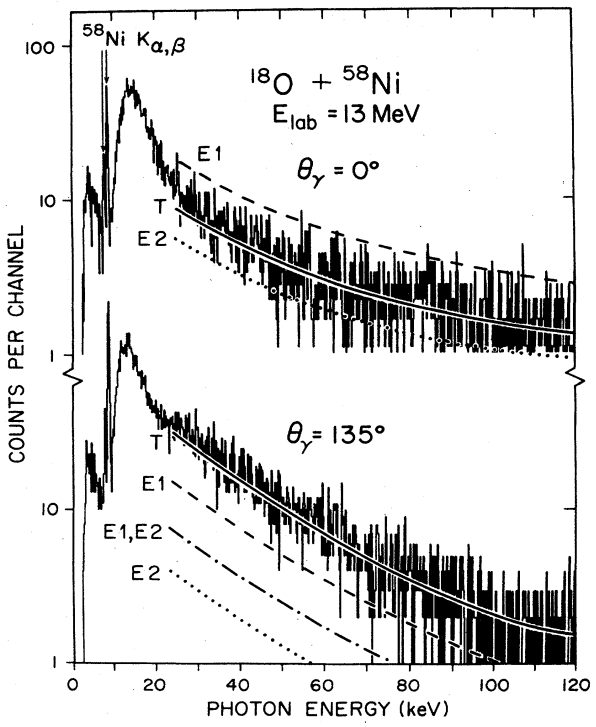

FIG. 13. Nucleus-nucleus bremsstrahlung spectra seen in 13-MeV $^{18}O+{}^{58}Ni$ collisions at detector angles of 0° and 135°. Contributions from dipole NNB ($E1$), quadrupole NNB ($E2$), and the total (T) coherent sum of $E1$ and $E2$ contributions are shown. $E1,E2$ denote the component due to dipole-quadrupole interference (Trautvetter *et al.*, 1976).

NNB in many other heavy-ion–atom collisions, finding generally good agreement with the calculations of Reinhardt *et al.* (1976).

3. Secondary-electron bremsstrahlung

Classically, a projectile with velocity v can undergo binary collisions with loosely bound target electrons, producing ionized electrons with energies up to

$$T_{\rm max}\approx 2mv^2 \tag{4.10}$$

(Merzbacher and Lewis, 1958). These electrons can collide with other target atoms in solid targets (or with atoms composing the experimental chamber walls), and can emit bremsstrahlung radiation up to the energy $T_{\rm max}$. Also, inner-shell ionization can produce ionized electrons with energies in excess of $T_{\rm max}$, although the differential ionization cross section $d\sigma_{\rm ioniz}/d\Omega_e dE_e$ drops off rapidly for electron kinetic or photon energies much above $T_{\rm max}$, and therefore the SEB cross section drops off rapidly for x-ray energies above $T_{\rm max}$.

For targets that are thick with respect to the range of the ionized electrons, the SEB cross section is given by

$$\frac{d^2\sigma_{\rm SEB}(\omega,\theta)}{d\Omega_{\rm lab}d\omega}=\int_\omega^\infty dE_e\int d\Omega_e\frac{d\sigma_{\rm ioniz}}{d\Omega_e dE_e}\int_\omega^{E_e}\frac{dE_e'}{S(E_e')}n_2\frac{d^2\sigma_{\rm brem}(Z_T,E_e',\omega,\theta_{br})}{d\Omega_{br}d\omega}, \tag{4.11}$$

where $S(E_e')$ is the electron stopping power in the target material of density n_2, $d^2\sigma_{\rm brem}/d\Omega_{br}d\omega$ is the bremsstrahlung emission cross section, θ_e and φ_e are the electron emission angles, $\theta_{\rm lab}$ is the photon emission angle with respect to the beam axis, and θ_{br} is given by

$$\cos\theta_{br}=\cos\theta_e\cos\theta_{\rm lab}+\sin\theta_e\sin\theta_{\rm lab}\cos\varphi_e \ . \quad (4.12)$$

Formulas for targets that are thin with respect to the electron range but thick with respect to the ion range (thick-target SEB yields) have also been derived (Ishii *et al.*, 1976,1977).

Several calculations of SEB have been made, which differ with respect to the bremsstrahlung and ionization cross sections used. For a review of the relative merits of bremsstrahlung cross-section formulas, we refer the reader to articles by Lee *et al.* (1976) and Tseng *et al.* (1979) and to data tables for electron bremsstrahlung cross sections (Pratt *et al.*, 1977; Kissel *et al.*, 1983). The least well understood factor is the ionization cross section. For high-velocity projectiles where $E_x < T_{\rm max}$, and for loosely bound target electrons with $T_{\rm max} \gg U_e$ (the average target electron binding energy), one can use the classical Rutherford formula (Yamadera *et al.*, 1981; Chu *et al.*, 1981),

$$\frac{d\sigma_{\rm ioniz}}{d\Omega_e dE_e}=\frac{(Z_p e^2)^2}{mv^2}\frac{1}{E_e^2}\delta[\cos\theta_e-(E_e/T_{\rm max})^{1/2}] \ . \quad (4.13)$$

Calculations using this equation and the Bethe-Heitler formula for bremsstrahlung are shown in Fig. 14 for 20-MeV $p+$Be collisions (Chu *et al.*, 1981). For x-ray energies smaller than $T_{\rm max}$ ($\approx$40 keV in these collisions), good agreement with the measurement is obtained. For x-ray energies slightly larger than $T_{\rm max}$, one can [unlike in Eq. (4.13)] incorporate the initial Fermi motion of the electron, using the impulse approximation for the ionization cross section (Jakubassa and Kleber, 1975). For x-ray energies much in excess of $T_{\rm max}$, however, plane-wave Born and binary-encounter-approximation calculations of the ionization cross sections have been used (Folkmann *et al.*, 1974; Jakubassa and Kleber, 1975; Ishii *et al.*, 1976,1977). The binary-encounter approximation (Bonsen and Vriens, 1970) provides a simpler formula for the excitation of electrons from the outer atomic shells.

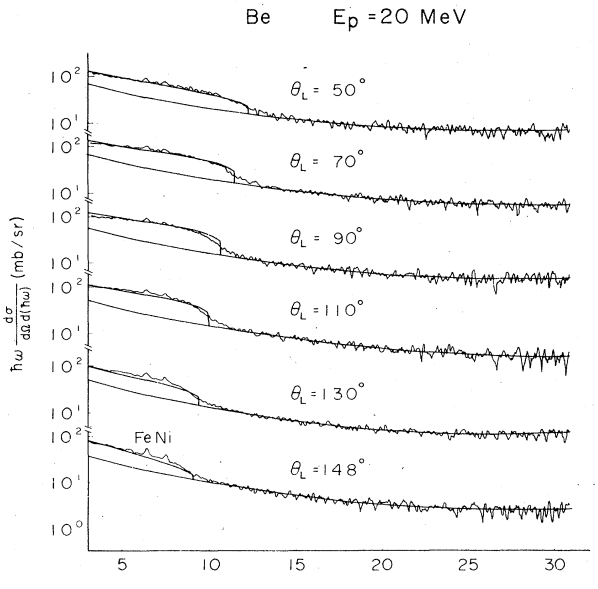

FIG. 14. Continuum x-ray spectra seen in 20-MeV $H^+ + Be$ collisions for detector angles between 50° and 148°. The ordinate shows the cross section multiplied by the x-ray energy. The smooth curves in the region between 3 and 30 keV show the calculated secondary-electron bremsstrahlung yield. The other curves extending to between 8 and 12 keV show the calculated primary bremsstrahlung yield (Chu *et al.*, 1981).

Most SEB studies have been made in collisions with protons and He, where the atomic model of inner-shell ionization is applicable. For slow heavy-ion—atom collisions where MO's are formed, the atomic electron-ionization cross sections cannot be used for the inner-shell electrons. The condition for the formation of MO's, $v_1/v_K \ll 1$, requires the use of low velocities, giving values of $T_{\rm max}$ smaller than many MO x-ray energies of interest. The most tightly bound electrons are generally excited to the largest kinetic energies E_e, so the main SEB background (at least near the K MO x-ray spectrum) is expected to come from $1s\sigma$, $2p\sigma$, $2s\sigma$, and $2p\pi$ electron ionization, for which detailed ionization theories are lacking. A few measurements have been made of ionized electron distributions in slow ion-atom collisions, from which SEB intensities can be calculated. Bell, Trollmann, Betz, and Spindler (1982) found that the SEB intensity is a factor of 0.01—0.02 smaller than the measured continuum intensity in 64-MeV Ni + Ni collisions. They also developed a scaling law for secondary-electron production cross sections from which other SEB intensities can be calculated (Bell, Trollmann, and Betz, 1982).

4. Primary bremsstrahlung

A projectile colliding with a target atom sees a number of target electrons speeding toward it with an energy $T=\frac{1}{2}mv^2$. Bremsstrahlung radiation can be emitted in projectile—nucleus—target-electron collisions with energies $E_x \le T$ in the projectile frame. In transforming from the projectile frame to the lab frame, the maximum energy becomes

$$E_{x\max}=(1-\beta^2)^{1/2}T(1-\beta\cos\theta_{\rm lab})^{-1} \ , \quad (4.14)$$

where $\beta=v/c$. For 20-MeV $p+$Be collisions where $T\approx 10$ keV, the laboratory end point of the PB spectrum varies from $\sim$8 keV at $\theta_{\rm lab}=148°$ to $\sim$12 keV at $\theta_{\rm lab}=50°$, as shown in Fig. 14 (Chu *et al.*, 1981).

The PB cross section for $E_x < T$ is just the projectile nucleus-electron bremsstrahlung cross section Lorentz transformed into the laboratory (Chu *et al.*, 1981)

$$\frac{d^2\sigma_{\rm PB}}{d\Omega_{\rm lab}d\omega_{\rm lab}}=Z_T\frac{d^2\sigma_{\rm brem}(Z_p,\theta_c,\omega_c)}{d\Omega_c d\omega_c}\frac{d\omega_c}{d\omega_{\rm lab}}\frac{d\Omega_c}{d\Omega_{\rm lab}} \ , \quad (4.15)$$

where the center-of-mass angle θ_c is related to $\theta_{\rm lab}$ by

$$\cos\theta_c = \frac{\beta - \cos\theta_{\rm lab}}{1 - \beta\cos_{\rm lab}} , \tag{4.16}$$

and the factor Z_T is the number of target electrons per atom striking the projectile nucleus. Calculations of the PB cross section using the Bethe-Heitler formula with the Elwert correction factor (Lee *et al.*, 1976) for bremsstrahlung in 20-MeV p+Be collisions are in good agreement with experiment for $E_x < E_{x\max}$ (Fig. 14; Chu *et al.*, 1981).

Near the end point of the PB spectrum, one can use the impulse approximation (Jakubassa and Kleber, 1975) to account for the Fermi motion of the target electrons. This allows x rays with energies exceeding $E_{x\max}$ to be emitted. For $E_x \gg E_{x\max}$, Anholt and Saylor (1976) calculated PB using formulas based on the binary-encounter approximation.

In heavy-ion—atom collisions where MO x rays are seen, the inner-shell electrons forming MO's are not free to undergo quasifree radiative collisions with the target or projectile nuclei. The free outer-shell target electrons can contribute to PB, but the condition for formation of MO's, $v \ll v_K$, confines the PB spectrum to small x-ray energies. For example, in 75-MeV Nb + Nb collisions (Fig. 12), $E_{x\max}$ is less than 0.5 keV, but the MO x rays range from 20 to 80 keV. Projectile electrons could undergo collisions with target nuclei, producing bremsstrahlung x rays with energies up to $E_x = \frac{1}{2}mv^2$ (their is no Doppler transformation in this case). Such electrons would have to be nearly free, however. Electrons with velocities larger than the ion velocity forming MO's would avoid radiative collisions with the target nuclei. The Bohr (1948) charge-state theory assumes that these electrons will be absent in thick solid targets, leaving no free electrons to collide with target nuclei.

In the slow collisions of interest, electron bremsstrahlung can be emitted also during the ionization of electrons from inner-shell MO's. Independent of the ionization mechanism, the electron is accelerated during the ionization process, allowing for the simultaneous emission of bremsstrahlung. A consistent molecular calculation of this process has not been developed.

Quasimolecular bremsstrahlung is also possible (Anholt and Salin, 1977). NNB considers the acceleration of the electric dipole between the projectile and target nuclei during a collision. Asymmetric molecules have a nonzero electric dipole given by

$$\mathbf{d}_{\rm MO}(R) = \sum_{i=1}^{N} \langle \chi_i(\mathbf{r},\mathbf{R}) \,|\, \mathbf{r} \,|\, \chi_i(\mathbf{r},\mathbf{R}) \rangle , \tag{4.17}$$

where N is the number of electrons participating in MO formation. This dipole varies nonlinearly with R, and hence is accelerated during a collision. Only low-energy photons are emitted, however, making this emission a relatively unimportant process.

5. γ-ray background

Although MO x-ray measurements are generally done with beam energies insufficient to overcome the nuclear Coulomb barrier and to make nuclear reactions, γ rays are nevertheless created in sub-barrier reactions or by nuclear Coulomb excitation, which can produce sharp γ-ray lines, but more often give a flat continuous photon distribution in the thin x-ray detectors, as the result of Compton scattering. Also, because of radioactive potassium and thorium in the environment, γ-ray room background is always present. The latter is the easiest background to remove, by counting photons after the accelerator has been shut off and subtracting the resulting real-time normalized spectrum from the MO x-ray measurements.

The beam-induced background (BIB) can be removed only by consistently accounting for known contributions of NNB and BIB in the high-energy portions of the spectra. Figure 12 illustrates how this is done in 75-MeV Nb + Nb collisions (Vincent, 1977). A thin Nb target on a thick C backing was used in this experiment. NNB calculated for Nb + Nb collisions, room background, and NNB + BIB measured in equal-energy Nb + C collisions are shown. The magnitude of the BIB from the Nb + Nb collisions, which was found in separate measurements to be approximately independent of x-ray energy to very high photon energies, was fitted by requiring that the calculated total x-ray intensity far above the MO x-ray spectrum agree with experiment. In low-Z_u collisions, where the MO x rays are relatively much more intense, γ-ray background and NNB are generally negligible.

6. Radiative electron capture

A projectile with an inner-shell vacancy can, in addition to undergoing a second collision in which two-collision MO x rays are emitted, radiatively capture target outer-shell electrons, giving a photon whose peak energy in the projectile frame is given by

$$E_{\rm REC} \approx U_K(p) + \tfrac{1}{2}mv^2 , \tag{4.18}$$

for capture into the K shell of the projectile with binding energy $U_K(p)$. REC and MO x-ray emission are related in that inner-shell electrons are "radiatively captured" by MO x-ray emission, and outer-shell target electrons by REC emission.

REC x-ray emission has the following characteristics. (1) The x-ray energy in the laboratory is Doppler shifted as a result of the Lorentz transform of the energy given in Eq. (4.18) into the laboratory; higher-energy x rays are emitted at forward angles, lower-energy ones at backward angles. (2) The angular distribution of REC radiation varies nearly as $\sin^2\theta_{\rm lab}$, as the result of a cancellation of the electron retardation effect, which by itself would give a photon distribution peaked in the backward direction in the laboratory, and the Lorentz transform which shifts the angular distribution forward in the laboratory (Spindler *et al.*, 1979). (3) The REC emission cross sec-

tion depends, like the $1s\sigma$ two-collision MO x-ray cross section, on the number of equilibrium projectile K vacancies in the solid target. For this reason, REC is most readily seen in high-velocity collisions where the projectile is fully stripped (Kienle *et al.*, 1973; Schnopper *et al.*, 1974; Bell *et al.*, 1975). (4) The REC x-ray peak has a large width as a result of the Fermi motion of the target electrons. This width is given approximately by

$$\Delta E_x \approx v p_z \ , \tag{4.19}$$

where p_z is the average momentum of the target electrons, related to the width of the Compton profile (Kleber and Jakubassa, 1975). It is this width which can make REC emission a troublesome background beneath the MO x-ray continuum. For instance, in the relatively high-energy 90-MeV S + Al collisions (Fig. 15), REC emission greatly obscures the MO x-ray continuum up to the UA energy E_u. At lower projectile velocities (16-MeV S + Al), it is less of a problem, but in 16-MeV S + C collisions, where E_u is smaller, it also obscures most of the MO x-ray spectrum. The shape of the REC emission can be accurately calculated with the impulse approximation (Kleber and Jakubassa, 1975; Spindler *et al.*, 1977). The intensity can be normalized, like the two-collision MO x-ray intensity, to the projectile x-ray cross section in high-Z_u collisions (where the radiative decay rate exceeds the collisional quenching rate significantly), and can be normalized to the REC peak intensity in low-Z_u collisions.

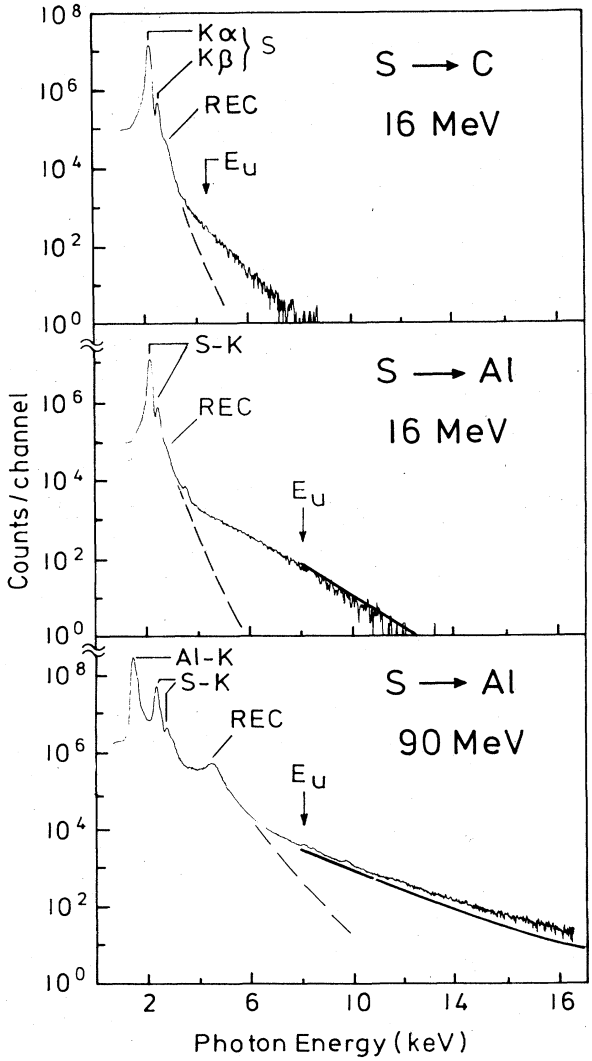

FIG. 15. X-ray spectra induced by sulfur ions impinging on 100-μg/cm^2 C and Al targets, corrected for x-ray attenuation in the absorber between the detector and target (Betz *et al.*, 1975). The width of one channel is 18.2 eV. The dashed lines show the calculated REC tail (Kleber and Jakubassa, 1975). The spectrum extending beyond the REC line and beyond the position of the UA x-ray lines E_u is due to $1s\sigma$ MO x-ray production.

C. $1s\sigma$ molecular-orbital x rays

1. Two-collision MO x-ray production

Figures 16 and 17 compare relative intensities from various MO x-ray transitions in 5-MeV Ni + Ni collisions (calculated using the quasistatic approximation; Meyerhof and Anholt, 1979) and 37-MeV Ni + Ni collisions (calculated using the full electron-slip theory; Anholt, 1978a).

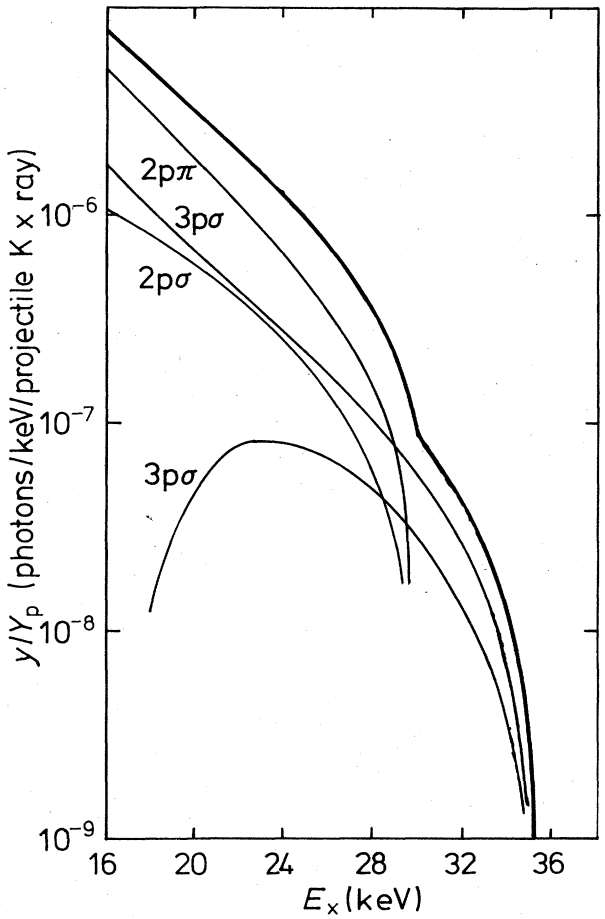

FIG. 16. Scaled MO x-ray yields in 5-MeV Ni + Ni collisions, calculated using the quasistatic approximation for the various component transitions (Meyerhof and Anholt, 1979).

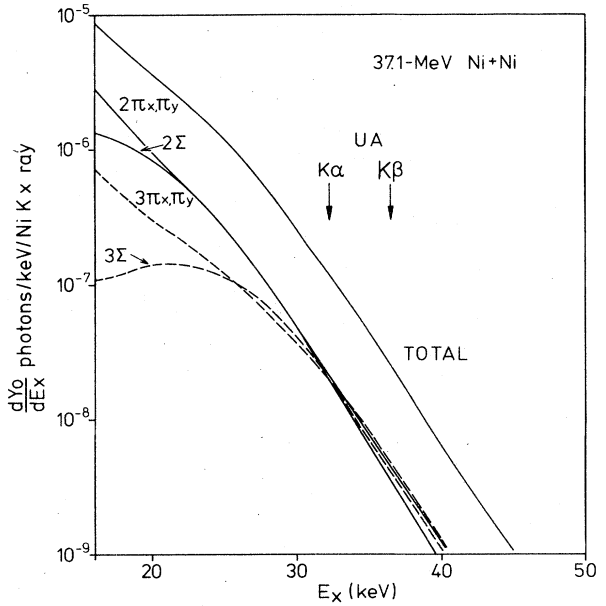

FIG. 17. Absolute MO x-ray intensities in 37-MeV Ni + Ni collisions, calculated including Coriolis coupling between the $2p\sigma$ and $2p\pi$ and the $3p\sigma$ and $3p\pi$ MO's. From Anholt (1978a).

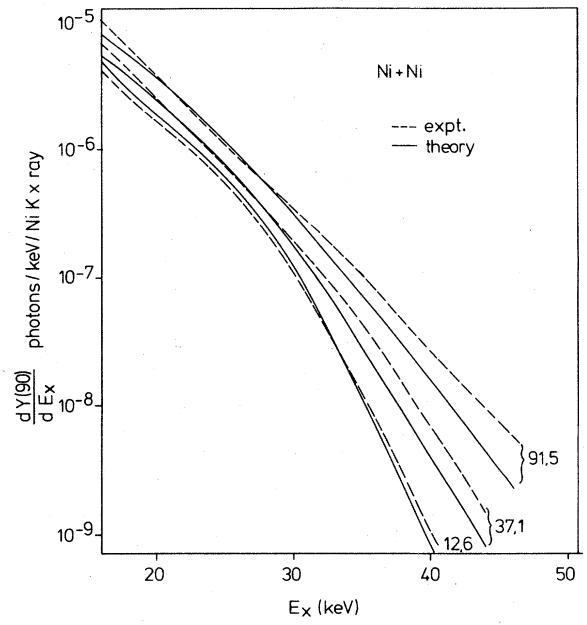

FIG. 18. Experimental and calculated MO x-ray intensities for 12.6-, 37.1-, and 91.5-MeV Ni+Ni collisions, observed at 90° to the beam direction. The theoretical intensities (solid lines) were calculated using the same electron occupation numbers needed to explain the measured MO x-ray anisotropies. The experimental values were measured by Vincent (1977).

In the quasistatic model, the $K\alpha$ MO x-ray spectrum ($2p\sigma,\pi\rightarrow 1s\sigma$ transitions) ends near the UA $K\alpha$ energy, and the $K\beta$ MO x-ray spectrum ($3p\sigma,\pi\rightarrow 1s\sigma$ transitions) near the UA $K\beta$ energy. In the dynamic calculations, the spectra fall off exponentially beyond the UA transition energies. Because the MO $K\beta$ x-ray spectra are shifted ~ 6 keV higher than the $K\alpha$ spectra, the MO $K\alpha$ and $K\beta$ intensities are all nearly equal (per electron) beyond the UA $K\alpha$ transition energy, despite the fact that the $K\beta$ transition rate $\lambda_{if}(R=0)$ is approximately 0.2 times smaller than the $K\alpha$ rate. The neglect of $K\beta$ transitions on the basis of relative transition rates alone is not justified. Note, however, that we do neglect $4p\sigma,\pi\rightarrow 1s\sigma$ transitions, whose relatively larger end-point energy does not make up for their smaller transition rates compared to the $3p\sigma,\pi\rightarrow 1s\sigma$ rates. Because the σ and π MO's are coupled in the electron-slip calculations, the relative contributions from such transitions as $2\Sigma\rightarrow 1s\sigma$ and $2\Pi\rightarrow 1s\sigma$, compared to $2p\sigma\rightarrow 1s\sigma$ and $2p\pi\rightarrow 1s\sigma$ in the quasistatic calculations, are qualitatively different. Note, however, that the $2p\pi\rightarrow 1s\sigma$ intensity in Fig. 16 includes both the π_x and π_y MO's, and therefore is about twice as large as the individual $2\Pi_x$ and $2\Pi_y$ intensities shown in Fig. 17. Although the $3p\sigma\rightarrow 1s\sigma$ intensity is reduced at small x-ray energies due to the node in the transition rate at intermediate internuclear distances (Fig. 9), in the electron-slip calculations the analogous $3\Sigma\rightarrow 1s\sigma$ x rays include contributions from the $3p\pi\rightarrow 1s\sigma$ transitions, and therefore the 3Σ intensity does not decrease as much at small x-ray energies.

Figure 18 compares calculated MO x-ray thin-target yields in 12.6-, 37.1-, and 91.5-MeV Ni + Ni collisions with measurements by Vincent and Greenberg (Vincent, 1977). The yield defined here is the number of x rays per 4π sr seen at 90° to the beam direction per Ni K x ray, which is the doubly differential cross section in Eq. (3.48) divided by $2\sigma_{px}$, since the target and projectile K x-ray cross sections are nearly equal (Vincent, 1977). The yield increases with projectile energy due to the decrease in the factor λ_x in Eq. (3.48). From SA K x-ray line shifts, Greenberg *et al.* (1977) determined the average number of projectile L vacancies V_L: 1.32 for 12.6-MeV to 3.6 for 91.5-MeV Ni + Ni collisions. Assuming these are all $2p$ vacancies, λ_x is given by

$$\lambda_x \sim \frac{6-V_L}{6}\lambda_x^{\mathrm{sv}}, \tag{4.20}$$

where λ_x^{sv} is the single vacancy $K\alpha$ transition rate (Scofield, 1969). Since λ_x decreases at large projectile energies, the expected yield increases, in good agreement with experiment. These vacancies also affect the occupancy of the MO's, and therefore the MO transition rates λ_{if}, but since the target atom always has a full number of electrons to partially fill the MO's, $\lambda_{if}(R)$ is not reduced as much as λ_x. The occupancy of the various MO's strongly affects the MO x-ray angular anisotropy, as discussed in Sec. V.B. The calculated intensities have been multiplied by a factor of 0.65 to bring them into agreement with experiment in the middle part of the spectra. This is probably due to the inaccuracy of the calculated molecular energy levels. Hydrogenic MO transition energies were semiempirically adjusted for electron screening and rela-

tivistic effects, using atomic binding energies in these calculations. This may not be adequate, however. Given the exponential falloff of the calculated MO x-ray spectrum, the factor of 0.65 difference in intensity can be interpreted as a <2 keV discrepancy in the x-ray transition energies. In addition, the calculated intensities are lower than experiment in the high-E_x portions of the spectra as discussed in Sec. IV.C.4.

2. A scaling law for MO x-ray production

To facilitate comparison between calculated MO x-ray intensities and experiment, Anholt (1978b) derived a scaling law relating the MO x-ray intensity at a frequency ω to a function F of three variables: $v=\omega/\omega_0$, $\zeta=Z_H/Z_L$, and $q=\omega_0 a_{KL}/v$, where ω_0 is the UA $K\alpha$ transition frequency, $a_{KL}=a_0/Z_L$ is the K radius of the lighter collision partner, a_0 is the Bohr radius, and the collision asymmetry parameter ζ is the ratio of higher to lower atomic numbers. Below the position of the UA K x-ray lines ($0.5<v<1$), the MO x-ray spectra all have similar shapes independent of ζ and q. Figure 19 compares measured MO x-ray spectra (at 90° to the beam direction) seen in a number of collisions for various values of ζ and q, where the thick-target yield spectra were normalized at $v=0.7$. The spectra all have approximately identical slopes, though the higher-ζ spectra increase at low-v values faster than the lower-ζ spectra, mainly because of the different relative position of the higher-Z SA $K\beta$ x rays. The quasistatic approximation predicts nearly identical shapes for different ζ and q values. The measured spectra are in good agreement with the quasistatic approximation for $v<0.8$. For $v>1$, the dynamic theory predicts a strong q or velocity dependence, discussed in Sec. IV.C.4. In the data shown in Fig. 19, the q dependence is not obvious.

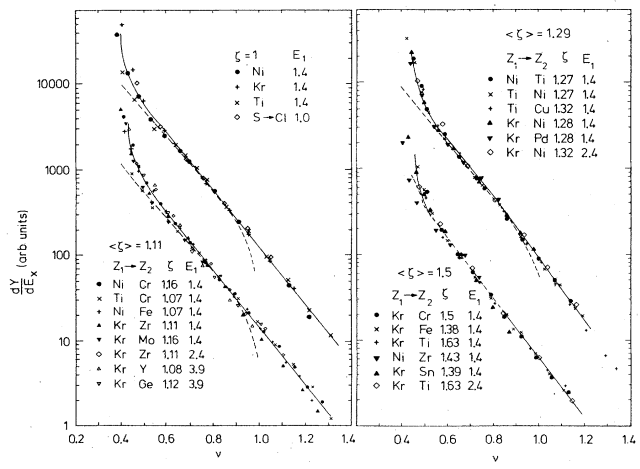

FIG. 19. Absolute thick-target yields plotted against the reduced x-ray energy v (see text) and normalized at $v=0.7$ for a variety of projectiles (Z_1), targets (Z_2), and projectile energies E (in MeV/amu). The dashed line shows quasistatic calculations. The solid line is drawn to guide the eye.

To assess measured MO x-ray yields, one can compare the shape with the curves in Fig. 19, and can compare the measured intensity with theory at a single v value, $v=0.7$ being chosen as the point most independent of ζ and q. Using tabulated functions of the spectral shape function $F_{\rm tot}(v=0.7,\zeta)$ (Anholt, 1978b), the two-collision MO x-ray thick-target yield at 90° to the beam direction $[d^2Y(90°)/dE_x d\Omega$ in b per 4π sr$=dY/dE_x]$ is given by

$$\frac{dY}{dE_x}=Y_{px}W\frac{n_2 a_{KL}^3\lambda_{\rm UA}}{\hbar\omega_0\lambda_x}F_{\rm tot}\ , \tag{4.21}$$

where $\lambda_{\rm UA}$ and λ_x are UA and SA projectile K x-ray decay rates (Scofield, 1969), and the other quantities are defined in Eq. (3.48) and above. A similar equation for MO x-ray cross sections in terms of projectile x-ray cross sections σ_{px} instead of the projectile thick-target x-ray yields can be obtained (the velocity dependence of W being neglected). Figures 20 and 21 compare thick-target yields seen in Ti, Ni, and Kr collisions with measurements by Anholt (1978b). The two-collision MO x-ray yield is largest in near-symmetric collisions. Most projectile vacancies are made in the $2p\sigma$ MO during a collision (Fig. 3), and independent of whether the projectile is the lighter or heavier collision partner, the probability of transferring a vacancy from the $2p\sigma$ MO to the projectile, then into the $1s\sigma$ MO in a second collision, is given by $w(1-w)$, where w is defined in Eq. (3.7). This quantity has the largest value, $\frac{1}{4}$, in symmetric collisions and falls off rapidly

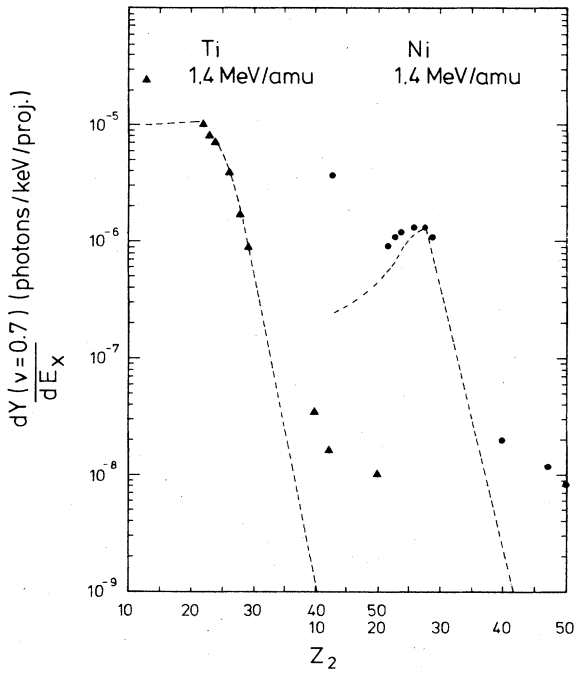

FIG. 20. Absolute thick-target yields of continuum x rays at $v=0.7$ for 1.4-MeV/amu Ti and Ni collisions vs target atomic number Z_2. The dashed lines show scaling-law calculations for two-collision $1s\sigma$ MO x rays, multiplied by factors of 1.5 (Ti) and 2.1 (Ni). These factors are probably due to the reduction of λ_x [Eq. (4.20)] from the single-vacancy value, due to projectile stripping (Anholt, 1978b).

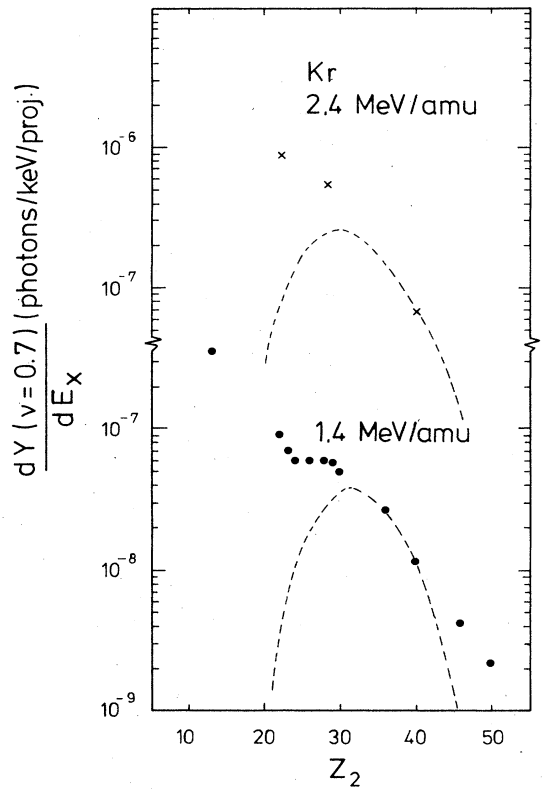

FIG. 21. Absolute thick-target yields of MO x rays at $v=0.7$ for 1.4- and 2.4-MeV/amu Kr collisions, as in Fig. 20. The dashed lines show scaling-law calculations for two-collision $1s\sigma$ MO x rays, multiplied by factors of 1.1 (1.4-MeV/amu Kr) and 1.75 (2.4-MeV/amu Kr).

with lower or higher Z_2. The other factor depending strongly on Z_2 is the target-atom density n_2 (in atoms per cm^3). In Kr collisions, the yield is not peaked at $Z_2=Z_1=36$, but is peaked at lower Z_2 values, where higher atomic densities are found. Meyerhof *et al.* (1974) made a series of measurements of MO x rays in 30-MeV Br + Br collisions where the density n_2 was varied by using Br_2, KBr, and KBr targets diluted with KCl. The K and Cl atoms produce few MO x rays in the region of interest. The MO x-ray yield was found to vary linearly with the density of Br atoms, as expected for two-collision MO x rays.

3. One-collision MO x-ray production

In the asymmetric collisions shown in Figs. 20 and 21, MO x rays are seen that, while having the same shape dependence on v as two-collision MO x rays, do not agree with the calculated two-collision MO x-ray intensities. These x rays are probably one-collision $1s\sigma$ MO x rays, which are dominant in asymmetric collisions, in collisions with gas targets where n_2 is small, and in high-Z_u collisions. (The data for asymmetric collisions with Ni ions in Fig. 20 have also been interpreted as atomic bremsstrahlung by Ishii and Morita, 1984.)

A number of comparisons of gas-target and solid-target MO x-ray intensities have been made (Bell *et al.*, 1975; Laubert *et al.*, 1976; Schmidt-Böcking *et al.*, 1978a,1978b; Stoller *et al.*, 1981). Higher yields in solid targets, but similar MO x-ray spectral shapes in gas and solid targets are observed (Fig. 22). Both one- and two-collision MO x-ray production are possible in solid targets. Comparison of absolute gas- and solid-target intensities is complicated because of possible MO x-ray production charge-state dependences. Schmidt-Böcking *et al.* (1978a) have shown that K MO x-ray cross sections in 32-MeV S + Ar(gas) collisions depend strongly on the projectile charge state. With larger projectile charge states, $1s\sigma$ electrons can be excited into empty nearby bound states, thus increasing the $1s\sigma$-vacancy production amplitude and the one-collision MO x-ray yield. Comparisons are best done between projectiles of the same charge state in solid targets and gas targets (Stoller *et al.*, 1981).

Aside from one model calculation for $H^+ + H$ collisions by Thorson and Choi (1977), one-collision $1s\sigma$ MO x-ray intensities have not been calculated for low-Z_u collisions, because a detailed knowledge of $1s\sigma$-vacancy pro-

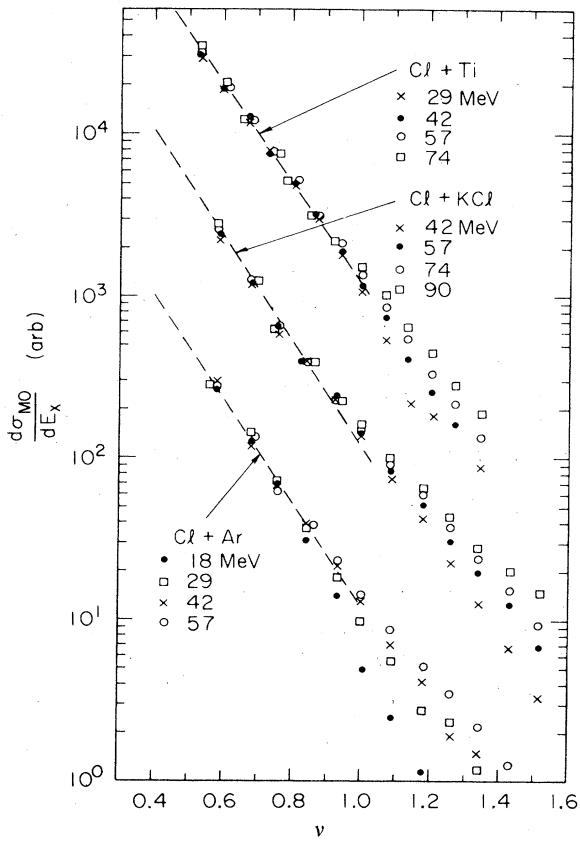

FIG. 22. MO x-ray cross sections vs reduced x-ray energy v, normalized at $v=0.7$. Dashed line: empirical curve from other MO x-ray data (Anholt, 1978b, Fig. 19). These results show the similarity between continuum x rays measured using gas targets (Cl + Ar), where only one-collision MO x rays are present, and x rays measured in solid targets (Cl + KCl, Cl + Ti), where one- and two-collision MO x rays are present (Stoller *et al.*, 1981).

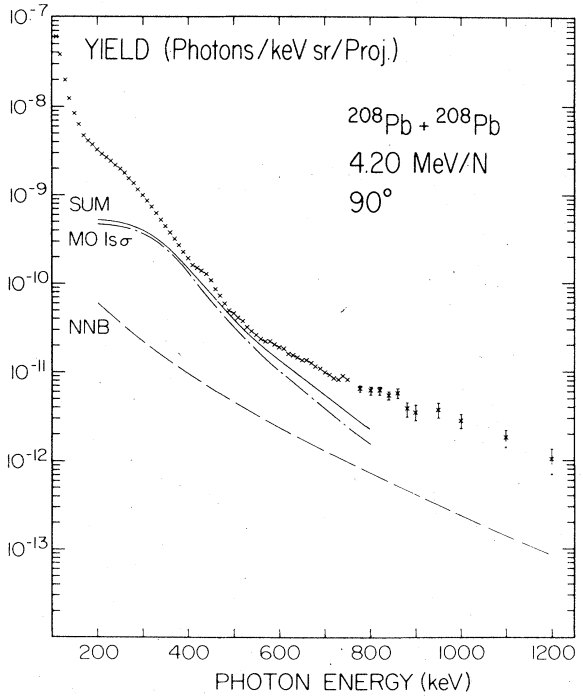

FIG. 23. Thick-target continuum x-ray yields measured in 4.2-MeV/amu ^{208}Pb+^{208}Pb collisions, using a highly enriched ^{208}Pb target (Stoller *et al.*, 1980). The theoretical curves are from calculations of NNB and one-collision $1s\sigma$ MO x rays by Kirsch *et al.* (1978).

duction is unavailable. The slopes of their calculated MO x-ray spectra scaled to collisions like Br + Br and Ni + Ni are flatter than those observed in experiments.

One-collision MO x-ray production has been calculated for very high-Z_u collisions (4.2-MeV/amu Pb + Pb collisions, Fig. 23) where $1s\sigma$-vacancy production is better understood (Müller *et al.*, 1978). One-collision MO x-ray production dominates in high-Z_u collisions, because the factors n_2 and a_{KL}^3 in the two-collision formula are relatively smaller, and the gap between the $1s\sigma$- and $2p\sigma$-vacancy production cross sections is smaller. For a given velocity, the $1s\sigma$ cross section increases faster with Z_u than the $2p\sigma$ cross section due to electronic relativistic effects (Behncke *et al.*, 1978; Anholt *et al.*, 1978), so to make MO x rays, it is simpler to excite the $1s\sigma$ vacancy in the same collision where it radiates than to create a $2p\sigma$ vacancy and transfer it into the $1s\sigma$ MO in a second collision. The calculations of Kirsch *et al.* (1978) for Pb + Pb collisions are in agreement with the measurements of Meyerhof *et al.* (1979) and Stoller *et al.* (1980), at x-ray energies just above 400 keV. However, the calculated spectrum is flatter than the measured one at lower x-ray energies. Contributions from MO x-ray transitions to $2p\sigma$ vacancies are present at low x-ray energies, as evidenced in measurements of the impact-parameter dependence of the continuum x-ray emission (Sec. VI.A). In any case, the spectrum between 200 and 400 keV disagrees with the one-collision $1s\sigma$ MO x-ray calculations, but agrees roughly at higher x-ray energies.

4. MO x-ray tails

One of the successes of the dynamic theory of MO x-ray emission (Sec. III.B) is the elucidation of the observed exponential spectral falloff beyond the MO x-ray end points expected in the quasistatic model. Expanding the transition energy difference $\omega_{fi}(t)$ as (Macek and Briggs, 1974)

$$\omega_{fi}(t)=\omega_{fi}^u+\dot{\omega}_{fi}t\ , \tag{4.22}$$

where ω_{fi}^u is the UA energy difference and $t=0$ is the point at which the two collision partners reach the distance of closest approach, we can calculate the MO x-ray emission probability in terms of Fresnel-integral functions $g(y)$ according to

$$\frac{dP_{\rm MO}}{d\omega}\sim\omega g^2(y)\approx\omega\exp(-4.22y)\ , \tag{4.23}$$

where $y=(\omega-\omega_{fi})(\pi\dot{\omega}_{fi})^{-1/2}$. Since the impact parameter does not appear in this equation, one obtains for the MO x-ray cross section

$$\frac{d\sigma_{\rm MO}}{d\omega}\sim\omega\exp\left[-\frac{0.693(\omega-\omega_{fi}^u)}{H}\right]\ , \tag{4.24}$$

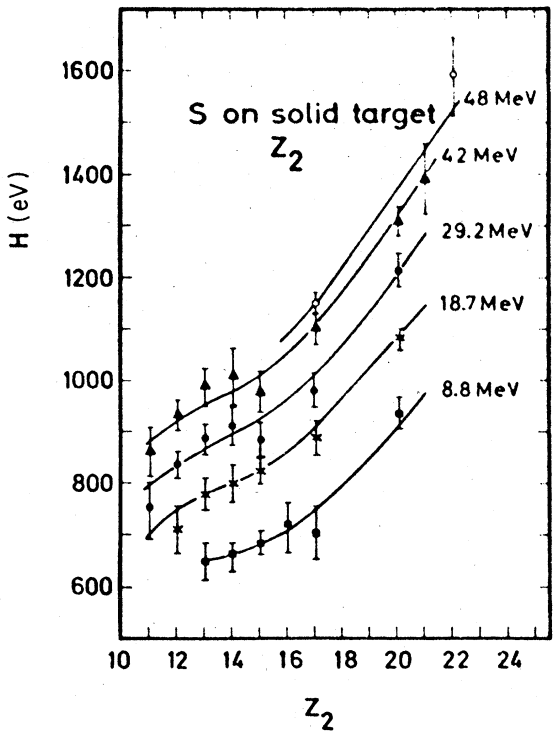

FIG. 24. Measured and calculated half-widths H for the falloff of the MO x-ray intensity beyond the UA K x-ray energies (Schmidt-Böcking *et al.*, 1978b). The curves were calculated using Eqs. (4.24) and (4.25) (see text).

where (Betz *et al.*, 1975)

$$H \sim 0.3(\hbar v \Delta E_x / \Delta R)^{1/2} . \quad (4.25)$$

Comparison of half-widths H have been made in a number of collisions (Betz *et al.*, 1975,1976; Schmidt-Böcking *et al.*, 1978b; Anholt, 1978a; Vincent and Greenberg, 1979; and Stoller *et al.*, 1981). In Eq. (4.25), Betz *et al.* (1975) proposed using the difference between the UA and higher-Z SA $K\alpha$ transition energies for ΔE_x and $\Delta R = (1 + Z_L/Z_H)/Z_H$ in atomic units. In subsequent work, there is some minor confusion about the magnitude of ΔR, and whether MO x-ray cross sections should be fitted to $\omega \exp(-0.693\omega/H)$ or $\exp(-0.693\omega/H)$. The half-width values H differ by 5—10%, depending on whether one takes the former form (Betz *et al.*, 1975,1976; Anholt, 1978a; Vincent and Greenberg, 1979; Stoller *et al.*, 1981) or the latter (Schmidt-Böcking *et al.*, 1978b). In later versions (Betz *et al.*, 1976), ΔR was increased by a factor of 1.22. The sum of radii ΔR is incorrectly given in Anholt (1978a) (inconsequentially, for the symmetric collisions considered there).

Figure 24 compares calculated half-widths with measurements for 8.8- to 48-MeV S collisions (Schmidt-Böcking *et al.*, 1978b). The measured values in these collisions [fitted with the form $\exp(-0.693\omega/H)$] are in good agreement with theory (without the factor of 1.22 in ΔR).

The calculated MO x-ray tail intensities in Ni + Ni collisions are not in good agreement with experiment except in the lowest-velocity collisions (Fig. 18). This is reflected in the variation of the half-width H with beam energy (Fig. 25). The dynamic theory of Macek and Briggs predicts that H should vary as $v^{1/2}$ or E^a with $a = \frac{1}{4}$. Fitting the electron-slip calculations of Anholt (1978a), one obtains $a = 0.23 \pm 0.01$, in reasonable agreement with $a = \frac{1}{4}$. The experimental value, however, is 0.285 ± 0.015 (Vincent and Greenberg, 1979). Other dynamic theories give $a = \frac{1}{4}$ (Müller, 1975) and $a = \frac{1}{3}$ (Fritsch and Wille, 1979). Anholt (1978a) surmised that contributions from one-collision MO x rays, which increase with beam energy relatively faster than the two-collision contributions, may be present in Ni + Ni collisions, and H may be higher for one-collision than for two-collision MO x rays. The latter point was investigated by Stoller *et al.* (1981), who measured half-widths in Cl + Ar gas-target collisions where only one-collision x rays are present. At high projectile energies, the one-collision gas-target half-widths are larger than the solid-target ones. At low projectile velocities, the gas-target widths are smaller than the solid-target ones, suggesting that the one-collision H value is smaller than the two-collision one there.

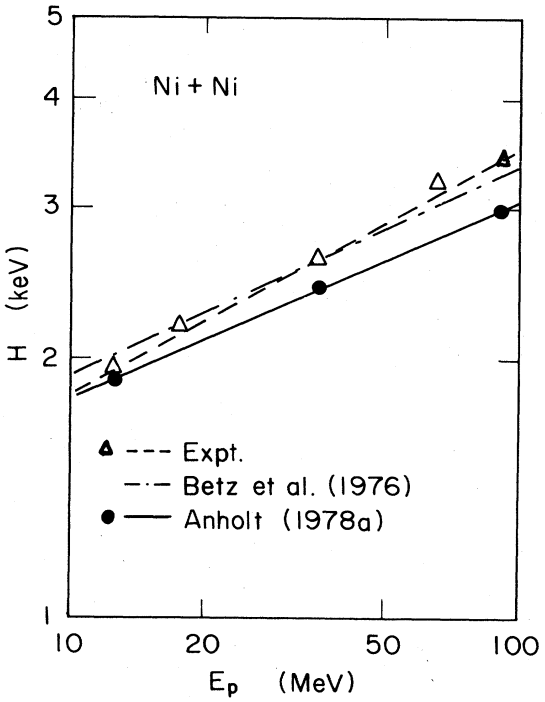

FIG. 25. X-ray intensity falloff parameters H vs the ^{58}Ni projectile bombarding energy. The measured points (Vincent, 1977) are connected by dashed lines, the theoretical results from the dynamical calculations including electron slip are shown by the solid lines, and the dot-dashed curve was calculated using the expressions of Betz *et al.* [1976; Eqs. (4.24) and (4.25)].

D. $2p\sigma$ molecular-orbital x rays

1. Near-symmetric collisions

In many measurements of $1s\sigma$ MO x rays, a continuum ($C1$ in Fig. 26) lying between the SA K x-ray lines and the $1s\sigma$ MO continuum ($C2$) is observed. Heinig *et al.* (1976) first suggested that this continuum was due to MO x-ray transitions into the $2p\sigma$ MO during the collision. The continua have been called $2p\sigma$ MO x rays (Heinig *et al.*, 1977; Anholt and Meyerhof, 1977), intermediate KL MO x rays (Heinig *et al.*, 1976), and $2p\Pi_x$ MO x rays (Anholt, 1979a). The x rays appear above the SA K x-ray lines because the $2p\sigma$ electronic energy has a deep minimum at intermediate internuclear distances (see Figs. 5—7), allowing larger transition energies at intermediate internuclear distances than the SA K x-ray energies. The x rays are produced in the same collision in which the $2p\sigma$ vacancy is made. The $2p\sigma$ vacancy is generally made via $2p\sigma$-$2p\pi$ Coriolis coupling transitions if the initial $2p\pi$ vacancy is made either in a prior collision or by excitation or ionization early in the same collision (Meyerhof *et al.*, 1977). The $2p\sigma$ MO x-ray continuum is much more intense than the one-collision $1s\sigma$ continuum, since $2p\sigma$-vacancy production is much more likely than $1s\sigma$-vacancy production. Because $2p\sigma$ MO and two-collision $1s\sigma$ MO x-ray production both depend on $2p\sigma$-vacancy production, but two-collision $1s\sigma$ MO x-ray production is reduced by the low probability of undergoing a second collision before the K vacancy decays, $2p\sigma$ MO x-ray production is much more probable than two-collision $1s\sigma$ production.

Various dynamic calculations of $2p\sigma$ MO x-ray pro-

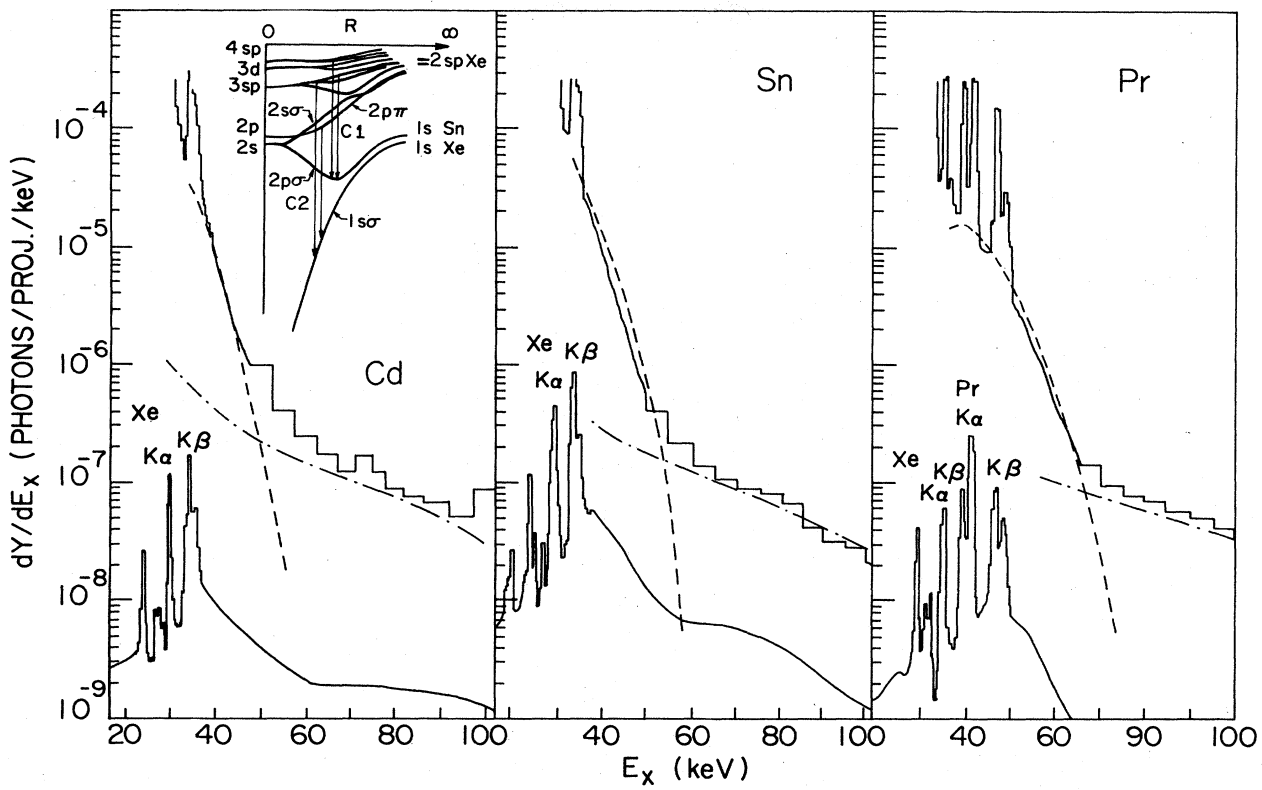

FIG. 26. Yields of continuum x rays observed in 470-MeV Xe + Cd, Sn, and Pr collisions. The calculated $2p\sigma$ or $C1$ MO x-ray yields (dashed lines) and the $1s\sigma$ or $C2$ MO x-ray yields (dot-dashed curve) are shown. The lower inset shows the original spectrum (counts/channel, arbitrarily normalized), where a 0.75-g/cm^2 Cu absorber was used to attenuate low-energy radiation. The upper inset shows a qualitative MO correlation diagram, showing typical transitions contributing to the $C1$ and $C2$ x-ray continua (Anholt and Meyerhof, 1977).

duction have been made (Heinig *et al.*, 1977; Anholt and Meyerhof, 1977; Anholt, 1979a; Jäger *et al.*, 1981). Using Eq. (3.14), one obtains the MO x-ray intensity from the Fourier transform of the dipole velocity matrix element:

$$D_{\sigma i}(b,\omega)=\frac{1}{\sqrt{2\pi}}\int_{-\infty}^{\infty} dt\, a_{2p\sigma}(t)D_{\sigma i}[R(t)] \times\exp\left[i\int_0^t dt'[\omega-\omega_{\sigma i}(t')]\right], \tag{4.26}$$

where $a_{2p\sigma}(t)$ is the $2p\sigma$-vacancy production amplitude obtained from the Coriolis coupling equations [Eq. (3.44)] with the initial conditions $a_{2p\pi}(-\infty)=1$ and $a_{2p\sigma}(-\infty)=0$. Generally, the probability of having an initial $2p\pi$ vacancy $|a_{2p\pi}|^2$ is less than unity. The MO x-ray intensities are therefore normalized to the SA K-vacancy production cross section or yield. The MO x-ray intensity per $2p\sigma$ vacancy is obtained using

$$\frac{1}{\sigma_{2p\sigma}}\frac{d\sigma_{2p\sigma\mathrm{MO}}}{dE_x}=\int_0^{\infty}2\pi b\,db\,\tfrac{4}{3}\alpha^3\omega\frac{|D_{\sigma i}(b,\omega)|^2}{\sigma_{\mathrm{rot}}}, \tag{4.27}$$

where

$$\sigma_{\mathrm{rot}}=\int_0^{\infty}2\pi b\,db\,|a_{2p\sigma}(b,\infty)|^2. \tag{4.28}$$

This quantity should be identical to the measured MO x-ray cross section divided by the $2p\sigma$-vacancy production cross section, and approximately equal to the MO x-ray thick-target yield divided by the $2p\sigma$ thick-target vacancy yield (Anholt and Meyerhof, 1977). A verification of this relationship has been made by Frank *et al.* (1978), who measured $2p\sigma$ MO x-ray and $2p\sigma$-vacancy production in 0.51-MeV/amu Kr + Nb and Nb + Kr collisions. In the solid Nb target, $2p\pi$ vacancies can be made in a double collision process, but in the Kr gas target $2p\pi$ vacancies must be made early in the collision before rotational coupling occurs. Although the $2p\sigma$ MO x-ray and vacancy production yields are an order of magnitude smaller in the gas target, identical MO x-ray yields per $2p\sigma$ vacancy

(or Kr K x-ray) were found.

Figure 26 shows calculations of MO x rays in 470-MeV Xe + Cd, Sn, and Pr collisions (Anholt and Meyerhof, 1977). In these calculations, only $2p\sigma$-$3d\sigma$, -$3d\pi$, -$4d\sigma$, and -$4d\pi$ transitions were considered. These give the largest transition rates, as shown in Fig. 10. The calculated hydrogenic $2p\sigma$ binding energies were adjusted semiempirically to give the correct SA and UA values. Thick-target yields were measured, which were calculated using measured $2p\sigma$ thick-target vacancy production yields (Meyerhof *et al.*, 1977). The spectral shapes are in reasonable agreement with experiment, though the calculated intensities are factors of up to three times higher than experiment (in Xe + Sn collisions). We consider this below.

Several calculations of $2p\sigma$ MO x-ray production considered possible $2p\sigma$ MO x-ray line tails. Fourier transforms of rapidly varying functions of time produce frequency spectra that fall off slowly with ω (Anholt, 1976). The function that varies most rapidly with time is a step function, used by Heinig *et al.* (1977) for $a_{2p\sigma}(t)$:

$$a_{2p\sigma}(t)=\begin{cases} a_{2p\sigma}(\infty) & \text{for } t>0 \\ 0 & \text{for } t<0. \end{cases} \tag{4.29}$$

This gives an MO x-ray intensity falling off as ω^{-2} beyond the end of the observed $2p\sigma$ MO x-ray spectrum, and can even exceed the $1s\sigma$ MO x-ray intensity. This approximation can be used to calculate the $2p\sigma$ MO x-ray intensity at small x-ray energies (Anholt and Meyerhof, 1977), but breaks down at high x-ray energies. Jäger *et al.* (1981) found that the use of realistic time-dependent amplitudes $a_{2p\sigma}(t)$ reduces the magnitude of this tail by 1–2 orders of magnitude, so that the tail intensity falls off more steeply with frequency ω, and is no longer more intense than $1s\sigma$ MO x rays. However, Jäger *et al.* also Fourier-transformed the dipole vector $\mathbf{D}_{\sigma i}[R(t)]$ instead of the magnitude, assuming the MO wave functions and therefore $\mathbf{D}_{\sigma i}[R(t)]$ follow the rotation of the internuclear axis. This introduces, for small impact parameters, a swiftly varying component into the Fourier transform which increases the magnitude of the tail.

The tail intensity is much reduced when one makes full dynamic calculations including the Coriolis coupling between the $2p\sigma$ and $2p\pi$ MO's and the initial $d\sigma$, $d\pi$, and $d\delta$ MO's (Anholt, 1979a). The calculations are similar to those described for $1s\sigma$ MO x rays in Sec. III.C.2. The initial and final wave functions are

$$\Psi_{2\Pi x}=a_{\pi x}(t)\chi_{2p\pi}(t)+a_{\sigma}(t)\chi_{2p\sigma}(t)\ , \tag{4.30}$$

$$\Psi_i=b_{id\sigma}(t)\chi_{d\sigma}(t)+b_{id\pi x}(t)\chi_{d\pi x}(t)+b_{id\pi y}(t)\chi_{d\pi y}(t)+b_{id\delta xy}\chi_{d\delta xy}(t)+b_{id\delta x^2-y^2}\chi_{d\delta x^2-y^2}\ ,$$

where the amplitudes b_{ij} are obtained by numerically solving $3d\sigma$, $3d\pi$, and $3d\delta$ Coriolis coupling equations with the initial conditions

$$b_{ij}(-\infty)=\delta_{ij}\ . \tag{4.31}$$

For example, the 3Σ MO is equal to the $3d\sigma$ MO at $t=-\infty$, and so on. The production of $2p\pi_x$ and $2p\pi_y$ vacancies is more likely than the production of $2p\sigma$ ones. Since the $2\Pi_y$ MO x-ray intensity is negligible in the region of interest, one can call these x rays $2\Pi_x$ MO x rays, although transitions to the $2p\sigma$ basis functions comprising the $2\Pi_x$ MO dominate.

At very small impact parameters, the $2p$ and d wave functions fail to follow the rotation of the internuclear axis. The direction of the dipole transition element remains relatively fixed, and the rapidly time-varying factor causing $2p\sigma$ line tails is not present. In 56-MeV Nb + Nb collisions (Fig. 27), the calculated $2p\sigma$ line tails are much reduced, though not completely absent above 40 keV, which could be due to numerical inaccuracies.

The difference in the magnitudes of the measured and calculated cross sections in Figs. 26 and 27 is probably due to uncertainties in the molecular transition energies. In analogy with the theory of Macek and Briggs (1974) for $1s\sigma$ MO x rays [Eq. (4.23)], the expected $2p\sigma$ MO intensity varies approximately as

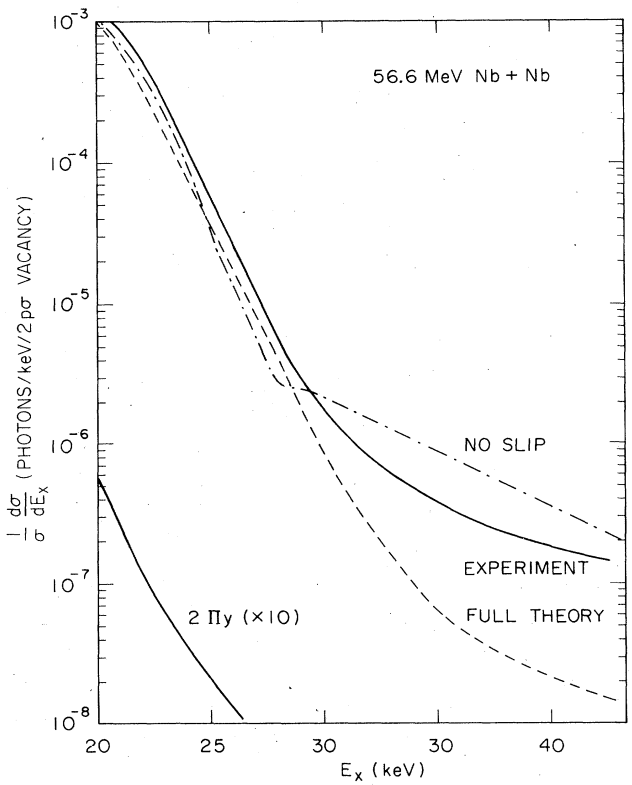

FIG. 27. $2p\sigma$ MO x-ray production cross sections for 56.6-MeV Nb+Nb collisions, measured at 90° to the beam direction (Vincent, 1977; solid line). The experimental cross section is the angular differential cross section per 4π sr, divided by the $2p\sigma$-(projectile+target K-) vacancy production cross section. The calculated cross section including electron slip (full theory; dashed lines) and with no electron slip (dot-dashed curve) are shown. The calculated contributions from the $3d$ to $2\Pi_y$ transitions (multiplied by 10) are shown separately (Anholt, 1979a).

$$\frac{d\sigma}{d\omega} \sim \omega \exp[-\alpha(\omega - \omega^*_{2p\sigma})] , \quad (4.32)$$

where α is a velocity-dependent constant and $\omega^*_{2p\sigma}$ is the maximum $2p\sigma$ transition energy. Since the calculated and measured $2p\sigma$ MO x-ray spectral shapes agree well, independent of collision velocity [Anholt and Meyerhof (1977) for 326- and 470-MeV Xe + Sn; Anholt (1979a) for 36- to 75-MeV Nb + Nb], the disagreement is probably due to the uncertainty in the value of $\omega^*_{2p\sigma}$. For Nb + Nb, one-electron transition energies were used, and the calculations fell a factor of 0.67 below experiment. For Xe + Sn collisions where an adjusted analytical $2p\sigma$ binding energy curve was used, the calculations are factors of 2—3 above experiment. Including or neglecting electron slip makes little difference, as shown in Fig. 27. One can infer that the energy value $\omega^*_{2p\sigma}$ is ~4 keV too low in the Xe + Sn calculations and 1—2 keV too high in the Nb + Nb calculations. Both schemes used to adjust the MO transition energies in these calculations were based on experimental SA and UA transition energies. (In Nb + Nb, the close agreement between the experimental and hydrogenic UA and SA transition energies implied that no adjustment was necessary.) Since it is not the SA or UA energy that determines the intensity in Eq. (4.32), but the maximum transition energy difference $\omega^*_{2p\sigma}$, this points to the limitation of semiempirically adjusting the hydrogenic calculations.

2. Asymmetric collisions

In a quasistatic calculation of $2p\sigma$ MO x-ray production, the cross section, proportional to the inverse of the derivative of the transition energy $d\Delta E_{if}/dR$ [Eq. (3.4)], should peak at the maximum transition energy $\omega^*_{2p\sigma}$ where the derivative is nearly zero. In a dynamical calculation, the peak is still present, but is broad, and the peak position is shifted to slightly lower transition energies (Anholt and Meyerhof, 1977). Usually, this peak is not observed, because it lies beneath the SA K x-ray lines. For instance, in Nb + Nb collisions the peak is expected to be slightly below 21 keV, but the Nb $K\beta$ x-ray line at 19 keV, with a half-width of ~1 keV, prevents the observation of the $2p\sigma$ MO x-ray peak. Searches for this peak have been made in very asymmetric collisions (Anholt and Meyerhof, 1977; Stöckli, 1979; Stöckli and Anholt, 1984).

Figure 28 shows measurements in 5- to 56-MeV Br + V collisions, where the peak is indeed visible at very low bombarding energies. The calculated MO x-ray intensities were obtained as follows. Full electron-slip calculations were done, including transitions from the $3d\Sigma$, $3d\Pi_x$, and $3d\Pi_y$ MO's (the other d MO's probably being unfilled in these collisions), and the hydrogenic molecular transition energies were multiplied by an adjustable constant. The x-ray energy fitting procedure gives the correct spectral shape at all energies, but the calculated intensity is slightly below experiment at high projectile energies. The value of the fitting constant, 0.91, is

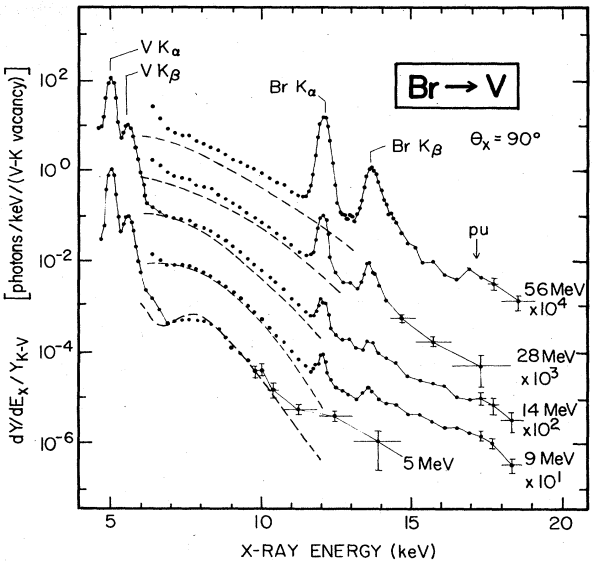

FIG. 28. Spectra of $2p\sigma$ MO x rays (6—12 keV) and Br and V K x rays seen in 5- to 56-MeV Br + V collisions. The dashed line is a theoretical calculation of $2p\sigma$ MO x rays by Stöckli and Anholt (1984), described in the text.

surprisingly high, because it gives a 5.7-keV UA $3d$-$2p$ transition energy, while the experimental $L\beta_1$ ($2p\frac{1}{2} \rightarrow 3d\frac{3}{2}$) energy is 5.25 keV and the hydrogenic value is 6.25 keV. That the MO x-ray intensity gives a UA transition energy closer to the hydrogenic than to the many-electron value indicates that $\omega^*_{2p\sigma}$ is less sensitive to many-electron screening effects than expected.

E. *L* molecular-orbital x rays

The first observation of quasimolecular x-ray emission was interpreted as x-ray transitions to $2p\pi$ MO's in Ar + implanted Ar collisions in Si targets (Saris *et al.*, 1972). Subsequent work, however, showed that the x rays are emitted in Si + Ar collisions. MacDonald and Brown (1972) measured continuum x rays in solid Ar targets, and showed that the spectrum extends to larger x-ray energies than those observed by Saris *et al.* (1972), consistent with the possibility that Saris *et al.* observed the lower-energy Ar + Si x rays. Cairns *et al.* (1974) showed that the Ar L x-ray, and therefore the $2p$-vacancy, population builds up with the Ar ion dose. Since two-collision MO x-ray production requires the presence of a $2p$ vacancy, the Ar + Ar MO x-ray yield per $2p$ vacancy should itself vary linearly with the dose [proportional to the factor n_2 in the two-collision formulas, Eq. (3.6) or (3.48); Meyerhof *et al.*, 1974]; thus the MO x-ray yield should vary quadratically with the dose. From the linear variation, one can infer that the Ar $2p$ vacancy was carried into Ar + Si collisions.

Bissinger and Feldmann (1973) measured continuum x

rays in Ar + Al collisions where the Al target was sufficiently thin to prevent Ar ion implantation. The observed spectrum shape is consistent with that seen in thick-target Ar + Al collisions, therefore implying that the continuum x rays are from Ar + Al instead of Ar + Ar collisions. Bissinger and Feldmann (1975) also studied the MO x-ray "end points" in S, Cl, Ar, K, Ca, and Ti + Si collisions and found them to be consistent with projectile-target MO x rays instead of projectile + (implanted) projectile MO x rays. Collisional broadening prevents the determination of absolute energies from MO x-ray end points, but the relative shifts in the spectra measured by Bissinger and Feldmann indeed show that the spectra vary as the UA energy in projectile-target collisions instead of the UA energy in projectile-projectile ones.

Finally, Lurio *et al.* (1975) measured the MO continuum spectrum with a high-resolution spectrometer ($\Delta E_{\rm res}=5$ eV), which showed that the spectrum is indeed a continuum instead of a series of unresolved lines.

Only one computation of L MO x rays has been made. Morovic *et al.* (1977) made calculations for 17-MeV I + Sn collisions based on the Xe + Ag RHFS correlation diagram in Fig. 7. In high-Z_u collisions, the observed L MO x rays are possibly made in transitions to the $3d\sigma$ MO, hence could be called M MO x rays. Morovic *et al.* assumed that the vacancies in the 3σ, 4σ, 5σ, and 6σ MO's in Fig. 7 are populated by $3p$ and $3d$ Coriolis coupling near the internuclear distance of closest approach, followed by a series of Landau-Zener transitions. The predominant vacancy pathway then would be parallel to the $3d\sigma$ curve in the diabatic one-electron correlation diagram (Fig. 5). For $3d\sigma$ MO x rays, the continuum x rays should extend up to ~15 keV in Xe + Ag collisions, but the $2p\pi$ spectrum extends to ~30 keV. In the similar 17-MeV I + Sn collisions, x rays are observed up to ~13 keV, consistent with the $3d\sigma$ MO x-ray interpretation, though background could prevent the observation of higher-energy continuum x rays. The $3d\sigma$ MO x-ray spectrum should be more intense than the $2p\pi$, because the $3d\sigma$ vacancies could be made by Coriolis transitions of vacancies from the I M shell. The $2p\pi$ MO x rays must originate from fewer I $2p$ vacancies.

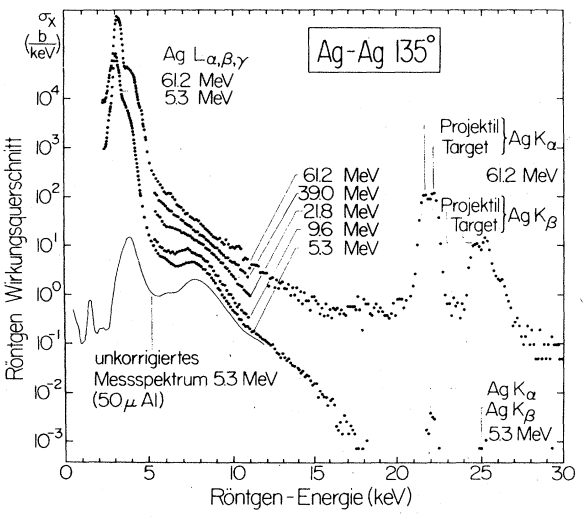

FIG. 29. Absorber-corrected (and -uncorrected for 5.3-MeV collisions, as shown by the solid line) x-ray spectra seen in 5.3- to 61-MeV Ag + Ag collisions at a detector angle of 135° (Stöckli, 1979). The continuum extending from 5 to 15 keV displays a peak at low projectile velocities and is possibly due to $3d\sigma$ MO x rays.

Stöckli (1979) attempted to distinguish $2p\pi$ and $3d\sigma$ MO x-ray production in the 5- to 15-keV continuum x rays seen in 5.3- to 61-MeV Ag + Ag collisions. The minimum in the $3d\sigma$ binding energy at intermediate internuclear distances should give a peak in the MO x-ray spectrum, similar to that seen for $2p\sigma$ MO x rays. Indeed, such a peak is seen in 5.3- and 9.6-MeV Ag + Ag collisions (Fig. 29); only a flat or exponential falloff is seen in higher-energy collisions (and in the 17-MeV I + Sn collisions). A quantitative interpretation of these results has not been made, however.

F. *M* molecular-orbital x rays

Mokler *et al.* (1972) observed (6—9)-keV continuum x rays in 11- to 57-MeV I + Au collisions, similar to those shown in Fig. 30 for lower-energy 1.5- to 5.5-MeV Xe + Au collisions (Lutz *et al.*, 1976). The MO x rays were thought to be due to transitions into $3d\pi$ vacancies, fed by SA I $2p$ vacancies made in a prior collision. Mokler *et al.* showed that the MO x-ray intensity is approximately consistent with this interpretation, using a version of the two-collision quasistatic formula [Eq. (3.6)] for the integrated MO x-ray cross section:

$$\sigma_{\rm MO}\approx\sigma_{\rm I2p}n_2\pi R_{\rm eff}^3\lambda_{\rm UA}/\lambda_x\ , \tag{4.33}$$

where $\sigma_{\rm I2p}$ is the I $2p$ x-ray cross section, $R_{\rm eff}$ is the average internuclear distance where $3d\pi$ MO x rays are emitted (0.2 a.u. in I + Au collisions), and $\lambda_{\rm UA}$ is the average MO x-ray transition rate taken as the UA $3d$ decay rate. This argument is based on crude estimates of the molecular quantities, and therefore leaves room for the possibility that some of the MO x rays come from other transitions.

These continuum x rays could also be made by transitions to $4f\sigma$ vacancies, and hence could be called N MO x rays. It is especially noteworthy that the continuum x-ray spectrum is peaked [even when corrected for low-energy x-ray attenuation in the Al absorber used by Mokler *et al.* (1975)], implying, in analogy with $2p\sigma$ MO x-ray production, that the MO x rays come from an orbital with a minimum energy at intermediate internuclear distances. The principal possibilities seen in the hydrogenic electron correlation diagram for I + Au collisions in Fig. 31 are transitions to the $4f\sigma$ MO (minimum energy equal to 22 keV at $R\sim0.18$ a.u.), the $3d\pi$ MO (minimum energy 26 keV at $R\sim0.06$ a.u.), the $3p\sigma$ MO (minimum 30 keV at $R\sim0.03$ a.u.), and the $3d\sigma$ MO (minimum 37 keV at $R\sim0.09$ a.u.). The calculated hydrogenic maximum binding energies are not usable for multielectron I + Au

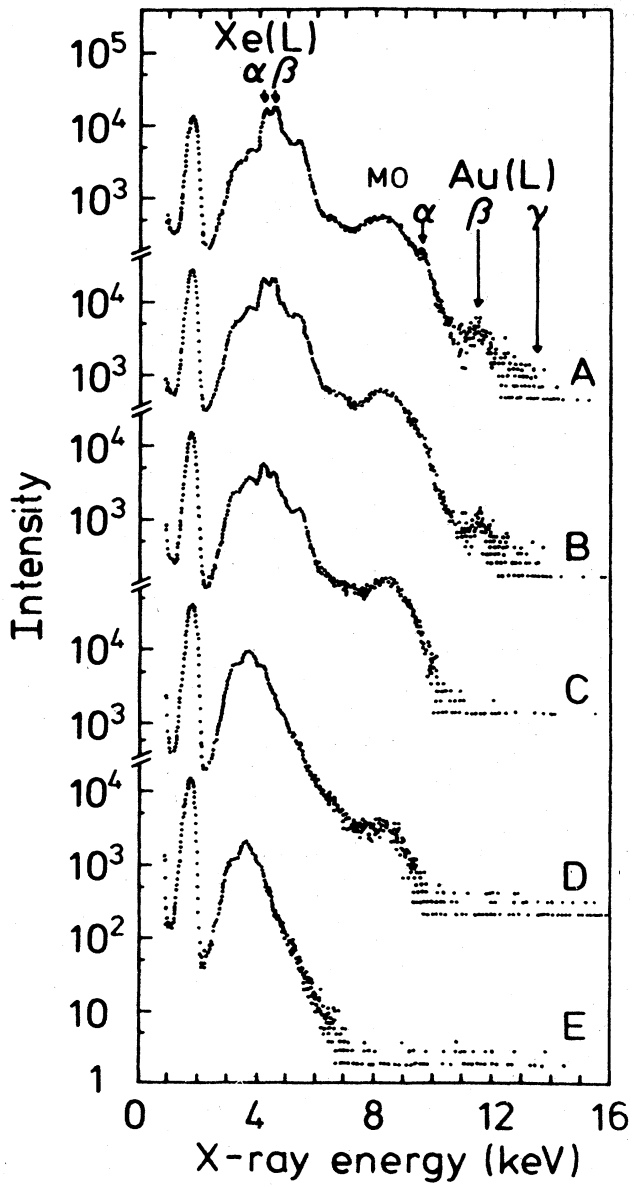

FIG. 30. Spectra of x rays excited in Xe + Au collisions (not corrected for the 29-μm Al absorber). Collision energies: *A*, 5.5 MeV; *B*, 4 MeV; *C*, 3 MeV; *D*, 2 MeV; and *E*, 1.5 MeV (Lutz *et al.*, 1976).

collisions, due to electron screening. The data in Fig. 30 show that the continuum cross section has a threshold near 1.5 MeV in Xe + Au collisions, which is probably the threshold for $4f$ Coriolis coupling, as shown below.

Coriolis coupling thresholds normally occur at the point where the product of the minimum momentum transfer q and the internuclear distance of closest approach d is near unity (Taulbjerg *et al.*, 1976),

$$qd \approx 1 . \tag{4.34}$$

For Coriolis coupling the energy difference between the σ and π levels (or π-δ, δ-φ, etc.) is given by Gerstein and Krivchenkov (1961),

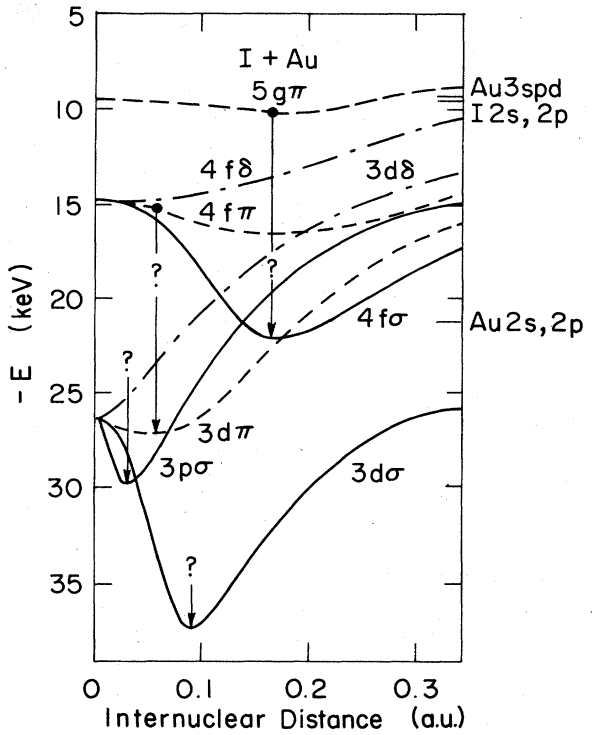

FIG. 31. A correlation diagram for I + Au collisions, calculated using one-electron wave functions, as in Figs. 1 and 5. The solid lines show σ levels, and the dashed lines show π levels. Transitions possibly contributing to I + Au or Xe + Au M MO x rays are shown.

$$\Delta E = \kappa Z_1 Z_2 (Z_1 + Z_2)^2 R^2 , \tag{4.35}$$

where κ is a constant. Since d is given by $2Z_1Z_2e^2/Mv^2$, where M is the reduced nuclear mass, and $q = \Delta E/v$, we have at the threshold velocity

$$\frac{\kappa Z_1 Z_2 (Z_1+Z_2)^2}{v} \left[\frac{Z_1 Z_2 e^2}{M v^2} \right]^3 \approx 1 , \tag{4.36}$$

implying that

$$\left[\frac{\omega}{v} \right]^7 = \frac{\alpha}{\kappa} , \tag{4.37}$$

where (Taulbjerg *et al.*, 1976)

$$\omega^7 = \tfrac{1}{4} Z_1 Z_2 (Z_1+Z_2)^2 \left[\frac{Z_1 Z_2}{M} \right]^3 . \tag{4.38}$$

One can use calculations of $2p\sigma$-$2p\pi$ coupling ($\kappa^{-1}=40$), giving a threshold at $v/\omega = 0.035$, to calibrate the value of α [which has an arbitrary value in Eq. (4.37)]. Using an average value of κ, 2/2835, for $3d\sigma$-π and $3d\pi$-δ, and an average κ value, 10/120 960, for $4f\sigma$-π, π-δ, and δ-φ (Gerstein and Krivchenkov, 1961), one obtains threshold energies of 5.4 MeV and 2 MeV for $3d$ and $4f$ Coriolis coupling in Xe + Au collisions. Gold L vacancies are made by $3d$ Coriolis coupling of I $2p$ vacancies (Hagmann *et al.*, 1978), hence the Au L x rays should disap-

pear below 5.4 MeV, and indeed do disappear, but below 4 MeV as shown in Fig. 30. [Lutz *et al.* (1976) interpret the disappearance of the Au L x rays as due to the fact that the crossing between the 5σ (going to the Au L shell) and 6σ levels is not reached below 4 MeV. Coincidentally, this crossing distance, ~ 0.04 a.u. in Fig. 32, is approximately equal to $R_{\min}$ at the Coriolis coupling threshold. We assume that the crossing is diabatic, and the Coriolis coupling energy transfer determines the disappearance of the Au L x rays.] If the MO x rays are transitions to $4f\sigma$ vacancies created by $4f$ Coriolis coupling of I M- or N-shell vacancies, the continuum should disappear below 2 MeV, which it indeed does. Our calculation of the threshold energies may be incorrect due to screening, which affects the absolute Z values in Eq. (4.36). However, the relative $3d$ and $4f$ thresholds seem approximately correct.

There are several other points favoring the $4f\sigma$ MO x-ray interpretation. The $4f\sigma$ MO x-ray intensity should be much larger than the $3d\pi$ intensity because many more vacancies are available to the $4f\sigma$ MO from the I M and N shells than to the $3d\pi$ MO from the I $2p$ shell. These MO x rays have also been seen in gas targets $Pb(CH_3)_4$ with approximately one-half of the solid target (Pb) intensity (Lutz *et al.*, 1976). Many fewer I or Xe $2p$ vacancies survive in gas targets than M or N vacancies. The M or N vacancies could be created in collisions with the surrounding C or H atoms in $Pb(CH_3)_4$. Second, the value of R_{eff} calculated by Mokler *et al.* (1972) in support of the $3d\pi$ MO x-ray interpretation is much larger than the internuclear distance, 0.06 a.u., where the $3d\pi$ minimum energy occurs. If most of the $3d\pi$ MO x rays are made at $R_{\text{eff}}=0.2$ a.u., no peak in the MO x-ray spectrum should be observed. Note also that the peak would not be observed in 2-MeV Xe + Au collisions, where the distance of closest approach, 0.1 a.u., is larger than the internuclear distance where the $3d\pi$ minimum binding energy occurs. This argument also negates the possibility that $3p\sigma$ MO x rays could be observed, as the minimum R value for the $3p\sigma$ MO is not reached for projectile energies below 6 MeV. If $3d\pi$ MO x rays are observed, one expects for projectile energies exceeding 5 MeV that Coriolis coupling will produce vacancies in the $3d\sigma$ MO, giving $3d\sigma$ MO x rays extending beyond the Au x-ray lines. The relatively low intensity of x rays beyond 12 keV suggests that the accompanying $3d\pi$ MO yield should be small.

Since the $4f\sigma$ MO feeds vacancies into the Xe $2p$ shell, the $4f\sigma$ MO x-ray intensity should be correlated with the L x-ray intensity (just as the $2p\sigma$ MO x-ray and SA K-vacancy production cross sections are correlated). As Fig. 30 shows, the continuum x-ray intensity falls off faster than the Xe L x-ray intensity. Some of the Xe L vacancies could be made by $5g\sigma$-vacancy sharing, which does not fall off with decreasing projectile energy as fast as does $4f\sigma$ production. For example, Hagmann *et al.*

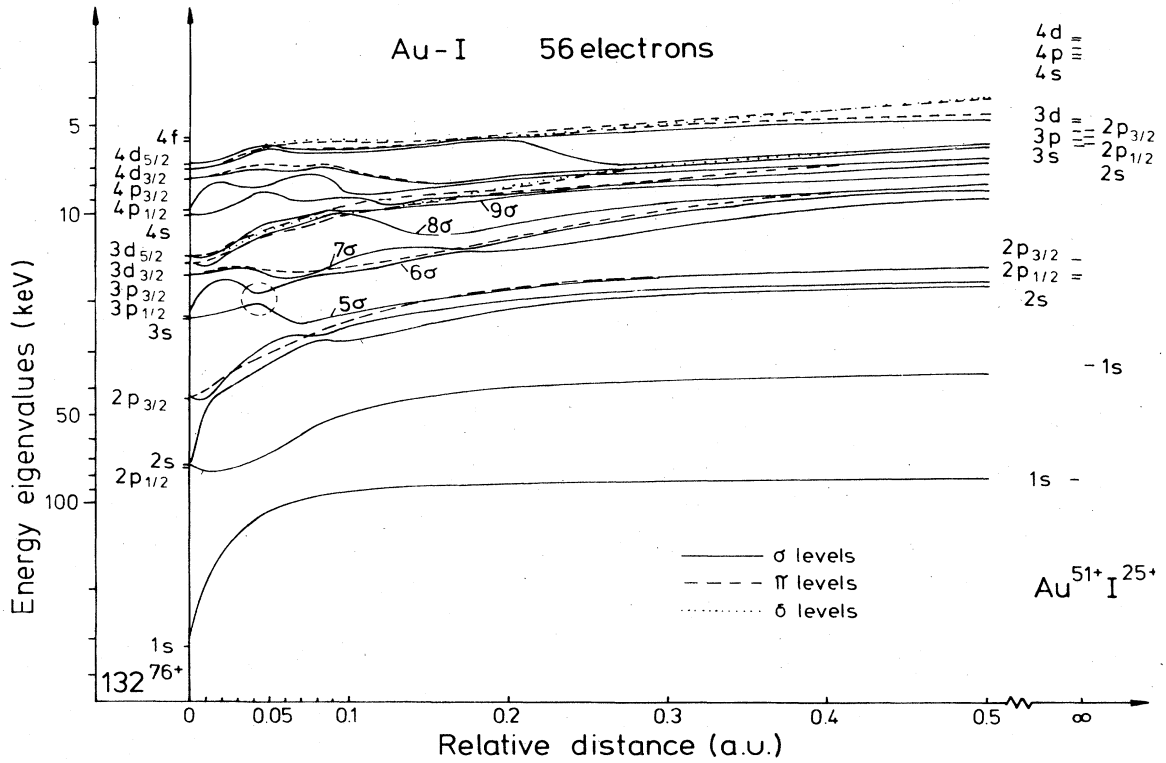

FIG. 32. A self-consistent relativistic correlation diagram for Au + I collisions, including 56 electrons, as in Fig. 7. The relevant levels for the M MO x rays are thought to be the 6σ, 7σ, 8σ, and 2π levels (Fricke *et al.*, 1976).

(1978) interpret the I L-vacancy production in 11-MeV I + Au collisions in terms of $4f\sigma$- and $5g\sigma$-vacancy sharing.

Fricke *et al.* (1976) calculated $3d\pi$ MO x rays in 17-MeV I + Au collisions based on the adiabatic RHFS I + Au correlation diagram in Fig. 32. Despite the fact that good agreement with experiment was found, several problems with this calculation remain. First, the degree of ionization assumed for the quasimolecule, + 76, is excessively high. Even if the projectile were fully stripped, only + 53 could be achieved, and at 15 MeV it is unlikely that more than 30 projectile electrons are absent. The use of a more realistic lower charge state would give lower molecular binding energies because of increased electron screening, affecting considerably the MO x-ray peak position. More importantly, Fricke *et al.* did not diabatize the RHFS correlation diagram. They calculated transitions to adiabatic MO's which undergo several avoided crossings, producing unphysical maxima and minima in many places. Also, since MO x-ray transition rates were not calculated by Fricke *et al.*, but were assumed to be given by

$$\lambda_{if}(R)=\gamma g_i g_f(\Delta E_{if})^3 , \tag{4.39}$$

where γ is a constant, ΔE is the transition energy, and g_i and g_f are orbital degeneracies, this gives unphysical emphasis to the crossings. As discussed in Sec. III.D, since the molecular wave function changes character at the crossings, the transition rate λ_{if} will be discontinuous, partially cancelling out the discontinuity in $d\Delta E_{if}/dR$ at that point. Finally, although absolute agreement between the quasistatic MO x-ray calculation of Fricke *et al.* and experiment is claimed, the magnitude used for γ, the number of $3d\pi$ vacancies assumed, and the conversion of the calculated spectrum to a counts-per-channel spectrum is not discussed, making the assessment of this claim impossible. In conclusion, lacking a better calculation of continuum x rays in I (Xe) + Au collisions, the possibility that the x rays are due to $4f\sigma$-vacancy emission cannot be ruled out.

V. THE ANGULAR DISTRIBUTION OF MOLECULAR-ORBITAL X RAYS

A. Doppler-velocity measurements

The angular distribution of dipole MO radiation is expected to be of the form

$$\frac{d^2\sigma}{d\Omega_{\text{c.m.}}dE_{\text{xc.m.}}}=I_0[1-A_0P_2(\cos\theta)]$$
$$=A(1+\eta\sin^2\theta) , \tag{5.1}$$

where A is a constant, and η is the anisotropy [Eq. (3.42)]. The forward (+45°)-backward (135°) center-of-mass symmetry is not seen in the laboratory frame due to three effects (Vincent *et al.*, 1978): First, the Doppler shift is given by

$$E_{x\text{lab}}=E_{x\text{c.m.}}(1-\beta\cos\theta)^{-1}(1-\beta^2)^{1/2} , \tag{5.2}$$

where β is the velocity of the emitting system. This shifts the intensity at a given c.m. x-ray energy to a higher lab energy at forward angles and a lower one at backward angles. As the $1s\sigma$ MO x-ray intensity falls off exponentially with x-ray energy, this increases the forward lab intensity over the backward intensity. Second, the c.m. solid angle is related to the laboratory solid angle by

$$\frac{d\Omega_{\text{c.m.}}}{d\Omega_{\text{lab}}}=\frac{1-\beta^2}{(1-\beta\cos\theta_{\text{lab}})^2} , \tag{5.3}$$

which also increases the forward intensity per laboratory solid-angle unit over the backward intensity. Finally, the Lorentz angle shift, given by

$$\cos\theta_{\text{c.m.}}=\frac{\cos\theta_{\text{lab}}-\beta}{1-\beta\cos\theta_{\text{lab}}} , \tag{5.4}$$

alters the c.m. angle from the measured angle.

To first order the relativistic angle shift [Eq. (5.4)] can be neglected, especially if the x-ray detector subtends a solid angle with $\Delta\theta_{\text{lab}}$ much greater than the angle shift. By measuring the forward-backward asymmetry, one can determine the Doppler velocity, and correct measurements at $\theta_{\text{lab}}=90°$ and 0°, to obtain the MO x-ray anisotropy. If one wishes to take into account the angle shift, one can then use the measured anisotropy to correct the lab angular distribution, recalculate the Doppler velocity and the anisotropy, and so on until one obtains a self-consistent velocity and anisotropy (Vincent *et al.*, 1978).

The determination of the Doppler velocity not only obtains the correct conversion between the laboratory anisotropy and the desired c.m. anisotropy, but also gives direct information on the emitting system. If the continuum x rays are quasimolecular x rays, the Doppler velocity should be the velocity of the nuclear center of mass or $v/2$ in symmetric collisions. Projectile x rays have the laboratory Doppler velocity; target x rays are usually emitted from stationary target atoms. The Doppler velocity has been measured in several experiments, and has generally been found to be in agreement with the nuclear c.m. velocity: for $1s\sigma$ MO x-ray production in 2.4-MeV/amu Kr + Zr collisions (Meyerhof *et al.*, 1975), for M MO x-ray production in 6- to 45-MeV I + Au collisions (Folkmann *et al.*, 1976), for 4.2-MeV/amu Pb + Pb collisions (Stoller *et al.*, 1980), for 67-MeV Nb + Nb collisions (Frank *et al.*, 1976), and for 64.8-MeV Ni + Ni collisions (Vincent *et al.*, 1978). Figure 33 shows MO x-ray and emitter velocity spectra seen in Ni + Ni collisions. The 64.8-MeV Doppler-velocity spectrum is nearly consistent with the c.m. Doppler velocity $\beta_{\text{c.m.}}$. A slight increase is seen at low x-ray energies, possibly due to REC contributions emitted with the projectile Doppler velocity. The 12.6-MeV Ni + Ni data disagree with the c.m. Doppler velocity, decreasing to $\beta=0$ in some places. The cause for this is unknown. Most back-

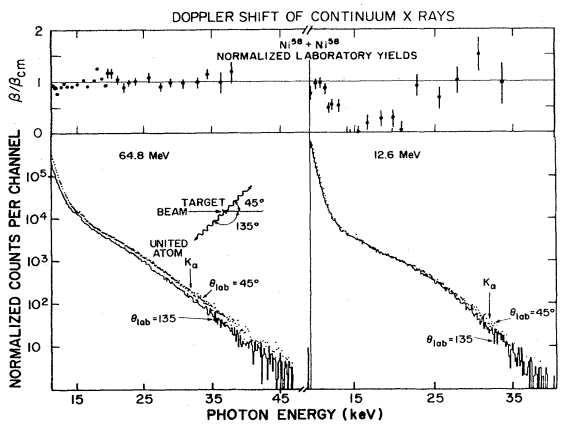

FIG. 33. MO x-ray and Doppler-velocity spectra seen in 12.6- and 64.8-MeV Ni + Ni collisions (adapted from Vincent *et al.*, 1978). The upper figures show the ratio of the measured emitter velocity to the c.m. velocity vs the continuum x-ray energy. The bottom curves show x-ray spectra taken at 45° and 135°, from which the emitter velocities were derived. The $1s\sigma$ MO x-ray spectrum extends from about 15 to 45 keV.

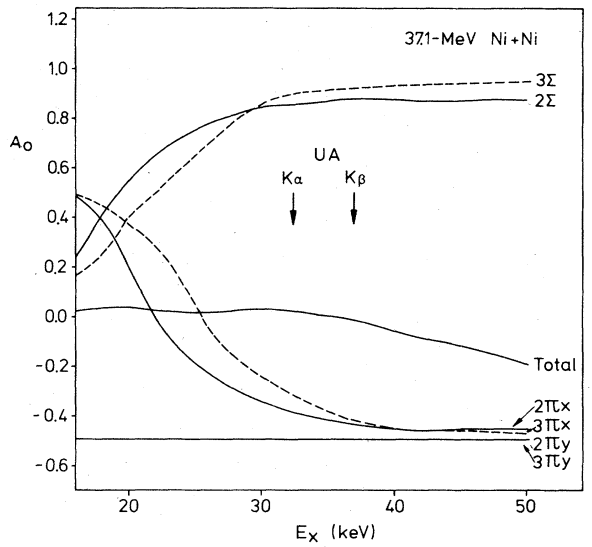

FIG. 34. Angular distribution A_0 parameters for individual MO x-ray transitions, calculated including Coriolis coupling. If all MO's are equally occupied, the total A_0 parameter, and therefore the MO x-ray anisotropy, is nearly zero (Anholt, 1978a).

ground radiation, e.g., REC, PB, and SEB, has a strong forward-backward asymmetry, which would tend to indicate positive Doppler velocities. Recoil MO x-ray production is negligible in 12.6-MeV Ni + Ni collisions (Meyerhof and Anholt, 1979).

B. Origin of the $1s\sigma$ molecular-orbital x-ray anisotropy

1. Two-collision MO x rays

Our understanding of the $1s\sigma$ MO x-ray anisotropy is based upon two facts. Due to Coriolis coupling, the MO's remain aligned in the laboratory system, despite the rotation of the internuclear axis. However, this by itself does not produce a net anisotropy. The net positive anisotropy is caused by higher electron populations in σ MO's than in π MO's. Because the σ-σ transition dipole is aligned initially along the beam axis and remains aligned along that axis throughout the collision, x rays are emitted preferentially perpendicular to the beam axis, giving a positive anisotropy [$\eta = d\sigma(90)/d\sigma(0) - 1 > 0$]. The π-σ dipole remains aligned perpendicular to the beam axis, so radiation is emitted parallel to that axis, giving a negative anisotropy. An equal number of $2p\sigma$ and $2p\pi$, $3p\sigma$ and $3p\pi$ electrons produces a near-zero anisotropy. More electrons in the σ MO's give a higher σ-σ transition intensity, hence a positive anisotropy.

The orbital alignment is illustrated in Fig. 34, where we plot individual A_0 parameters for several transitions $i \to f$, where A_{0if} is given by [Eq. (3.41)]

$$A_{0if} = \frac{3I_{zif} - I_{0if}}{2I_{0if}} . \tag{5.5}$$

At high x-ray energies, the $2\Sigma \to 1s\sigma$ and $3\Sigma \to 1s\sigma$ alignment parameters approach unity, implying that $I_{zif} = I_{0if}$; in other words, the transition dipole is along the z or beam axis. We say that MO radiation is aligned along the z axis if $A_0 = 1$, but this actually means that radiation is emitted perpendicular to the z axis [$I(90°) \sim 1 + 0.5A_0 \approx 1.5$; $I(0°) \sim 1 - A_0 \approx 0$]. For the $\Pi_y \to 1s\sigma$ transitions, A_{0if} is exactly $-\frac{1}{2}$, implying that $I_{zif} = 0$. The Π_y MO is parallel to the rotation axis, hence the $\Pi_y \to 1s\sigma$ dipole does not rotate, so the Fourier transform of the dipole transition vector has only a y component. The $\Pi_x \to 1s\sigma$ intensity approaches $-\frac{1}{2}$ at large x-ray energies, also implying that $I_{zif} = 0$. The Π_x-$1s\sigma$ intensity is aligned along the x axis.

In Fig. 34, the total A_0 parameter, calculated assuming that all $2p$ and $3p$ MO's are equally populated, is near zero. To produce a positive anisotropy, or A_0 value, we require a larger Σ intensity than Π intensity, which is possible if there are more initial vacancies in the π MO's than in the σ MO's. By inspection of correlation diagrams, we see that this is usually the case, assuming the projectile carries a distribution of vacancies into the collision, inversely proportional to the electron binding energy. While the $2p\sigma$ MO correlates to the projectile or target K shell, the $2p\pi$ MO's correlate to the projectile or target L shells, implying the likelihood of more $2p\pi$ than $2p\sigma$ vacancies. While the $3p\sigma$ MO correlates to the SA L shells, the $3p\pi$ correlates to SA M shells, so that the $3p\sigma$ population should exceed the $3p\pi$ population.

The anisotropies shown in Fig. 35 for Ni + Ni collisions were calculated assuming (i) that the 2Σ MO is fully occupied, (ii) that the populations of the 2Π and 3Σ MO's can be obtained from the L-vacancy number measured by the projectile-target $K\alpha$ x-ray line shifts, and (iii) various occupation probabilities $N_{3\Pi}$ for the 3Π MO

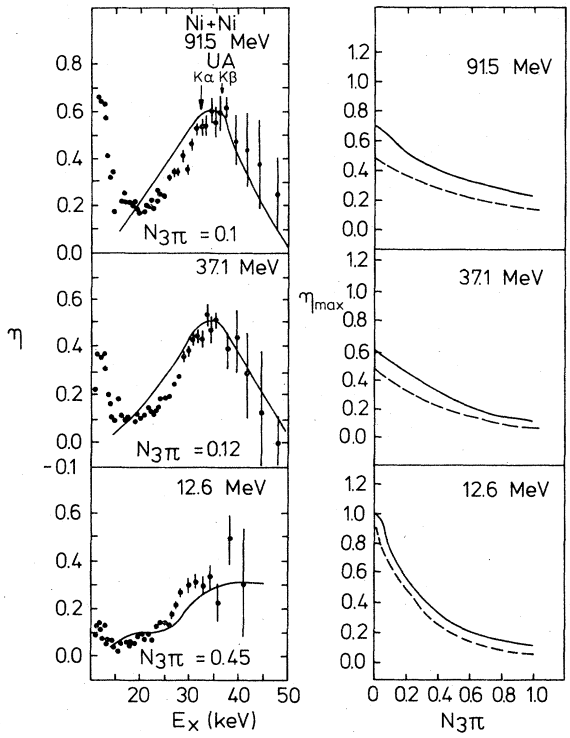

FIG. 35. (a) Measured (Vincent, 1977) and calculated MO x-ray anisotropies for 12.6-, 37.1-, and 91.5-MeV Ni + Ni collisions. The solid lines were calculated assuming that the projectile L vacancies, measured by the SA $K\alpha$ line shifts, all go into the 2Π MO, and using an optimized value of the 3Π occupation number. (b) The maximum value of the anisotropy plotted against the 3Π occupation number, calculated assuming that all L vacancies go into the 2Π MO (solid lines) or that the L vacancies are shared between the 2Π and 3Σ MO's (dashed lines; Anholt, 1978a).

(Anholt, 1978a). The most important conclusion suggested by the MO x-ray anisotropies is that the 3Π MO is relatively unoccupied in 37- and 91-MeV Ni + Ni collisions. The criterion for the formation of MO's requires that the electron velocity v_e be larger than the projectile velocity v. For the 3Π MO, which has a SA binding energy of less than 100 eV (where $v/v_e \gg 1$ for all Ni + Ni projectile energies considered) and a UA binding energy of ~ 1 keV (where $v < v_e$ for all Ni + Ni energies considered), the interpretation of this requirement is ambiguous. That a near-zero 3Π occupation is required to explain the MO x-ray anisotropies, implying that the $3p\pi$ electrons do not form MO's, suggests that the SA electron velocity criterion is most significant.

The shape of the anisotropy spectrum depends on a number of factors. The low-energy MO x-ray intensity comes from collisions with large impact parameters, where the internuclear axis rotates slowly, hence the MO's are no longer aligned in the laboratory frame, and x-ray emission tends to be slightly more isotropic (Fig. 34). The anisotropy falloff at large x-ray energies is due to a subtle difference in the falloff of the Σ and Π intensities. The Σ intensity falls off faster than the Π intensity, so although the vacancy distribution produces a net positive anisotropy near the UA $K\alpha$ and $K\beta$ energies, the more rapid falloff of the Σ intensity enables the Π intensity to eventually exceed the Σ intensity at larger x-ray energies, giving a smaller and even negative anisotropy.

The more rapid Σ falloff can be understood using the equations of Betz *et al.* (1975) and Macek and Briggs (1974) for the intensity above the UA $K\alpha$ energy:

$$d^2\sigma_{if} \sim \omega \exp(-\omega/H_{if}) , \tag{5.6}$$

where H_{if} is proportional to $(d\Delta E_{if}/dR)^{1/2}$. Since the $2p\sigma$ MO correlates to a higher SA binding energy than the $2p\pi$ MO, the derivative near $R=0$ is larger for the $2p\sigma \rightarrow 1s\sigma$ transition than for the $2p\pi \rightarrow 1s\sigma$ transition, implying a larger half-width and a slower intensity falloff. The 2Σ MO is composed of a linear combination of the $2p\sigma$ and $2p\pi$ MO's, the contribution from the $2p\pi$ MO being largest near the internuclear distance of closest approach. Since this is the region contributing most to the high-energy MO x rays, we expect that the half-width for the $2\Sigma \rightarrow 1s\sigma$ transition should be closer to the smaller $2p\pi$ half-width, hence the 2Σ intensity should fall off faster, as required to lower the high-energy anisotropy. Anholt (1978a) has calculated half-widths for the individual 2Σ, 2Π, 3Σ, and 3Π transitions, and finds that the Σ values are always slightly smaller than the Π values.

2. The perfect electron-slip model

The MO alignment can be understood mathematically if we first assume that the σ and π transition dipoles $D_\sigma[R(t)]$ and $D_\pi[R(t)]$ (per electron) are equal, and the σ and π electron binding energies are equal, so that in Eq. (3.46)

$$D_\sigma e^{i\Delta\sigma} = D_\pi e^{i\Delta\pi} . \tag{5.7}$$

Second, for small impact parameters, one can assume that the π-σ energy differences in the Coriolis coupling equation governing the σ and π amplitudes Eq. (3.44) are zero, and the matrix element $\langle \chi_\sigma | \partial/\partial\Theta | \chi_\pi \rangle$ is unity. This gives the kinematic peak solutions (Briggs and Macek, 1972) for the σ and π amplitudes:

$$a_{\sigma\Sigma} = -\cos\Theta(t), \quad a_{\pi x\Sigma} = -\sin\Theta(t), \quad a_{\pi y\Sigma} = 0 , \tag{5.8}$$

and so on. Substitution into Eq. (3.46) gives

$$D_{z\Sigma}(\omega) = \int_{-\infty}^{\infty} dt\, e^{i\omega t}(-\cos^2\Theta - \sin^2\Theta) D_\sigma e^{i\Delta\sigma} ,$$
$$D_{x\Pi x}(\omega) = D_{y\Pi y}(\omega) = D_{z\Sigma}(\omega) , \tag{5.9}$$

and all other values are zero. This gives the A_{0if} parameters at high x-ray energies discussed above.

One of the great surprises of these detailed MO x-ray studies is that the kinematic peak solutions are valid at impact parameters as large as those affecting the total MO x-ray intensity. At very large impact parameters, however, one can no longer set the matrix elements and

energies equal, and the MO's are no longer so perfectly aligned.

The perfect electron-slip model is useful to check the validity of numerical calculations, especially when the equations become much more complicated. For instance, for $2p\sigma$ MO x rays, one includes $2p\sigma$-π Coriolis coupling in the final state and $3d\sigma$-π-δ coupling in the initial state (Anholt, 1979a). One can instruct the computer to set all relevant matrix elements and energies equal, and can compare the relative magnitudes of the calculated x, y, and z intensity components with the perfect electron-slip model for $2p\sigma$ MO x-ray production.

C. Scaling laws and the spectroscopy of molecular-orbital x rays

The theoretical $1s\sigma$ MO x-ray intensities approximately obey a scaling law similar to that discussed in Sec. IV.C.2, so that one can calculate the z component and the total MO x-ray cross sections using

$$\frac{d\sigma_z}{dE_x}=\sum_f n_j\lambda_j f_j I_{zj}(q,\nu,\zeta)$$

and (5.10)

$$\frac{d\sigma_0}{dE_x}=\sum_f n_j\lambda_j f_j I_{0j}(q,\nu,\zeta)\ ,$$

where n_j (≤ 2) is the occupancy of the jth ($=2\Sigma$, $2\Pi_x$, $2\Pi_y$, 3Σ, etc.) MO, λ_j is the UA transition rate for the single $1s$-vacancy atom, and in the perfect electron-slip model, neglecting Coulomb deflection, I_{zj} is given by

$$I_{zj}=q\int_0^\infty B\,dB\left|\int_{-\infty}^{\infty}dz\,d_j(\rho)\exp\left[iq\int_0^z dz'[\nu-\nu_{1s\sigma}(z')+\nu_j(z')]\right]\right|^2\ , \tag{5.11}$$

with a similar expression for I_{0j}, where

$$z=vt/a_{KL},\quad B=b/a_{KL},\quad \rho^2=B^2+z^2\ ,$$

$$d_j(\rho)=D_{1s\sigma\text{-}j}(R/a_{KL})/D_{1s\sigma\text{-}j}(0)\ ,$$

$$q=\omega_0 a_{KL}/v,\quad \nu_i=\omega_i(\rho)/\omega_0\ ,$$

the constant f_j is given by

$$f_j=\frac{a_{KL}^2 qv}{4\pi\omega_0^2\Delta_j}\ , \tag{5.12}$$

Δ_j is the UA $1s\sigma\rightarrow j$ transition energy, a_{KL} is the lower-Z K-shell radius (Z_L^{-1} in atomic units), ω_0 is the UA $K\alpha$ transition frequency, and $\zeta=Z_H/Z_L$. The quantities are arranged so that I_{zj} and I_{0j} are dimensionless numbers, and are approximately independent of q and ζ to facilitate interpolation. The two-collision MO x-ray cross section is obtained by multiplying $d\sigma_z/dE_x$ and $d\sigma_0/dE_x$ by the number of $1s\sigma$ vacancies, Eq. (3.48):

$$\frac{d^2\sigma}{d\Omega\,dE_x}=\frac{n_2 vW\sigma_{px}}{\lambda_x}\frac{d\sigma_0}{dE_x}[1-A_0P_2(\cos\theta)]\ ,$$

$$A_0=\frac{3\,d\sigma_z-d\sigma_0}{2\,d\sigma_0}\ . \tag{5.13}$$

Introduction of the full electron-slip model and Coulomb trajectories for the time integral does not affect the validity of these scaling law equations significantly.

The implication of this scaling law is that if the anisotropy peak lies at a given reduced x-ray energy ν for one combination of Z_1 and Z_2, it will be at the same ν value for another combination, as long as q and ζ are kept nearly constant (and as long as the scaling law is valid). Furthermore, since MO x-ray intensities are relatively insensitive to the values of ζ and q, one can probably compare anisotropy spectra with different ζ and q values. This is a partial theoretical confirmation of the suggestion by Stoller *et al.* (1977) that spectroscopic information can be obtained from MO x-ray anisotropy spectra. They showed that the point of inflection on the anisotropy curve is related to the UA $K\alpha$ energy. Since the scaling law shows that the anisotropy peak shape is independent of ν, any point along the curve is related to the UA $K\alpha$ energy ω_0. Most of the data shown in Fig. 36 have $\zeta=1$,

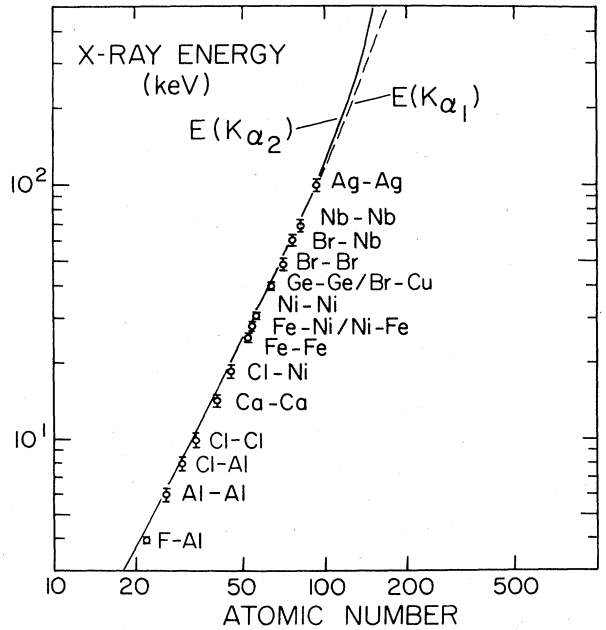

FIG. 36. A plot of the position of the point of inflection on the MO x-ray anisotropy spectrum against united-atom number Z_u. The solid and the dashed curves indicate the united-atom $K\alpha_2$ and $K\alpha_1$ transition energies (Stoller *et al.*, 1977).

but q values between approximately 3 (1-MeV/amu Al + Al collisions) and 18 (60-MeV Ag + Ag collisions) were used. Stoller *et al.* (1977) showed experimentally that the peak shape is independent of ion velocity or q over a limited range of q values (6—11 in 14- to 40-MeV Fe + Fe collisions), hence assumed it to be independent of velocity everywhere, and did not report corresponding ion velocities for their data points. However, a velocity or q dependence of the anisotropy spectrum shape is sometimes seen especially for high q values [compare 12.6-MeV ($q \approx 14$) and 92-MeV ($q \approx 5.3$) Ni + Ni collisions in Fig. 35].

The possibility of extrapolating the results in Fig. 36 to obtain UA $K\alpha$ energies in superheavy quasimolecules (e.g., Pb + Pb collisions) was challenged on the basis that the scaling law breaks down for high-Z_u collisions (Anholt, 1979a) and that the $1s\sigma$ MO x-ray anisotropy will be near zero in such collisions anyway (Anholt, 1978a). The scaling-law relations require that the ratio of each transition energy to the characteristic energy ω_0, $\nu_{1s\sigma}(\rho) - \nu_j(\rho)$ in Eq. (5.11), be independent of Z_L and Z_H for a constant reduced internuclear distance. A sketch of reduced $1s\sigma \rightarrow 2p\pi$ transition energies for several quasimolecules is shown in Fig. 37. The scaling law is valid for $Z_u < 100$, but breaks down significantly for Pb + Pb and U + U collisions. The rapid decline in the transition energy near $\rho \approx 0$ for the very high-Z_u quasimolecules is due to the overwhelming relativistic effects in the superheavy UA's, which is what makes the measurement of these transition energies potentially interesting. A similar argument was given for the breakdown of scaling laws governing $2p\sigma$ MO x-ray production (Anholt, 1979a).

In typical measurements of MO x-ray anisotropies, the maximum value of the anisotropies tends to fall off with increasing Z_u; values of $\eta = 1.4$ are seen in 20-MeV Al + Al collisions, but values of $\eta = 0.3$ are seen in 62-MeV Ag + Ag collisions (Wöfli, Morenzoni, Stoller, Bonani, and Stöckli, 1978). In part, this is due to higher electron populations in the $2p\sigma$, $2p\pi$, $3p\sigma$, and $3p\pi$ MO's in high-Z_u collisions, it being more difficult to excite more tightly bound electrons at the relatively smaller projectile velocities. Also, for very high Z_u, the $3p\pi$ electrons can form MO's, which they cannot in the low-Z_u collisions.

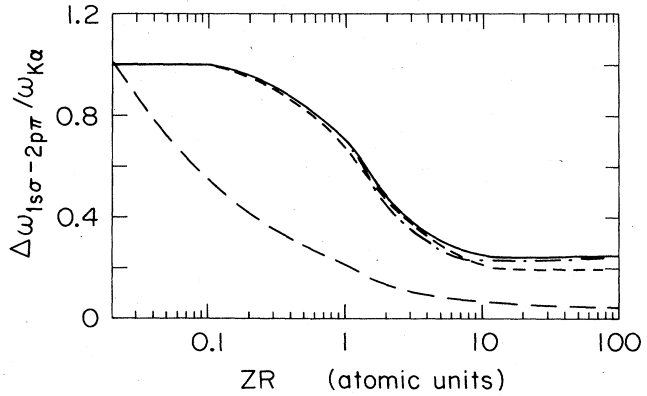

FIG. 37. The $1s\sigma$-$2p\pi$ transition energy normalized to the UA $K\alpha_1$ energy, plotted against the scaled internuclear distance. Solid line, $H^+ + H$ calculations; short-dashed line, Xe+Xe collisions, sketched from measured UA and SA binding energies; dot-dashed curve, Ne + Ne collisions, from VSM calculations (Eichler and Wille, 1974); long-dashed curve, U + U from Dirac two-center calculations (Müller and Greiner, 1976).

A more fundamental limitation is due to the enormous $2p\frac{1}{2}$-$2p\frac{3}{2}$ spin-orbit splitting in high-Z_u collisions. Because of this splitting, the MO's tend to have good j and m_j quantum numbers instead of l-s quantum numbers. A $2p\sigma$ MO is a $2p\frac{1}{2}$ orbital in high-Z_u collisions. For $2p\frac{1}{2} \rightarrow 1s\frac{1}{2}$ transitions, Δm_j values of 0 and ± 1 are allowed, and since the intensities from $\Delta m_j = \pm 1$ transitions are equal to those from $\Delta m_j = 0$ transitions, the MO radiation is emitted isotropically, independent of the orientation of the internuclear axis. Varying the $p\frac{1}{2}$ and $p\frac{3}{2}$ occupation numbers has no affect on the MO anisotropy. A nonzero anisotropy can be obtained only by affecting the relative m_j populations. Stoller *et al.* (1980) measured a near-zero MO x-ray anisotropy in Pb + Pb collisions, in agreement with these predictions.

D. One-collision molecular-orbital x-ray anisotropies

Most measurements and calculations of the anisotropy of $1s\sigma$ MO x rays are for two-collision MO x-ray production. It was suggested (Anholt, 1978a) that the anisotropies for one- and two-collision MO x-ray production should be similar. Coriolis coupling between the $p\sigma$ and $p\pi$ MO's is present in both cases. However, it is likely that fewer projectile vacancies are brought into the collision when one-collision MO x rays are made, since it is unnecessary for the projectile to have previously suffered a relatively central K-vacancy producing collision. Therefore, one-collision anisotropies may be smaller than two-collision ones.

Stoller *et al.* (1981) compared MO x-ray anisotropy spectra in gas Cl + Ar and solid Cl + KCl collisions (Fig. 38). In the gas target, only one-collision MO x rays are present, but in the solid target, one- and two-collision x rays are present, the relative contributions still being a subject of controversy (Schmidt-Böcking *et al.*, 1978a,1978b; Stoller *et al.*, 1981). A clear difference in the magnitudes and the shapes of the anisotropy spectra is seen. The anisotropy shape seen in Cl + KCl collisions is typical of that seen in most measurements. Within the experimental uncertainties, the gas-target and solid-target anisotropy spectra are nearly identical at 57 MeV; the gas anisotropies are smaller, but have similar shapes at 29 and 42 MeV, but the shapes are qualitatively different at 19 MeV. Lacking a one-collision theory of $1s\sigma$ MO x-ray production, the reason for these differences can not be ascertained. Making similar measurements with other gas targets may be useful.

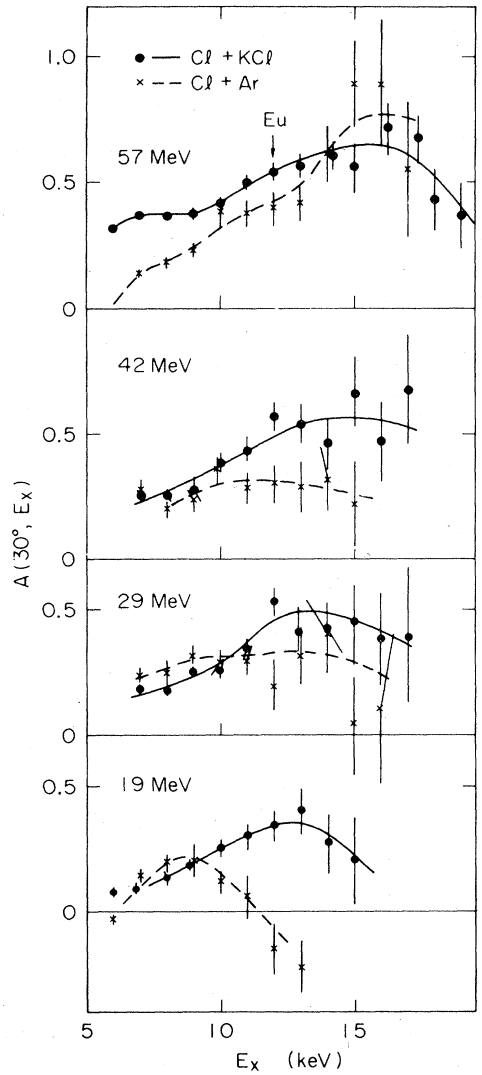

FIG. 38. Gas-target (Cl + Ar; dashed lines) and solid-target (Cl + KCl; solid lines) anisotropy spectra for 19- to 57-MeV Cl bombardments (Stoller *et al.*, 1981). The lines are drawn to guide the eye. $A(30°)+1$ is defined as the MO x-ray cross section at 90° divided by that at 30°.

E. Other theories of molecular-orbital x-ray anisotropies

1. Induced MO x-ray transitions

Müller and co-workers (Müller and Greiner, 1974; Müller, Smith, and Greiner, 1974,1975) speculated on the possibility of induced MO x-ray transitions. In the molecular frame in which the calculations of Macek and Briggs (1974) were done, an electron has, in addition to its momentum relative to the quantization axis, a rotational current. One can visualize the rotation of the electron clouds with the internuclear axis if electron slip is not present. This current gives rise to a contribution to the radiation-interaction Hamiltonian given by

$$H_{\text{rad,ind}}=\frac{e}{c}(\dot{\boldsymbol{\Theta}}\times\mathbf{r})\cdot\mathbf{A}\ , \tag{5.14}$$

where $\dot{\boldsymbol{\Theta}}$ is the rotational velocity and $\mathbf{A}$ is the radiation field. This contribution adds incoherently to the normal radiative Hamiltonian $e/mc(\mathbf{p}\cdot\mathbf{A})$ used in writing Eq. (3.30). The induced-emission x rays have an angular distribution of the form

$$\frac{d\sigma_{\text{ind}}}{d\Omega\, dE_x}\sim\tfrac{1}{2}+\tfrac{1}{4}\sin^2\theta_{\text{lab}}\ , \tag{5.15}$$

and the magnitude of the induced cross section tends to peak near the UA $K\alpha$ transition energy, where the MO x rays are made in small-impact-parameter (large $\dot{\boldsymbol{\Theta}}$) collisions.

The equation for the time development of the electronic states and the photon field is given by (Gros *et al.*, 1976)

$$\left[\frac{p^2}{2m}+V(\mathbf{r},\mathbf{R}(t))-\frac{e}{mc}\mathbf{A}\cdot\mathbf{p}+H_{\text{ph}}-i\hbar\frac{\partial}{\partial t}\right]\Psi=0\ , \tag{5.16}$$

where H_{ph} is the Hamiltonian for the photon field, $\mathbf{p}$ is electronic momentum, and V is the electron-nuclear two-center potential. Formally, if one solves equations for the eigenstates φ_i of the unperturbed Hamiltonian

$$H'=\frac{p^2}{2m}+V(\mathbf{r},\mathbf{R})+\dot{\boldsymbol{\Theta}}j_y\ , \tag{5.17}$$

where (neglecting radial coupling)

$$-i\hbar\partial/\partial t\,|\,\varphi_i\rangle=-\dot{\boldsymbol{\Theta}}j_y\,|\,\varphi_i\rangle\ , \tag{5.18}$$

then when one evaluates the matrix element of the radiation interaction $\mathbf{A}\cdot\mathbf{p}$, one obtains the spontaneous and induced terms

$$\langle\varphi_f\,|\,\mathbf{p}/m\,|\,\varphi_i\rangle=\langle\varphi_f\,|\,\omega_{fi}\mathbf{r}+\dot{\boldsymbol{\Theta}}\times\mathbf{r}\,|\,\varphi_i\rangle\ . \tag{5.19}$$

The problem with this approach is that the φ basis is an inconvenient one for making MO x-ray calculations (Gros *et al.*, 1977). The difference between the eigenenergies of φ_i and φ_f is not simply the difference between the energies obtained from correlation diagrams, but also includes terms dependent on $\dot{\boldsymbol{\Theta}}$. Also, the $\mathbf{A}$ field is much more complicated in this frame (Däppen and Baltensperger, 1977).

The approach taken in Sec. III.C is to write the total wave function as a linear combination of basis wave functions χ_i, which are eigenfunctions of

$$H_0=\frac{p^2}{2m}+V(\mathbf{r},\mathbf{R})\ . \tag{5.20}$$

Then when one takes matrix elements of $\mathbf{p}\cdot\mathbf{A}$, the commutator $[p,H_0]$ produces no induced radiation term proportional to $\dot{\boldsymbol{\Theta}}$. The rotational velocity is taken into account in the time dependence of the σ-π mixing coefficients.

Chen *et al.* (1975) suggested the inclusion of an induced transition term due to radial coupling of the form

$$H' = \frac{e}{c}(\dot{R}/R)\mathbf{r}\cdot\mathbf{A} \ . \tag{5.21}$$

These terms could produce large contributions near avoided crossings. By approximating the basis wave functions by diabatic wave functions, which could be viewed as linear combinations of adiabatic functions obtained by solving equations for the mixing amplitude involving terms in $\dot{R}$, there is no need to take into account radial coupling, either in the radiation Hamiltonian or in the calculation of the mixing amplitudes. Terms of this sort can induce quasimolecular bremsstrahlung, however (Anholt and Salin, 1977).

It is interesting to reflect that calculations with the induced radiation Hamiltonian produced results similar to those obtained with the full electron-slip theories. Alignment of the MO's for x-ray energies near the UA energy was predicted, and it was realized that vacancies in the $2p\sigma$ and $2p\pi$ MO's were required to produce the observed anisotropies in Ni + Ni collisions. The vacancy populations taken were somewhat unrealistic, because the importance of the $3p\sigma$ and $3p\pi$ MO's, where higher vacancy populations could be obtained, was not realized. However, many results based on these theories, e.g., the claim to have observed induced transitions in the velocity dependence of the MO x-ray cross section (Betz *et al.*, 1975), should be reinterpreted.

2. Radiative electron capture to molecular orbitals (RECMO)

It is possible for the outer-shell electrons not participating in MO formation in the collision (e.g., the absent $3p\pi$ electrons in Ni + Ni collisions) nevertheless to participate in MO x-ray production. Radiative transitions between target atomic orbitals (AO's) and projectile AO's are known as REC. Transitions between two MO's are MO x rays. Transitions from outer-shell AO's to MO's can be called RECMO transitions (Wölfli, Stoller, Bonani, Stöckli, Suter, and Däppen, 1978).

RECMO transitions may be responsible for continuum x rays seen in high-velocity measurements (Thoe *et al.*, 1975; Wölfli, Stoller, Bonani, Stöckli, Suter, and Däppen, 1978) where even the $2p\sigma$ or $2p\pi$ MO's cannot form. The angular distribution of RECMO x rays is expected to be of the form

$$\frac{d\sigma_{\text{RECMO}}}{d\Omega\, dE_x} \sim A + B\sin^2\theta \ , \tag{5.22}$$

as a consequence of the velocity dependence of the AO translation factors of the form $\exp(i\mathbf{v}\cdot\mathbf{r} - iv^2t/2)$.

In relatively low-velocity collisions like 90-MeV Ni + Ni collisions, contributions from RECMO are negligible. The transition matrix element depends on the overlap between the small $1s\sigma$ MO and the diffuse outer-shell AO's. Anholt (1979c) has calculated these overlap integrals for the nonadiabatic orbitals in Ni + Ni collisions, and obtained RECMO intensities 10^{-3} to 10^{-1} smaller than the observed intensities. In high-velocity collisions, where the $2p\sigma$ and $2p\pi$ MO's are not formed and MO x-ray transitions are not possible, the smaller AO-MO overlap is a less important consideration, so the observed continuum x-ray intensity in those measurements could be due to RECMO transitions. The theory of RECMO transitions could explain the high positive anisotropies seen by Wölfli *et al.* (Wölfli, Stoller, Bonani, Stöckli, Suter, and Däppen, 1978) in 0.2- to 2-MeV/amu F + Al, Al + Al, and Cl + Al collisions, but it fails to explain the near-zero anisotropies seen by Thoe *et al.* (1975) in ~2-MeV/amu C + C collisions.

3. The kinematic dipole model

Hartung and co-workers (Hartung and Fricke, 1978; Hartung *et al.*, 1979) made calculations of MO x-ray anisotropies in Xe + Ag and in I + Au collisions. The basis of their calculations is a version of the quasistatic model of MO x-ray production and assumes that the σ and π MO's rotate with the internuclear axis during the collision. For a given x-ray energy E_x and a given transition $i \rightarrow f$, one obtains the corresponding internuclear distance R where $\Delta E_{if}(R) = E_x$. Then, for every impact parameter, one calculates the angle between **R**, **v**, and the photon direction **k**. For σ-σ transitions, the angular distribution is proportional to $\sin^2\theta(\mathbf{R},\mathbf{k})$, where θ is the angle between **R** and **k**. For σ-π transitions, the angular distribution is proportional to $1+\cos^2\theta(\mathbf{R},\mathbf{k})$. One then finds the number of photons emitted at the angle θ_{lab} between **v** and **k**, weights it by the probability of having the impact parameter b and the transition probability λ_{if}, and sums over impact parameters, possible transitions, and the two points along the trajectory where the distance R is reached. RHFS correlation diagrams are used to calculate the transition energies ΔE_{if}. The transition rates λ_{if} are not calculated, but are taken to be proportional to $(\Delta E_{if})^3$. Several critical remarks on this model have already been made in Sec. IV.F. This model gives anisotropies that are in reasonable agreement with experiment in some cases (Hartung *et al.*, 1979). However, the dynamic calculations show that the MO's contributing to $1s\sigma$ MO x-ray production tend not to rotate during the collision.

F. $2p\sigma$ molecular-orbital x-ray anisotropies

The anisotropy spectra for $2p\sigma$ MO x rays have been measured in a number of collisions ranging from Fe + Fe to Ag + Ag (Frank *et al.*, 1976; Vincent, 1977; Stoller *et al.*, 1978). Also, $2p\sigma$ anisotropies may have been measured by Stoller *et al.* (1980) in Pb + Pb collisions, though the interpretation there is ambiguous. The anisotropy spectrum shows a peak whose position can be related to either the UA $L\beta$ ($2p\frac{1}{2}$-$3d\frac{3}{2}$) transition energy ω_0, using (Anholt, 1979a)

$$E_{\text{peak}}=2.34\omega_0\ , \tag{5.23}$$

for constant $q=\omega_0 a_{KL}/v=2$, or to the SA K binding energy E_K (Stoller *et al.*, 1978)

$$E_{\text{peak}}=1.5\pm0.04E_K\ . \tag{5.24}$$

The experimental evidence of Stoller *et al.* is a positive indication that the observed continua are due to MO x-ray production, instead of REC for instance.

Stoller *et al.* (1978) interpret the peak position in terms of the maximum $2p\sigma$ binding energy at intermediate internuclear distances. That E_{peak} is nearly equal to the $2p\sigma$ binding energy computed from correlation diagrams, and not, for example, to the $3d\sigma,\pi\rightarrow 2p\sigma$ transition energy, suggested the conclusion that RECMO transitions, where the initial state AO's have near-zero binding energy, are responsible for production of $2p\sigma$ MO x rays.

Anholt (1979a) has calculated $2p\sigma$ MO x-ray anisotropies in 35- to 75-MeV Nb + Nb collisions using the full electron-slip theory described in Secs. III.C and IV.D. The principal transitions involved are $3d$ to $2p$ transitions (Fig. 10). One must account for the Coriolis coupling between the $3d\sigma$, $3d\pi$, and $3d\delta$ MO's, as well as between the $2p\sigma$ and $2p\pi$ MO's. The results are compared with measurements by Vincent (1977) in Fig. 39. The calculations predict a peak in the anisotropy spectrum, at the correct position. Near the anisotropy maximum ($\sim$30 keV), a significant number of the continuum x rays are due to $1s\sigma$ MO x rays (see Fig. 12). The total anisotropy is found by adding the calculated $2p\sigma$ and extrapolated $1s\sigma$ MO x-ray intensities. The $1s\sigma$ MO x-ray anisotropy is assumed here to be constant for $E_x<50$ keV, which gives a total anisotropy in good agreement with experiment.

Several conclusions emerge from the calculations of Anholt (1979a). First, one does not need to assume the presence of RECMO transitions to explain the observed anisotropy spectra; $3d\rightarrow 2p$ MO transitions alone give good agreement with experiment. Second, the anisotropy peak position is relatively insensitive to the occupation of the $3d$ and $4d$ MO's. The transition most responsible for the anisotropy peak is the $3\Sigma\rightarrow 2\Pi_x$ transition. The calculations in Fig. 39 were made assuming that only the 3Σ and 3Π MO's are filled, as suggested by the adiabaticity criteria based on the binding energies of SA orbitals correlating to the $3d\delta$ and $4d$ MO's. The possible inclusion of the latter MO's lowers the value of the anisotropy maximum, but does not shift the peak position. Finally, one can derive a scaling law, predicting a universal anisotropy spectrum shape as a function of the reduced energy $\nu=\omega/\omega_0$ for a constant value of $q=\omega_0 a_{KL}/v$ and $\zeta=Z_H/Z_L$. If hydrogenic correlation diagrams are valid

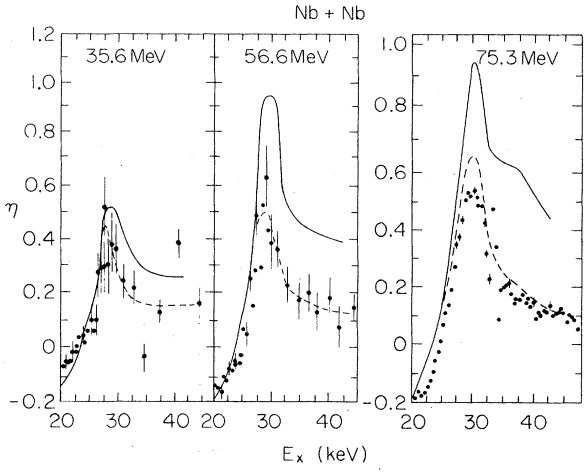

FIG. 39. Measured (Vincent, 1977) and calculated anisotropies in 35.9-, 56.6-, and 75.3-MeV Nb + Nb collisions. The solid lines show the calculated $2p\sigma$ MO x-ray anisotropy, and the dashed lines were calculated including contributions to the total intensity from $1s\sigma$ MO x rays (Anholt, 1979a).

(screening and relativistic effects are negligible), ω_0 can be any quantity depending on Z_1+Z_2, Z_1, or Z_2: the UA $L\beta$ transition energy, the UA $2p$ binding energy, or the maximum $3d$-$2p$ transition energy at intermediate internuclear distances. Of course, hydrogenic correlation diagrams are exactly valid only for one-electron low-Z_u collisions, though they are approximately valid in collisions between Fe + Fe and Ag + Ag, and are best for Nb + Nb collisions (Anholt, 1979a). Since the observed $2p\sigma$ MO x rays are emitted at internuclear distances where the $3d$-$2p$ transition energy is largest, this choice for ω_0 would be best if it were simple to calculate. Because it is not, Anholt (1979a) scaled calculations based on the UA $L\beta$ energy. The scaling law stipulates that identical peak positions are obtained only if identical reduced velocities q and asymmetry parameters ζ are used. This was not done in the measurements in Stoller *et al.* (1978), though the dependence on q is slight. The scaling law is expected to be invalid in superheavy quasimolecules, making spectroscopic applications impractical.

The origin of the $2p\sigma$ anisotropy peak, though correctly predicted by a large computer code, is difficult to understand on simple physical principles. The perfect electron-slip model fails for $2p\sigma$ MO x-ray production, because of the large difference between the $2p\sigma$ and $2p\pi$ electron binding energies. When the coupled equations are analyzed in terms of their basic components, terms like

$$\int_{-\infty}^{\infty} dt\, a_{\sigma i}(t)b_{fj}(t)\begin{bmatrix}\cos\Theta\\ \sin\Theta\end{bmatrix}D_{\sigma j}[R(t)]\exp\left[i\int_0^t[\omega-\omega_{2p\sigma}(t')+\omega_j(t')]dt'\right] \tag{5.25}$$

overwhelm terms containing $\omega_{2p\pi}(t')$. Considering only $3\Sigma\rightarrow 2\Pi_x$ transitions, which give the major contribution to the anisotropy peak, we get

$$D_{z\Pi x\Sigma} \sim \int_{-\infty}^{\infty} dt\, a_{\sigma\Pi x}(t)(2\cos\Theta b_{\sigma\Sigma}(t) - \sqrt{3}\sin\Theta b_{\pi x\Sigma}) D_{\sigma\sigma} ,$$

$$D_{x\Pi x\Sigma} \sim \int_{-\infty}^{\infty} dt\, a_{\sigma\Pi x}(t)(-2\sin\Theta b_{\sigma\Sigma}(t) - \sqrt{3}\cos\Theta b_{\pi x\Sigma}) D_{\sigma\sigma} ,$$

and

$$D_{y\Pi x\Sigma} = 0 \tag{5.26}$$

where we have abbreviated

$$D_{\sigma\sigma} = D_{2p\sigma\text{-}3d\sigma}[R(t)] \exp\left[i \int_0^t (\omega - \omega_{2p\sigma} + \omega_{3d\sigma}) dt' \right] , \tag{5.27}$$

which is approximately equal to the analogous term involving the $3d\pi$ orbital, as shown in Fig. 9 of Anholt (1979a). The highest-energy radiation comes from near the internuclear distance, where ω is closest to the maximum $2p\sigma \rightarrow 3d\sigma$ or $2p\sigma \rightarrow 3d\pi$ transition energy difference, at $Z_L R = 4$ a.u. At this point $a_{\sigma\Pi x}$ (which is near zero for $t < 0$), is close to its final value, so we take it outside the integral, and we only consider the contribution to the time integral for $t > 0$. The b amplitudes reach their final values more slowly, so we substitute kinematic peak solutions [Anholt, 1979a, Eqs. (A.12)] for them and obtain

$$\begin{aligned} D_z &\sim a_\sigma(b) \int_{-\infty}^{\infty} dt\, D_{\sigma\sigma} 2\cos\Theta(t) , \\ D_x &\sim a_\sigma(b) \int_{-\infty}^{\infty} dt\, D_{\sigma\sigma} \sin\Theta(t) , \\ D_y &= 0 . \end{aligned} \tag{5.28}$$

We next remove the value of $\cos\Theta$ and $\sin\Theta$ from inside the integral, substituting the value at the internuclear distance R, where radiation is emitted [$\cos\Theta(R) = (R^2 - b^2)^{1/2}/R$, for positive t]. We obtain finally

$$\begin{aligned} A_0 &= \frac{3|D_z|^2 - |D_z|^2 - |D_x|^2}{2(|D_x|^2 + |D_z|^2)} \\ &= \frac{9(1 - b^2/R^2) - 1}{6(1 - b^2/R^2) + 2} . \end{aligned} \tag{5.29}$$

The variation of $A_0(b)$ for the $3\Sigma \rightarrow 2\Pi_x$ transitions shown in Fig. 40 can be understood from this equation. The relevant internuclear distance $Z_L R$ is approximately equal to ~ 4 a.u., but for 30-keV $2p\sigma$ MO x rays in Nb + Nb collisions, impact parameters up to $Z_L b \sim 1.5$ a.u. contribute, so that A_0 is approximately unity, independent of b for $0.2 < Z_L b < 1.5$ [Fig. 40(b)].

For smaller x-ray energies, larger b values contribute to the total cross section, where A_0 is smaller ($A_0 \rightarrow -\frac{1}{2}$ at $b = R$). The A_0 value for the total cross section therefore falls off at lower x-ray energies [Fig. 40(a)]. At higher x-ray energies, the range of impact parameters is so small that the contributions to the cross section come from the region of $Z_L b$ (< 0.2 a.u.), where the perfect electron-slip model is valid, giving $A_0 = -\frac{1}{2}$. Hence A_0 decreases with x-ray energy above 30 keV.

This argument has little to do with the maximum value of the relevant $2p\sigma$-$3d$ transition energy, 20—22 keV. For x-ray energies near 30 keV, the required momentum transfer needed to make these x rays [$\Delta|\mathbf{K}| = (8\text{- to }10\text{-keV})/v$] limits the contributing range of impact parameters to $\Delta b < |\Delta \mathbf{K}|^{-1} \approx 1$ a.u./Z_L (Bang and Hansteen, 1959), which in turn affects the expected orientation of the transition dipole at the emission distance. The exact peak position is determined by a complicated interplay between dipole orientation considerations, electron-slip considerations, and the range of impact parameters involved at given x-ray energy.

G. *L* and *M* molecular-orbital x-ray anisotropies

Folkmann *et al.* (1976) and Kraft *et al.* (1974) measured the angular distribution of 6- to 9-keV continuum x rays in 6.3- to 45-MeV I + Au collisions (Fig. 41). The anisotropy spectrum is peaked, and the peak position and shape vary strongly with the projectile velocity. Realistic calculations of the anisotropies have not yet been made, although qualitative explanations based on the model of rotationally induced transitions have been suggested (Kraft *et al.*, 1974). Also, kinematic dipole approximation calculations in reasonable agreement with experiment have been made by Hartung *et al.* (1979). Most of the models are based on the assumption that transitions to the $3d\frac{3}{2}$ MO are observed in these collisions.

Wölfli *et al.* (Wölfli, Morenzoni, Stoller, Bonani, and

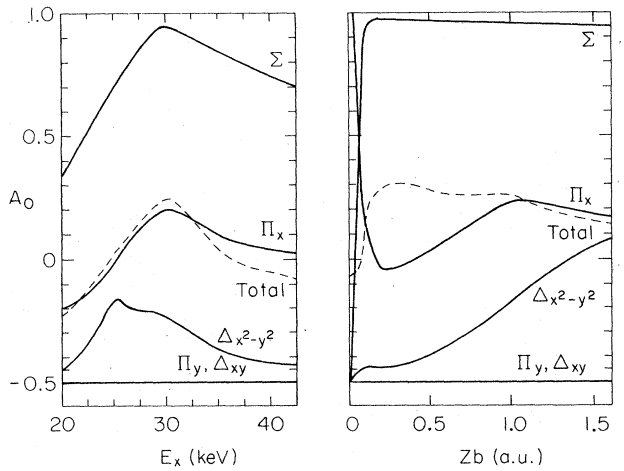

FIG. 40. A_0 parameters for individual transitions for $2p\sigma$ MO x-ray production in 56.6-MeV Nb + Nb collisions vs x-ray energy. On the left-hand side, the total (integrated over impact parameter) A_0 parameters are plotted against x-ray energy, and on the right, A_0 parameters for a fixed x-ray energy, 30 keV, are plotted against impact parameter. The A_0 parameter for the $2\Pi_x$-3Σ transition is abbreviated Σ, and so on (Anholt, 1979a). The total A_0 parameter, assuming equal occupations of all MO's, is shown by the dashed line.

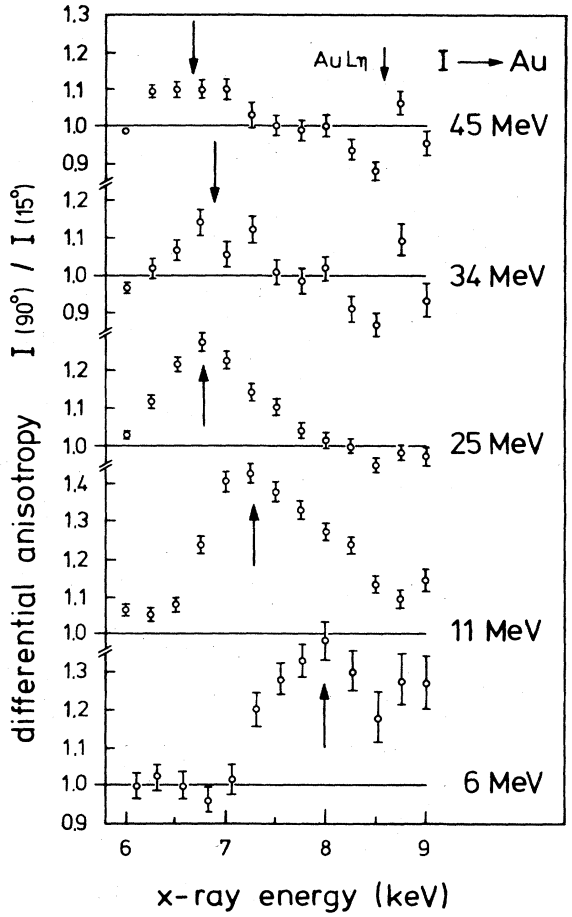

FIG. 41. Differential anisotropies in I+Au collisions I(90°)/I(15°) for x-ray energies between 5.4 and 9.4 keV and impact energies between 6 and 45 MeV. The data points are corrected for Doppler effects using the center-of-mass velocity (Folkmann *et al.*, 1976).

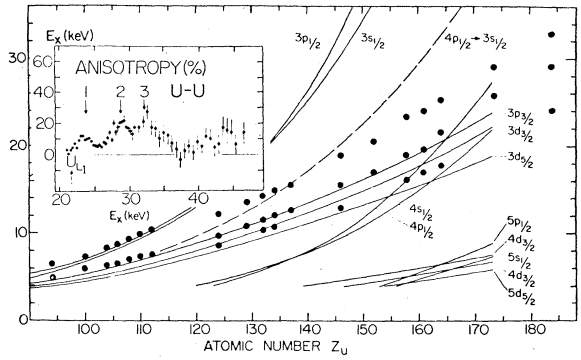

FIG. 42. Plots of three anisotropy peak energies against Z_u. For $Z_u \leq 112$ and for a few very asymmetric collisions, only two peaks could be resolved. For comparison, the relevant M, N, and O UA binding energies (solid lines) and one typical united-atom M-N transition energy (dashed-line) are shown. The accuracy of the peak energies corresponds to the size of the symbols. The inset shows a typical anisotropy spectrum, found in the 40-MeV U + U collisions, above the uranium L x-ray peaks (Wölfli, Morenzoni, Stoller, Bonani, and Stöckli, 1978).

Stöckli, 1978) measured anisotropies of ~5- to 30-keV continuum x rays for near-symmetric collisions ranging from Ag + Ag to U + U, as shown in Fig. 42. In Ag + Ag and I + Sn collisions, these x rays are probably due to transitions to vacancies in the $3d\sigma$ MO (Sec. IV.E). Several peaks in the anisotropy spectra are seen which scale with the UA atomic number as one varies Z_1 and Z_2. Wölfli *et al.* associated the peak positions with specific UA transition energies or binding energies. Morenzoni *et al.* (1982) interpreted the peak positions in Au + Au collisions in terms of MO x-ray transitions into several different MO's. They observed the disappearance of some peaks at low velocities, consistent with expected thresholds for vacancy production via radial or rotational coupling mechanisms.

Measurements of this kind would provide a stringent test of as yet undeveloped theories of MO x-ray production in these collisions. Peaked anisotropy spectra for $1s\sigma$ and $2p\sigma$ MO x rays have been seen. In both cases the peak position scales with UA atomic numbers or transition energies, but the peak position is due to a number of complicated factors. The deduction of UA quantities from anisotropy peak positions can only be made after precise dynamical calculations are done. By using intensity and anisotropy information, such calculations can undoubtedly decide whether the MO x rays seen in I + Au collisions are $3d\pi$ or $4f\sigma$ MO x rays, and whether the x rays seen by Wölfli *et al.* (Wölfli, Morenzoni, Stoller, Bonani, and Stöckli, 1978) and Morenzoni *et al.* (1982) are $3d\sigma$ or $2p\pi$ ones.

VI. OTHER MEASUREMENTS

A. The impact-parameter dependence of molecular-orbital x-ray production

1. Quasimolecular interferences

More rigorous tests of theories of MO x-ray production are obtained if one measures the impact-parameter dependence of MO x-ray emission, $\sim\sum |\mathbf{D}_{ij}(\omega,b)|^2$ in Eq. (3.35), instead of cross sections. Such measurements are done by counting coincidences between continuum x rays and particles scattered to an angle Θ classically related to the impact parameter (as long as nuclear reactions do not occur). The MO x-ray emission probability, $d^2P/d\omega\, d\Omega$, is proportional to the number of coincidences $N_c(\omega,\theta)$ divided by the number of scattered particles N_p

$$\frac{d^2P(b,\omega,\theta)}{d\omega\, d\Omega} = \frac{N_c(\omega,\theta)}{N_p[\Theta(b)]}\frac{AaD}{\varepsilon\, d\Omega_x}, \tag{6.1}$$

where the remaining quantities are the same as those given in Eq. (4.2).

One of the most interesting aspects of MO x-ray emis-

sion is the predicted oscillatory behavior of the emission probability with x-ray energy for fixed impact parameter, due to the interference between x rays emitted on the incoming and outgoing parts of the ion trajectory (Lichten, 1974; Macek and Briggs, 1974). As discussed in Sec. III.B.2, this interference occurs for $1s\sigma$ MO x rays in very low-velocity collisions. It is not seen for one-collision MO x-ray production, but is seen only if a vacancy is brought into the collision. Unfortunately, if the vacancy is made in a two-collision process in solid targets, the scattering angle dependence for the initial vacancy production process smears the observed MO x-ray production probability, making the observation of oscillations impossible (Anholt, 1982a). The observation is possible only if one uses a fully stripped projectile, which is incompatible with the MO formation criterion, $v \ll v_K$.

This obstacle has been overcome by using an acceleration-deceleration technique for producing low-velocity, fully stripped projectiles (Tserruya *et al.*, 1983; Schuch *et al.*, 1985). A Cl projectile is accelerated to a high energy where v is greater than v_K, then is stripped to one electron. It then is decelerated to a low velocity where MO interference is possible. The projectile then impinges on a dilute gas target where single collisions prevail, so it cannot recapture electrons easily.

Figure 43 shows measured ionization probabilities in 5- to 20-MeV $Cl^{16+}+Ar$ collisions. For the higher-energy projectiles, the oscillatory structure is less obvious, but for low-velocity, low-b collisions, reasonable agreement between the shape of the measured oscillatory impact-parameter dependence and the electron-slip calculations of Anholt (1978a) is obtained. The disagreement between the magnitudes of measured and calculated cross sections was thought to be due to the inaccuracy of calculated MO energy levels. The calculations shown in Fig. 43 are based on the scaling law discussed in Secs. IV.C and V.C, where the x-ray energy scale is determined using the many-electron UA $K\alpha$ energy. The shapes of the measured and calculated impact-parameter dependences agree well, so we cannot attempt to adjust the magnitude of the probabilities by adjusting the MO energy levels. The origin of the quantitative disagreement is presently unknown.

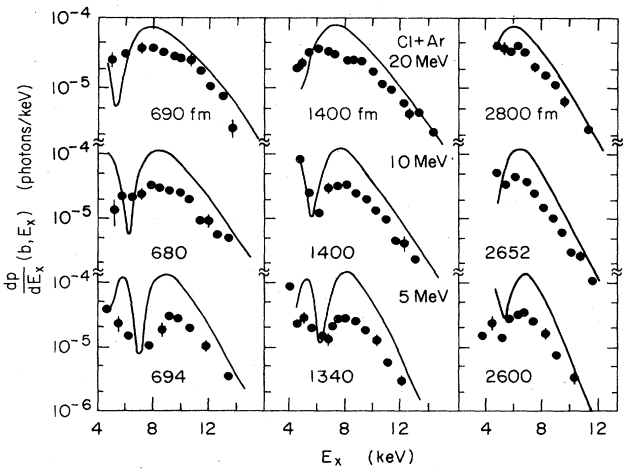

FIG. 43. The impact-parameter dependence of $1s\sigma$ MO x rays in 5- to 20-MeV Cl + Ar collisions, where one-electron Cl projectiles bring in a K vacancy. The oscillatory dependence is due to the interference between MO x-ray emission on the incoming and outgoing parts of the collisions. The solid lines show full electron-slip calculations. (The data is from Schuch *et al.*, 1985.)

The oscillations in the MO x-ray spectra depend sensitively upon the molecular transition energies, $E_{1s\sigma\text{-}2p\sigma}(R)$ or $E_{1s\sigma\text{-}2p\pi}(R)$ for Cl + Ar collisions. Schuch *et al.* (1985) and Meron *et al.* (1985) analyzed the spectra, obtaining from the oscillation frequency an R-dependent transition energy, which has been compared with RHFS calculations (Fricke *et al.*, 1984). Because the $1s\sigma$-$2p\sigma$ and the $1s\sigma$-$2p\pi$ transitions both contribute coherently to the total MO x-ray production probability, it is unclear what the experimentally derived transition energy represents. The $2p\sigma$ and $2p\pi$ energies may be sufficiently close together at the relevant internuclear distances that this difference is insignificant.

Two other indications of quasimolecular interferences besides that discussed in this section have not been verified. Reported oscillations in the MO x-ray anisotropy spectrum (Wölfli *et al.*, 1976) have not been confirmed, despite numerous attempts (Stöckli, 1979). Smith *et al.* (Smith, Müller, Greiner, Greenberg, and Davis, 1975) interpreted some small oscillations superimposed on the $1s\sigma$ MO x-ray continuum seen in 70-MeV Ni+Ni collisions as quasimolecular interferences, but these peaks were later found to be due to one-photon, two-electron SA x-ray transitions (Wölfli *et al.*, 1975).

2. Solid-target measurements

The two-collision MO x-ray cross section [Eq. (3.48)] is proportional to the cross section for projectile K-vacancy production, say σ_1, and that for MO x-ray production given a $1s\sigma$ vacancy, say σ_2. In a double collision, the projectile suffers a deflection during the creation of a K vacancy in the azimuthal angle φ_1 and the polar angle Θ_1, related to impact parameter b_1, then suffers a second deflection φ_2 and Θ_2 when the MO x ray is emitted. In the laboratory, one measures a deflection Θ_0 given by the addition of the angles Θ_1, Θ_2, φ_1, and φ_2 according to

$$\cos\Theta_0=\cos\Theta_1\cos\Theta_2-\sin\Theta_1\sin\Theta_2\cos\varphi_2 \ . \tag{6.2}$$

To compare calculated MO x-ray production probabilities $dP_{\mathrm{MO}}(\Theta_2)/d\omega$ with measured probabilities $dP_{\mathrm{TCMO}}(\Theta_0)/d\omega$, one must fold in all combinations of the angles Θ_1, Θ_2, and φ_2, weighted by the probabilities $P_K(\Theta_1)$ and $dP_{\mathrm{MO}}(\Theta_2)/d\omega$ that give the angle Θ_0. Anholt (1982a) made such calculations using a Monte Carlo technique. One finds that if the MO x-ray and K-vacancy production probabilities fall off approximately equally slowly with impact parameter, as they do at low x-ray energies in 90-MeV Ni + Ni collisions, the folded probability falls off more steeply than either. If one dependence falls off much faster with b than the other, as

the high MO x-ray energy probability does, the folded probability has approximately the same shape as the faster falling impact-parameter dependence.

Figure 44 compares two calculations of MO x-ray production in 90-MeV Ni + Ni collisions with measurements of Schmidt-Böcking *et al.* (1982). Calculation A is based on that of Anholt (1982a). Calculation B, by Jäger (1981), used a different method for folding the K-vacancy and MO x-ray production probabilities. Despite the fact that different approximations to the MO correlation diagrams and matrix elements were used in the two calculations, the shapes of the two calculations agree well with each other and with experiment for $b > 500$ fm. In calculation B, Jäger has included $2p\sigma$ MO x-ray production, which is certainly important near 15 keV, where Anholt's calculations are lower than experiment.

Also shown in Fig. 44 is a contribution from one-collision $1s\sigma$ MO x rays. The impact-parameter dependence of $1s\sigma$ MO x rays is presumed to vary as that for $1s\sigma$-vacancy production (Müller *et al.*, 1978):

$$P_{1s\sigma}(b) \sim \exp[-2R_{\min}E_{1s\sigma}(R_{\min})/\hbar v] , \tag{6.3}$$

where $R_{\min}$ is the internuclear distance of closest approach for an impact parameter b, and $E_{1s\sigma}$ is the $1s\sigma$ binding energy at that distance. The one-collision MO (OCMO) x-ray curves in Fig. 44 were obtained from

$$\frac{dP_{\mathrm{OCMO}}}{d\omega} = N\frac{dP_{\mathrm{MO}}(b,\omega)}{d\omega}\exp(-2R_{\min}E_{1s\sigma}/\hbar v) , \tag{6.4}$$

where N is a b-independent, x-ray-energy-independent constant approximately equal to 0.016 in both calculations, and the MO x-ray emission probability per $1s\sigma$ vacancy is obtained by summing over transitions the probability given in Eq. (3.38). Such a dependence was first proposed by Meyerhof *et al.* (1974) and criticized by Thorson and Choi (1977). Nevertheless, reasonable agreement between theory and experiment is obtained, and the value of the constant N is close to the expected value (Gaukler, 1981),

$$N \approx \tfrac{1}{2}P_{1s\sigma}(b=0) = 0.01\text{–}0.03 . \tag{6.5}$$

Several other measurements of K MO x-ray production probabilities have been made (Tserruya *et al.*, 1976; Schuch *et al.*, 1980; Stiebing *et al.*, 1984). In 143-MeV Nb + Nb collisions, Schuch *et al.* (1980) found that the impact-parameter dependence of $2p\sigma$ MO x-ray production follows that of K-vacancy production, as suggested by Anholt and Meyerhof (1977). One can take the view that $2p\sigma$ MO x rays are made by filling $2p\sigma$ vacancies on the outgoing part of the collision. If the vacancy is not filled by MO x rays (which is usually the case, given the low probabilities for MO x-ray emission), SA K x rays will result. Because of momentum-transfer considerations, the probabilities for x-ray energies much exceeding

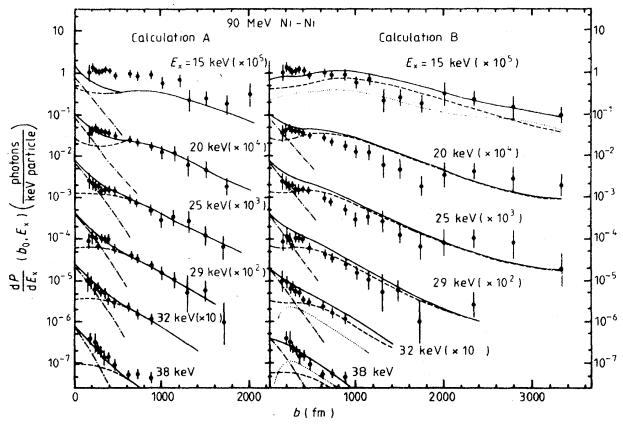

FIG. 44. Experimental and theoretical (solid curves) MO x-ray production probabilities in 90-MeV Ni + Ni collisions at several x-ray energies. The other curves show calculated contributions of two-collision $1s\sigma$ MO radiation (dashed curves), one-collision $1s\sigma$ MO radiation (dot-dashed curves), and one-collision $2p\sigma$ MO radiation (dotted curves; calculation B only).

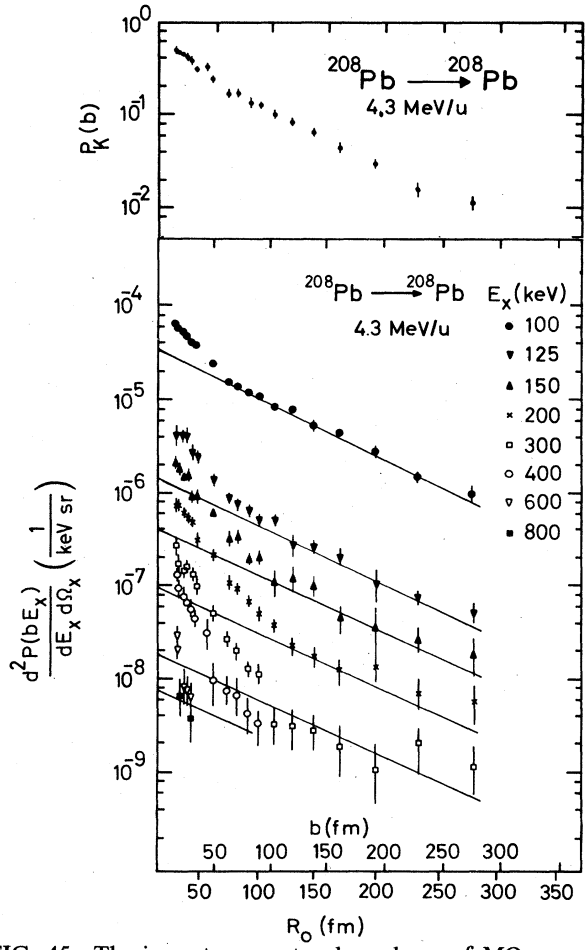

FIG. 45. The impact-parameter dependence of MO x rays in 4.3-MeV/amu ^{208}Pb+^{208}Pb collisions, showing a two-component structure (Stiebing *et al.*, 1984). Above ~100 fm, the impact-parameter dependence of the continuum x-ray production falls off as that for Pb SA K x rays produced by the excitation of electrons from the $2p\sigma$ MO (top part of the figure), and hence is thought to be due to $2p\sigma$ MO x rays. Below 100 fm, the steeply falling impact-parameter dependence is probably due to $1s\sigma$ MO x-ray production.

the maximum $2p\sigma$-$3d$ transition energy fall off slightly faster with b than the K-vacancy probability.

In 4.2-MeV/amu Pb + Pb collisions (Fig. 45, from Stiebing *et al.*, 1984), two different slopes are observed in the impact-parameter dependence. The steeply falling segment ($b < 100$ fm) is thought to be due to one-collision $1s\sigma$ MO x-ray production. The $b < 100$ fm probabilities are relatively higher at higher x-ray energies, where $1s\sigma$ MO x rays are dominant, and the impact-parameter dependence is qualitatively in agreement with that calculated by Kirsch *et al.* (1979) for $1s\sigma$ MO x rays. The slowly falling segment, which has the same shape as the K-vacancy impact-parameter dependence, is thought to be due to $2p\sigma$ ($2p\frac{1}{2}$) MO x rays.

B. The azimuthal angular distribution

Although measurements of the polar angular anisotropy of MO x rays for fixed impact parameters have not been reported, the azimuthal angular anisotropy has been measured for fixed impact parameters (Schuch *et al.*, 1981; Bürgy *et al.*, 1981). The azimuthal anisotropy was measured at a polar angle $\theta_{\rm lab}=90°$ with respect to the collision plane established by measuring coincidences with particles scattered into a direction **v**″ from the beam direction **v**. It is defined by

$$\eta_\varphi=\frac{d^2P(b,v,\theta_{\rm lab}=90°,\varphi=90°)}{d^2P(b,v,\theta_{\rm lab}=90°,\varphi=0°)}-1\ , \tag{6.6}$$

where $\varphi=0°$ is parallel to the collision plane defined by **v** and **v**″. The anisotropy is calculated using (Anholt, 1981)

$$\eta_\varphi=\frac{|D_x|^2-|D_y|^2}{|D_x|^2+|D_y|^2}\ , \tag{6.7}$$

where

$$|D_x|^2=\sum_{if}|D_{xif}(b,v,\omega)|^2\ , \tag{6.8}$$

and the components of $\mathbf{D}(b,v,\omega)$ for $1s\sigma$ MO x rays are given in Eq. (3.46). The azimuthal anisotropy provides a sensitive test of the electron-slip calculations. In the perfect electron-slip model, the x component of the intensity comes from only $\Pi_x\rightarrow 1s\sigma$ transitions, and the y component from $\Pi_y\rightarrow 1s\sigma$ transitions. Since the π_x and π_y MO's originate from identical SA orbitals and have equal binding energies, they should be equally occupied and should have equal intensities, so that near-zero azimuthal anisotropies are obtained. In other models, e.g., the kinematic dipole approximation of Hartung and coworkers (Hartung and Fricke, 1978; Hartung *et al.*, 1979), the x component comes from σ and π_x transitions, and the y component only from the π_y MO, so the x and y components tend to be unequal, and larger azimuthal anisotropies are obtained.

For two-collision MO x rays made in solid targets, the determination of the scattering plane is not straightforward. An incoming projectile of velocity **v** scatters into the direction **v**′ in the collision in which the K vacancy is made, then into the direction **v**″ in the collision in which the MO x ray is emitted. One measures the anisotropy with respect to the plane determined by **v** and **v**″, but calculates it in Eq. (6.8) with respect to the plane **v**′ and **v**″. The anisotropy with respect to the plane **v**-**v**″ must be determined by folding with the measured K-vacancy production scattering angle dependence as described by Anholt (1982a) and in Sec. VI.A.2. The calculated azimuthal anisotropy is small in the electron-slip model, and folding reduces it further. Figure 46 shows results for 90-MeV Ni + Ni collisions. The largest azimuthal anisotropy is found at the largest impact parameters, where

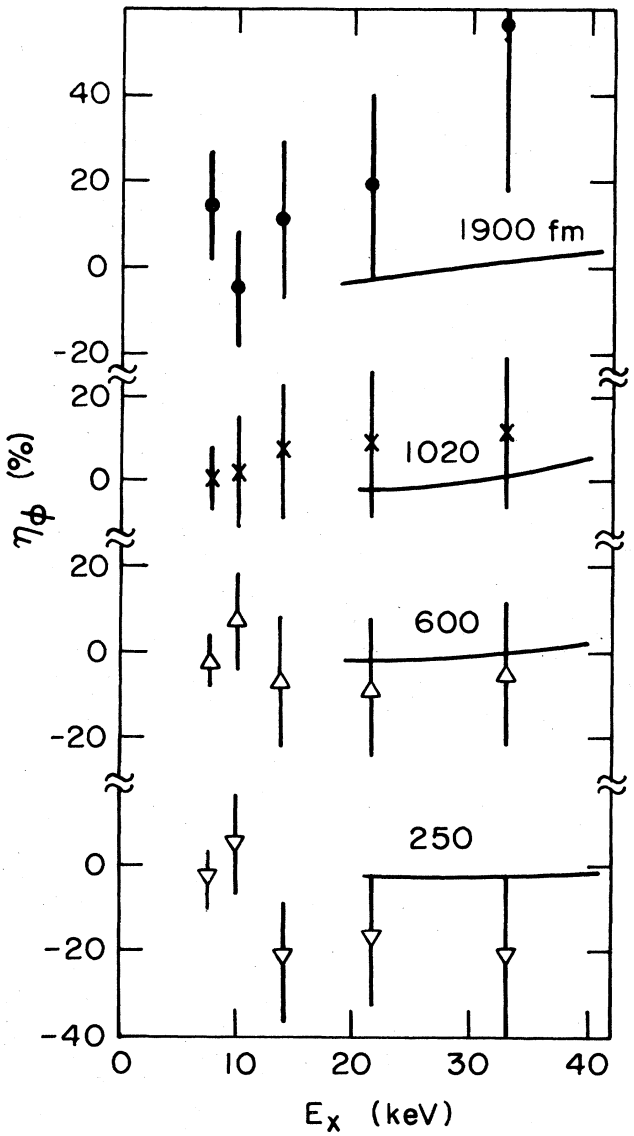

FIG. 46. The azimuthal anisotropy of 90-MeV Ni + Ni MO x rays observed at a polar angle of 90° at several impact parameters in fm (Schuch *et al.*, 1981) compared with theoretical calculations for $1s\sigma$ MO x rays (Anholt, 1982a). For x-ray energies less than 15 keV, $2p\sigma$ MO x rays are seen for which no theoretical calculations have been made.

the rotation of the internuclear axis is slowest, hence where the perfect electron-slip model predicting near-zero anisotropies is less valid. After folding, the absolute value of the azimuthal anisotropy is smaller than 0.1 for all impact parameters. The measured anisotropies are slightly larger than the calculated ones, though the experimental uncertainties are not inconsistent with zero anisotropy. $2p\sigma$ MO x rays are seen for x-ray energies between 10 and 20 keV, and the anisotropy there is also nearly zero, but $2p\sigma$ MO x-ray azimuthal anisotropies have not been calculated. Bürgy *et al.* (1981) found near-zero anisotropies in 20-MeV F + Al and 48-MeV Cl + Cl collisions.

C. Linear polarization measurements

Mokler *et al.* (1980) measured the linear polarization of MO x rays in 1.7-MeV P + Si and 1.3-MeV Mg + Mg collisions at $\theta_{\rm lab}=90°$. To measure the polarization of the 2.7- to 6.17-keV x rays, they used Bragg reflection by a diffracting crystal, Ge(111), LiF(200), or LiF(220). At the Bragg angle, x rays with polarization perpendicular to the crystal scattering plane are scattered by twice the Bragg angle into an x-ray detector, but x rays with polarization parallel to the plane are not. Measuring the scattered x-ray intensity with the crystal plane parallel to and perpendicular to the plane determined by $\mathbf{v}$ and the photon direction $\hat{\mathbf{k}}$ gives the linear polarization, defined as

$$P=\frac{I_{||}-I_{\perp}}{I_{||}+I_{\perp}}\ , \tag{6.9}$$

where $I_{||}$ and $I_{\perp}$ are the x-ray intensities having the polarization parallel or perpendicular to the beam axis.

Polarization measurements are more difficult to make than angular distribution measurements because the emitted x-ray beam must be tightly collimated before scattering from the diffracting crystal, with a consequent loss of counting rate. Also, since the crystal can be used only at a single Bragg angle, a different crystal is required for every x-ray energy measured.

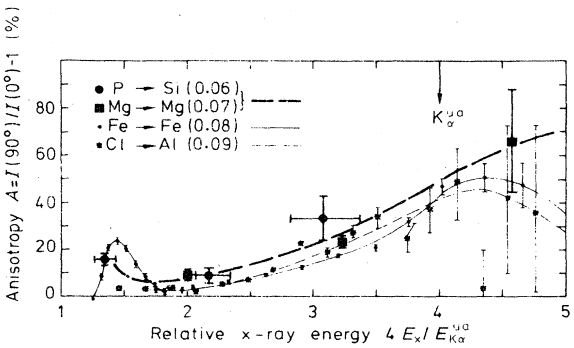

FIG. 47. The anisotropy of MO radiation as a function of the scaled x-ray energy. For Mg + Mg and P + Si the values are converted from linear polarization measurements. The other systems are directly measured anisotropies reported by Stoller *et al.* (1977) and Wölfli *et al.* (Wölfli, Stoller, Bonani, Stöckli, Suter, and Däppen, 1978). The numbers in brackets are the adiabaticity parameters $v/v_{\rm UA}$ (Mokler *et al.*, 1980).

For dipole radiation, the linear polarization is related to the polar angular anisotropy using (Briggs *et al.*, 1979)

$$\eta=\frac{P}{1-P}\ . \tag{6.10}$$

Mokler *et al.* (1980) compared their converted linear polarization measurements with anisotropy measurements in Cl + Al and Fe + Fe collisions, making use of a scaling law similar to that discussed in Sec. V.C. In Fig. 47, the anisotropy spectra are plotted versus reduced x-ray energy $\sim 4v$ in Eqs. (5.11)—(5.13) for nearly constant values of the ratio of the ion velocity to the UA K electron velocity. Holding $v/v_{K\rm UA}$ constant is nearly equivalent to holding q constant if the values of $\zeta=Z_H/Z_L$ are similar. The magnitude of the anisotropies may differ because a different number of projectile vacancies can be brought into the collision, but the shapes should be the same. The linear polarization measurements clearly agree well with the anisotropy measurements, indicating that the continuum x rays are due to dipole radiation.

D. Molecular-orbital x-ray separated-atom K x-ray coincidences

If a $1s\sigma$ vacancy is filled by an electron from the $2p\sigma$ MO during a collision, the resulting $2p\sigma$ vacancy may correlate to the projectile and target K levels where it emits a SA K x ray after the collision. Were it not for the strong Coriolis coupling between the $2p\sigma$ and $2p\pi_x$ MO's, measurements of MO x-ray SA K x-ray coincidences could select just $2p\sigma\rightarrow 1s\sigma$ MO x-ray transitions. However, Coriolis coupling allows contributions from $2p\pi_x\rightarrow 1s\sigma$ transitions early in the collision, followed by the later transfer of the $2p\pi$ vacancy to the $2p\sigma$ MO. In reality, the $2p\sigma$ and $2p\pi_x$ MO's are only basis orbitals with which to describe the 2Σ and 2Π time-dependent MO's. The coincident $1s\sigma$ MO x-ray production probability is given by a coherent sum of radiative amplitudes $\mathbf{D}(b,\omega)$ from the Σ and Π_x MO's, weighted by the amplitudes $a_{\Pi\pi}$ and $a_{\Sigma\pi}$ for the vacancy to go into the $2p\sigma$ MO at the end of the collision (Anholt, 1983):

$$\frac{dP_{\rm MO}^{\rm coin}}{d\omega}\sim|\,\mathbf{D}_{\Sigma}(b,\omega)a_{\Pi\pi}(b)-\mathbf{D}_{\Pi x}(b,\omega)a_{\Sigma\pi}(b)\,|^2 + \frac{dP_{\rm MO}(b,\omega)}{d\omega}P_K(b)\ . \tag{6.11}$$

The last term in this expression is the two-vacancy contribution. A K vacancy can be created independently in a collision where an MO x ray is emitted, giving two vacancies at the end of the collision, one in the SA K shell and the other in any SA shell. The probability of this accidental coincidence (Ford *et al.*, 1981) is the product of the total K-vacancy production probability P_K and the total MO x-ray production probability for $1s\sigma$ MO x rays. (If $2p\sigma$ MO x rays are considered, a different expression for this accidental probability must be used; Vincent

et al., 1985.) The calculated coincident $1s\sigma$ MO x-ray spectrum has about the same shape as the singles spectrum and is a factor of approximately 0.2 smaller for 40-MeV Ni + Ni collisions. The double vacancy probabilities, calculated using extrapolations of measured K-vacancy production probabilities P_K, are factors of ~ 0.07 smaller in 40-MeV Ni + Ni collisions. O'Brien *et al.* (1980) measured approximately identical shapes of coincident and noncoincident continuum spectra in 100- to 200-MeV Nb + Nb collisions, in approximate agreement with the calculations.

The anisotropy of the K coincident MO x rays is much larger than that for the noncoincident MO x rays. In 40-MeV Ni + Ni collisions (Fig. 48), the calculated noncoincident anisotropies are as large as 0.6, but the coincident ones are as large as 6 (Anholt, 1983). When one adds the two-vacancy contributions to the calculated coincident probabilities, smaller anisotropies are obtained, because the anisotropies of the two-vacancy probabilities are equal to the noncoincident anisotropies, of the order of 0.6. Zouros *et al.* (1984) measured higher coincident than noncoincident anisotropies in 40-MeV Ni + Ni collisions, but the coincident anisotropies were lower than the calculations of Anholt (1983). They attempted to subtract the two-vacancy probability from the measured one, to compare their data with calculations including only the first term in Eq. (6.11). The resulting anisotropies agree reasonably well with calculations, though the large anisotropies depend so sensitively on the magnitudes of the measured probabilities that the experimental uncertainties are large.

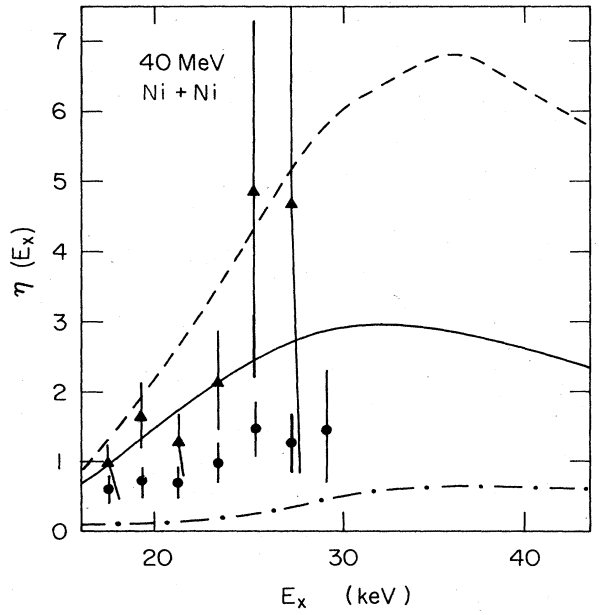

FIG. 48. Measured (Zouros *et al.*, 1984) and calculated (Anholt, 1983) $1s\sigma$ MO x-ray anisotropies for 40-MeV Ni + Ni collisions. The dot-dashed curve shows the noncoincident MO x-ray anisotropies, similar to those shown in Fig. 35. The dashed curve is for SA K x-ray coincident MO x rays, calculated using just the first term in Eq. (6.11). The solid curve and the solid-circle data points are for coincident MO x rays, where the calculations include both terms in Eq. (6.11). Zouros *et al.* subtracted the two-vacancy contribution from their data, obtaining the triangular points, which are in reasonable agreement with the calculations neglecting the two-vacancy contribution (dashed curve).

Coincidences in Pb + Pb collisions have been measured by Vincent *et al.* (1985). Due to the strong $2p\frac{1}{2}$-$2p\frac{3}{2}$ spin-orbit splitting in Pb + Pb quasimolecules, coupling between the σ and π or $p\frac{1}{2}$ and $p\frac{3}{2}$ MO's is small, hence one can in principle measure just $2p\frac{1}{2} \rightarrow 1s\frac{1}{2}$ transitions [$a_{\Pi\pi}=1$ and $a_{\Sigma\pi}=0$ in Eq. (6.11)]. However, contributions from these transitions are small (Kirsch *et al.*, 1978), and since the K-vacancy production probability is near unity in these collisions, one measures only the two-vacancy production contribution for $1s\sigma$ MO x rays. Calculations of the coincident intensity based on measured Pb + Pb MO x-ray and K-vacancy production probabilities agree with experiment, and give additional confirmation of the separation of the measured MO x-ray probabilities into contributions from $1s\sigma$ and $2p\sigma$ MO x rays (Stiebing *et al.*, 1984).

E. Compound-nucleus x-ray emission

Molecular-orbital x-ray measurements are usually made at low projectile energies, where nuclear reactions are not possible and γ-ray background is small. If sufficiently high projectile energies are used so that the projectile and target nuclei merge to form a long-lived compound nucleus (CN), and if a $1s\sigma$ vacancy is present, sharp K x-ray lines characteristic of the UA may be observed. Such x rays have been observed in $p + {}^{106}$Cd (Chemin *et al.*, 1979) and $p + {}^{112}$Sn (Röhl *et al.*, 1981) collisions, from which CN lifetimes of the order of 10^{-18} sec have been deduced. (For a review see Anholt, 1985, and Meyerhof and Chemin, 1985.)

Compound-nucleus and MO x-ray emission must be considered as a single coherent process. If the CN lifetime is very short (approximately zero in the collisions so far considered), only MO x rays are seen. For a long-lived CN the $1s\sigma$ and $2p\pi$ MO's merge into UA $1s\frac{1}{2}$ and $2p\frac{3}{2}$ AO's, so sharp UA $K\alpha_1$ and $K\alpha_2$ lines are observed. The minimum CN lifetime needed to observe UA K x rays must be calculated by considering the interference between CN and MO x rays (Anholt, 1979b).

For a collision in which the projectile and target nuclei stick for a time T, the modified emission amplitude for two-collision MO x-ray production in the dynamic theory of Macek and Briggs (1974; Sec. III.B) is given by

$$\sqrt{2\pi} D_{if}(b,\omega) = \int_{-\infty}^{0} \cdots + \int_{0}^{T} \cdots + \int_{T}^{\infty} dt\, D_{if}[R(t)] \times \exp\left[i \int_{0}^{t} [\omega - \omega_{if}(t')] dt' \right] . \quad (6.12)$$

During the sticking time T, $D_{if}[R(t)]$ and $\omega_{if}(t')$ are constant. Usually the decay of the vacancy during the collision is neglected, because the decay probability Γt_c is small (Γ being the total Auger and radiative transition probability, and t_c the collision time). If Eq. (6.12) is to be used for long-lived compound nuclei where ΓT is large, this term should be included in the calculation of the contribution for $0<t<T$, for which we then have

$$D_{\mathrm{UA}}=\frac{D_{if}(R=0)}{i[\omega-\omega_{if}(0)]-\Gamma_{\mathrm{UA}}/2}[\exp\Delta(T)-1]\ , \quad (6.13)$$

where $\Delta=i[\omega-\omega_{if}(0)]T-\Gamma_{\mathrm{UA}}T/2$. The total emission amplitude is then given by

$$D(b,\omega,T)=\frac{1}{\sqrt{2\pi}}[D_{\mathrm{in}}+D_{\mathrm{UA}}+\exp\Delta(T)D_{\mathrm{out}}]\ , \quad (6.14)$$

where D_{in} and D_{out} are given by

$$D_{\mathrm{out}}=\int_0^\infty dt\, D_{if}[R(t)]\exp\left[i\int_0^t[\omega-\omega_{if}(t')]dt'\right]\ , \quad (6.15)$$

$$D_{\mathrm{in}}=D_{\mathrm{out}}^*\ .$$

In most collisions in which compound nuclei are formed, there will be a distribution of CN sticking times T, the simplest being an exponential distribution with an average lifetime τ. The CN-MO x-ray production probability is averaged over this distribution according to

$$\frac{dP_{\mathrm{CN\text{-}MO}}}{d\omega}\sim\int_0^\infty\frac{dT}{\tau}\exp(-T/\tau)\,|\,D_{if}(b,\omega,T)\,|^2\ . \quad (6.16)$$

Figure 49 shows x-ray emission probabilities in 200-MeV Ni + Ni collisions for various products of the CN lifetime τ and the UA $K\alpha$ transition frequency ω_0. For $\omega_0\tau\approx 0$, only a slowly falling MO x-ray continuum is observed. For longer CN lifetimes the UA x-ray peak builds up until sharp lines are seen for $\omega_0\tau>100$. Similar results have been obtained for one-collision CN-MO x-ray production in Yb + Yb collisions (Anholt, 1979b). In general, the decisive value of $\omega_0\tau$ is approximately 20. For $\omega_0\tau>20$, sufficiently sharp UA x-ray lines are seen, enabling the extraction of CN lifetimes or crude spectroscopic information. This requires that the lifetime τ must be greater than $20/\omega_0=5\times10^{-19}$ sec in Ni + Ni collisions to 5×10^{-20} sec in Yb + Yb collisions.

These results can be understood simply with the Heisenberg uncertainty principle

$$\Delta\omega\tau\approx\frac{\Delta\omega}{\omega_0}\omega_0\tau\approx 1\ . \quad (6.17)$$

If we wish to have a sharp line at the UA transition frequency ω_0, we must have $\Delta\omega/\omega_0\lesssim 0.05$, which requires $\omega_0\tau>20$.

In practice, the observation of CN x rays is limited not by the fundamental minimum lifetime, but by γ-ray background. Due to the large angular momentum brought into heavy-ion nuclear collisions, a copious number of γ rays is produced, which gives a continuum photon distribution far more intense than the MO-CN emission probabilities. Several searches for CN x rays in heavy-ion collisions have been unsuccessful (see Anholt, 1979b, and Meyerhof and Chemin, 1985, for references). A possible indication of CN x-ray emission in 4-MeV/amu Ni + Fe collisions has recently been reported (Chemin *et al.*, 1985).

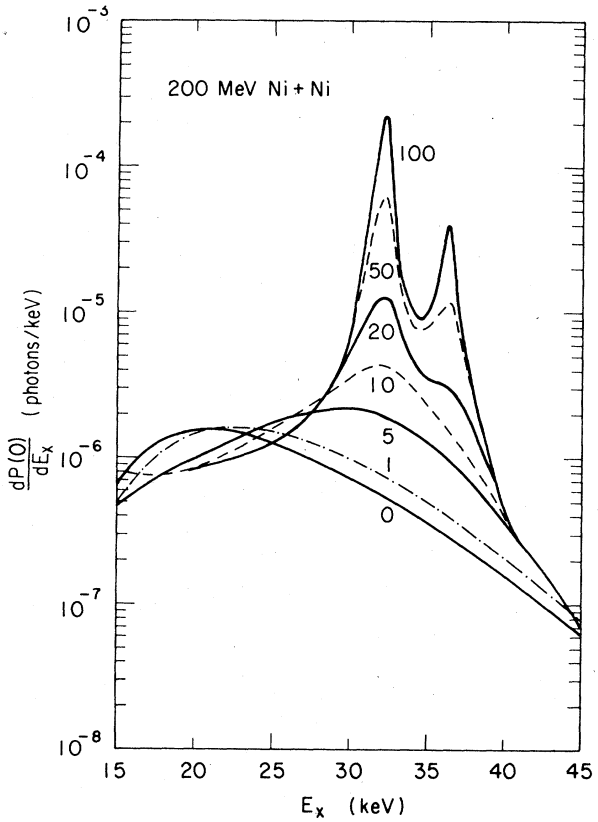

FIG. 49. MO x-ray emission probabilities in 200-MeV Ni + Ni collisions with zero impact parameter, calculated assuming that long-lived compound nuclei with lifetimes τ are formed. The curves were calculated for various products of $\omega_0\tau$, where ω_0 is the UA $K\alpha$ transition frequency (32 keV/$\hbar$).

F. Molecular Auger electron emission

X-ray emission is just one way in which a vacancy in an inner-shell MO can decay during a collision. We have mentioned in the Introduction the possibility of positron emission in special cases like U + U collisions where the $1s\sigma$ binding energy exceeds $2mc^2$. Another more obvious mode of decay is molecular Auger electron emission, wherein an electron in a high-lying MO fills the inner-shell vacancy, and another electron is simultaneously excited into the continuum.

Studies of MO Auger emission are usually made by measuring the spectrum of emitted electrons. The most severe difficulty in these studies is to distinguish MO Auger electrons from secondary electrons excited by radial, rotational, or Coulomb excitation of bound electrons to the continuum. Molecular Auger decay has been investi-

gated in low-velocity collisions where secondary-electron production is hopefully small. Emission from the inner shells in low-Z collisions or the outer shells in high-Z collisions has also been investigated, because x-ray emission is dominant in inner-shell vacancy decay in high-Z atoms, and therefore secondary-electron emission is liable to dominate MO Auger emission in those cases. For example, comparison of MO x-ray emission cross sections in 60-MeV Ni + Ni collisions with the electron emission cross sections for similar photon and electron energies, using an average expected MO UA fluorescence yield, indicates that the observed electron emission cross sections are a factor of ~ 20 too large for molecular Auger emission, and therefore must be primarily due to secondary-electron emission (Bell, Trollmann, Betz, and Spindler, 1982).

The simplest example of MO Auger emission is seen in $He^+ + He$ collisions. In the one-electron correlation diagram [Fig. 50(a)], two electrons can go into the $2p\sigma$ MO and one into the $1s\sigma$ MO during a collision, allowing for a *KLL* MO Auger transition: one $2p\sigma$ electron decays into the $1s\sigma$ MO and the other is excited into the continuum. Such emission was observed indirectly by Barat *et al.* (1972) in ion energy-loss spectra in 1-keV $He^+ + He$ collisions. The interaction responsible for Auger emission is the electron-electron repulsion potential $r_{\alpha\beta}^{-1}$, and the relevant matrix element is given by (Sidis, 1973)

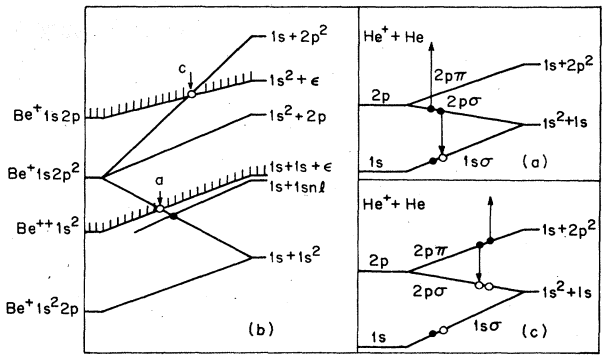

FIG. 50. Correlation diagrams for $He + He^+$ collisions: (a) and (c). Schematic one-electron diagrams showing important MO Auger transitions; (b). A multielectron diagram for $He^+ + He$ collisions adapted from Barat *et al.* (1972).

$$V_\varepsilon[R(t)] = \left\langle 1s\sigma\, 2p\sigma^2 \left| \sum_{\alpha<\beta} \frac{1}{r_{\alpha\beta}} \right| 1s\sigma^2\varphi_\varepsilon \right\rangle , \tag{6.18}$$

where the wave function $|1s\sigma\, 2p\sigma^2\rangle$ denotes the antisymmetrized three-electron wave function for the configuration with one $1s\sigma$ and two $2p\sigma$ electrons. The amplitude for electron emission with energy ε is given in the c.m. system by

$$b_\varepsilon = \int_{-\infty}^{\infty} dt\, V_\varepsilon[R(t)] \exp\left[i \int_0^t [\varepsilon + E_{2p\sigma}(t')] - [E_{1s\sigma}(t') - E_{2p\sigma}(t')]dt' \right] , \tag{6.19}$$

where all energies are assumed to be positive definite. This expression is similar in character to the MO x-ray emission amplitude and can be evaluated using the stationary-phase or Airy-function approximations (Gerber and Niehaus, 1976; Fritsch and Wille, 1979). An oscillatory electron spectrum for constant b or scattering angle is predicted, in fairly good agreement with the data of Barat *et al.* (1972; Sidis, 1973).

Examination of the many-electron $He^+ + He$ correlation diagram [Fig. 50(b)] reveals another way of viewing MO Auger transitions. The molecular *KLL* Auger process considered above can be viewed as the crossing [point a in Fig. 50(b)] with levels correlating to UA electron continuum states built upon the state Be^{2+} $(1s^2)$. At such a crossing, mixing between the $1s\sigma\, 2p\sigma^2$ and $1s\sigma^2\varphi_\varepsilon$ MO's occurs through the matrix element of V_ε. The crossing has a small probability of being avoided, so the wave function goes into the $1s\sigma^2\varphi_\varepsilon$ wave function.

$2p\sigma$-$2p\pi$ rotational coupling creates the possibility that two $2p\sigma$ electrons couple to the $2p\pi$ MO at close internuclear distances, allowing Auger transitions where one $2p\pi$ electron decays back into the $2p\sigma$ MO and the other is promoted into the continuum [Fig. 50(c) or the crossing marked c in Fig. 50(b)]. This process is most evident in $He + He$ and $Li^+ + He$ collisions, where $1s\sigma$ vacancies are not present. Since the $2p\pi$-$2p\sigma$ transition energy is smaller, this Penning-type autoionization process gives Auger electrons with energies close to the SA projectile and target *KLL* Auger lines. This emission has been studied in detail theoretically by Gerber and Niehaus (1976) and Devdariani *et al.* (1977) and experimentally by a number of groups, especially for $Li^+ + He$ collisions (Yagishita *et al.*, 1980; Bordenave-Montesquieu *et al.*, 1982).

Doppler-velocity measurements are an important tool in the study of molecular Auger electrons. Since the Doppler shift is given by the vector sum of the emitter velocity β_{emit} and the Auger electron velocity β_e, the relative Doppler shifts for Auger electrons where $\beta_e \sim \beta_{\text{c.m.}}$ are much greater than for x rays where the photon speed is much greater than $\beta_{\text{c.m.}}$ The angular distribution of MO Auger emission from the quasimolecule is expected to be symmetric around $\theta_{\text{c.m.}} = 90°$. Therefore a transformation with the c.m. emitter velocity that finds a symmetrical c.m. angular distribution is a firm indication of a quasimolecular Auger emission mechanism (Gordeev *et al.*, 1981; Woerlee *et al.*, 1981; Tokoro *et al.*, 1982).

The transformation is somewhat complicated because, near the SA *KLL* Auger line energy, the relevant emitter velocity is the projectile or target-atom velocity, which Doppler-shifts those lines differently. Furune *et al.* (1983) introduced an R-dependent Doppler velocity,

which interpolates smoothly between the c.m. and laboratory emitter velocities. Instead of calculating the c.m.-to-lab transform, they directly calculate the laboratory Auger emission probability in $Li^+ + He$ collisions. Switching functions in molecular translation factors (Delos, 1981) were introduced to accomplish a similar type of interpolation (but for different reasons). The quantitative behavior of molecular switching functions is not yet known, and molecular Auger and x-ray measurements may shed additional light on these quantities (Delos, 1983).

Afrosimov *et al.* (1977) and Gordeev *et al.* (1981) studied continuum electron emission in $Ar^+ + Kr$ and in $Kr^+ + Kr$ collisions. Due to the large number of possible MO's, the question of which Auger transitions take place in these collisions is considerably more complicated than for $He^+ + He$ collisions. By varying the projectile energy and measuring the Auger electron spectrum end point, Afrosimov *et al.* (1977) and Gordeev *et al.* (1981) claim to measure a binding-energy curve which correlates to the UA $4p$ level. Neglecting the binding energy of the electron making the transition into the $4p\pi$ shell, and the initial binding energy of the promoted electron, Gordeev *et al.* conclude that these electrons are due to the filling of $4p\pi$ vacancies. Exponential tails are seen above the end points, due to either collision broadening or secondary-electron production (Woerlee *et al.*, 1981). The significance of the derived binding energies is questionable, though the relative energies may be correct.

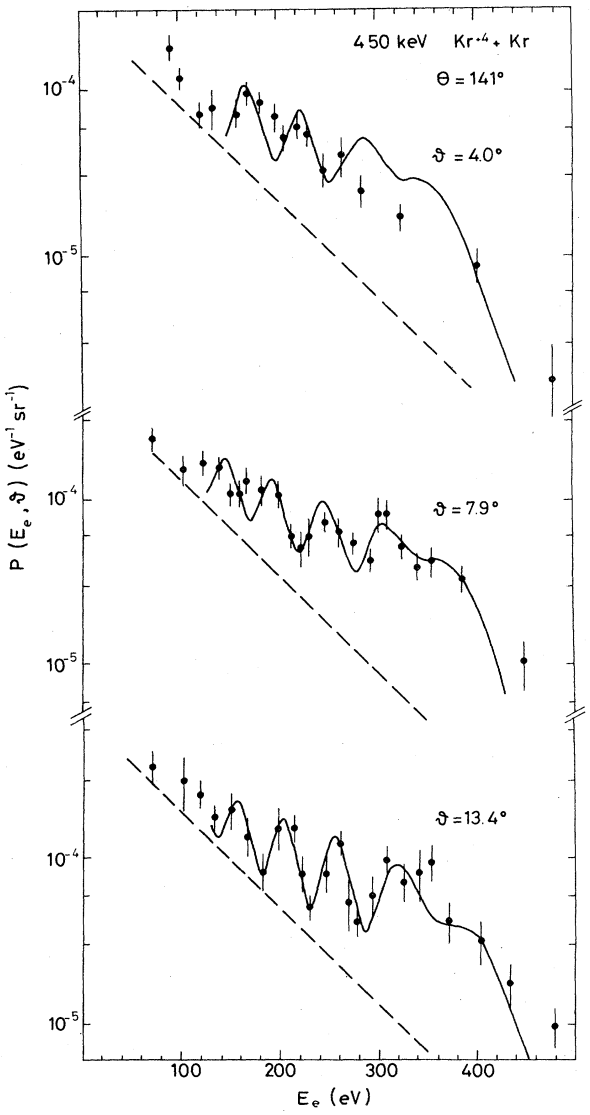

FIG. 51. Electron emission probabilities as a function of the electron energy E_e in 450-keV Kr + Kr collisions at 4.0°, 7.9°, and 13.4° lab scattering angles and an electron observation angle of 141°. The solid lines give the calculated emission probabilities from a superposition of a background due to secondary electrons (dashed lines) and of the molecular autoionization (Liesen *et al.*, 1982).

Liesen *et al.* (1982) measured oscillatory electron emission in 450-keV $Kr^+ + Kr$ collisions at projectile scattering angles between 4° and 13.4° (Fig. 51). The oscillatory behavior is due to the interference between Auger emission on the incoming and outgoing parts of the ion trajectory. The results of Liesen *et al.* suggest that of all possible molecular Auger transitions, one specific transition must dominate to give such pronounced oscillations. If transitions from several different MO's occur, the oscillations would be more smeared out. Liesen *et al.* analyzed the oscillations using an Airy-function approximation [similar to the stationary-phase approximation for MO x rays, Eq. (3.27)]. The fitted spectra allow the deduction of the MO Auger transition energy as a function of internuclear distance. The transition energies seem to agree well with the $4(\frac{3}{2})u$ binding-energy curve calculated using RHFS wave functions by Fricke and Sepp (1981).

VII. CONCLUSIONS

This review has emphasized studies of the mechanism for the production of MO x rays and their emission anisotropies. Such a detailed understanding of MO x-ray production provides a snapshot of a collision in progress. We can deduce which electrons form MO's during a collision, enabling us to formulate a firm condition for MO formation based on the ratio of the ion velocity to the SA electron velocity. We see how the MO's remain aligned in the laboratory frame, ignoring the rotation of the internuclear axis, and how this alignment breaks down partially at low Fourier frequencies (e.g., for $2p\sigma$ MO x-ray production, but less for $1s\sigma$ x-ray production).

Perhaps the most exciting picture to be developed is that of the time development of the amplitude for $1s\sigma$-vacancy production, obtainable from studies of one-collision $1s\sigma$ MO x-ray production. While several theories giving reasonable predictions of $1s\sigma$-vacancy production probabilities and cross sections exist (Andersen *et al.*, 1976; Müller *et al.*, 1978; Anholt, 1980), none of the amplitudes calculated with these theories give correct $1s\sigma$ MO x-ray cross sections. The predicted spectra tend to be flatter than those observed in asymmetric or

high-Z collisions and in gas targets (Thorson and Choi, 1977; Kirsch *et al.*, 1978). In fact, even the cross sections for the production of SA K vacancies by the ionization of $1s\sigma$ electrons are not known exactly in near-symmetric collisions; they usually must be extrapolated from asymmetric collisions as in Fig. 3 or as described by Anholt and Meyerhof (1977). Whether the cross sections vary smoothly with Z_u near $Z_1 \approx Z_2$ or are discontinuous like that sketched in Fig. 3 is not known. One-collision $1s\sigma$ MO x-ray studies bear on the magnitudes of these cross sections.

Mechanisms not yet quantitatively understood are those of L MO x-ray production in collisions like Ag + Ag ($2p\pi$ or $3d\sigma$ MO x rays?), M MO x-ray production in I + Au collisions ($3d\pi$ or $4f\sigma$ MO x rays?), and $4p\pi$ Auger electron production in Kr + Kr collisions. This author makes the following prediction about the outcome of MO x-ray production studies: If one examines the range of possible K, L, and M vacancy-production mechanisms, there are actually only two archetypical ones: "Coulomb excitation" and electron promotion in highly promoted MO's ($2p\sigma$, $3d\sigma$, $4f\sigma$, $5g\sigma$, . . . , excluding $1s\sigma$) followed by vacancy sharing (Meyerhof *et al.*, 1976; Hagmann *et al.*, 1978; Anholt *et al.*, 1978). Coulomb excitation here denotes the process whereby large momentum is transferred from the projectile to a deeply bound electron via the traditional Coulomb excitation mechanism valid for collisions with, say, protons (Merzbacher and Lewis, 1958), or it may involve radial coupling in the MO model. Vacancies are produced in the $1s\sigma$ MO via this mechanism. Electron promotion may involve some momentum-transfer process or may occur as the result of Coriolis coupling or Landau-Zener transitions of vacancies from unfilled SA levels. The highly promoted MO's are loosely bound states near the UA, making electron excitation easy, therefore giving the largest excitation cross sections.

Likewise, there are probably only two (or three) different MO x-ray production mechanisms: MO x-ray emission of vacancies formed in the collision as the result of Coulomb excitation (one-collision $1s\sigma$ MO x rays), and MO x-ray emission on the outgoing part of the collision of vacancies in the highly promoted MO's, formed as the result of electron promotion (e.g., $2p\sigma$ MO x rays). The third two-collision $1s\sigma$ MO x-ray creation mechanism does not fit into either of these two categories well, though it is closer to the second because it involves the formation of a projectile vacancy in a prior collision, but while the outer-shell vacancy transfers into the highly promoted MO at close internuclear distances in the collision (via $2p\sigma$-$2p\pi$ Coriolis coupling for $2p\sigma$ MO x rays, for instance), the projectile K vacancy transfers into the $1s\sigma$ MO at large internuclear distances on the way into the collision, to make two-collision $1s\sigma$ MO x rays. This view agrees with the $3d\sigma$ MO x-ray interpretation of continuum x rays seen in Ag + Ag collisions and the $4f\sigma$ MO x-ray interpretation in I + Au collisions. The $2p\sigma$ MO x-ray production mechanism is archetypical of the highly promoted MO x-ray category. Peaked, positive MO x-ray anisotropies are seen, and peaks in the MO x-ray spectra are seen at low projectile velocities. This process is expected to be dominant for the same reason that the promotion mechanism is the dominant mechanism for the creation of SA x rays in heavy-ion—atom collisions. It is much less difficult to produce a vacancy in the highly promoted MO's.

Our viewpoint in this paper is based on a diabatic view of collisions. Levels cross in the diabatic correlation diagrams, and hydrogenic correlation diagrams are qualitatively superior to Hartree-Fock or many-electron diagrams. In some very low-velocity collisions, however (perhaps 450-keV $Kr^+ + Kr$ or ~1-MeV Xe + Au collisions?), this picture probably breaks down. Given the character change in the wave functions and therefore in the behavior of the radiative and Auger matrix elements near avoided crossings, the breakdown of the diabatic picture may have a striking effect on MO x-ray and Auger spectra.

Finally, the potential for obtaining information about electronic translation factors from Doppler-velocity measurements of MO x rays and Auger electrons is an unexplored facet. An MO electron has, in addition to its velocity relative to the nuclei, a c.m. velocity roughly in the beam direction. As the two nuclei separate, the net velocity changes from the c.m. velocity to that of either the projectile or the target nuclei. Incorporation of this velocity switching into the perturbed stationary states theory is the least well understood aspect of electronic excitation in slow collisions. Though understood formally, the quantitative assessment of the electronic switching functions is not. Such switching may be observable near the SA x-ray and Auger lines by measuring the Doppler velocity of the emitted radiation or electrons. Auger electron measurements are most sensitive to this effect.

ACKNOWLEDGMENTS

This work was supported in part by the National Science Foundation, Grant No. PHY-83-13676. This author enjoyed the hospitality of the Physics Department at the University of Utah while writing this paper. The author thanks H. D. Betz, G. Bissinger, J. Eichler, H. O. Lutz, J. H. Macek, H. Schmidt-Böcking, R. Schuch, and P. Vincent for useful comments and for answering questions about their work. Finally, I would like to thank W. E. Meyerhof for making line-by-line comments on this entire manuscript.

REFERENCES

Afrosimov, V. V., Yu. S. Gordeev, A. N. Sinoviev, A. A. Korotov, and A. P. Shergin, 1978, *Proceedings of the 10th International Conference on the Physics of Electronic and Atomic Collisions, Paris, 1977,* edited by G. Watel (North-Holland, Amsterdam), Vol. 2, p. 924.

Albat, R., N. Gruen, and B. Wirsam, 1975, J. Phys. B **8**, 2520.

Alder, K., A. Bohr, T. Huus, B. Mottelson, and A. Winther,

1956, Rev. Mod. Phys. **28**, 432.
Amusia, M. Ya., 1982, Comments At. Mol. Phys. **11**, 123.
Andersen, J. U., E. Laegsgaard, M. Lund, and C. D. Moak, 1976, Nucl. Instrum. Methods **132**, 507.
Anholt, R., 1976, J. Phys. B **9**, L249.
Anholt, R., 1978a, Z. Phys. A **288**, 257.
Anholt, R., 1978b, Z. Phys. A **289**, 41.
Anholt, R., 1979a, Z. Phys. A **291**, 289.
Anholt, R., 1979b, Z. Phys. A **292**, 123.
Anholt, R., 1979c, Annual Report, Gesellschaft für Schwerionenforschung, unpublished.
Anholt, R., 1980, Z. Phys. A **295**, 201.
Anholt, R., 1981, Phys. Lett. A **84**, 62.
Anholt, R., 1982a, Nucl. Instrum. Methods **198**, 567.
Anholt, R., 1982b, Z. Phys. A **306**, 285.
Anholt, R., 1983, Z. Phys. A **309**, 193.
Anholt, R., 1985, in *Atomic Inner-Shell Physics,* edited by B. Crasemann (Plenum, New York).
Anholt, R., H. H. Behncke, S. Hagmann, P. Armbruster, F. Folkmann, and P. H. Mokler, 1978, Z. Phys. A **289**, 349.
Anholt, R., and W. E. Meyerhof, 1977, Phys. Rev. A **16**, 913.
Anholt, R., and J. O. Rasmussen, 1974, Phys. Rev. A **9**, 585.
Anholt, R., and A. Salin, 1977, Phys. Rev. A **16**, 799.
Anholt, R., and T. K. Saylor, 1976, Phys. Lett. A **56**, 455.
Backe, H., and B. Müller, 1985, in *Atomic Inner-Shell Physics,* edited by B. Crasemann (Plenum, New York).
Bang, J., and J. M. Hansteen, 1959, K. Dan. Vidensk. Selsk. Mat. Fys. Medd. **31**, No. 2.
Barat, M., D. Dhuicq, R. Francois, R. McCarroll, R. D. Piacentini, and A. Salin, 1972, J. Phys. B **5**, 1343.
Barat, M., and W. Lichten, 1972, Phys. Rev. A **6**, 211.
Bates, D. R., K. Ledsham, and A. L. Stewart, 1953, Philos. Trans. R. Soc. London Ser. A **246**, 215.
Bates, D. R., and D. A. Williams, 1964, Proc. Phys. Soc. London **83**, 425.
Behncke, H. H., P. Armbruster, F. Folkmann, S. Hagmann, J. R. MacDonald, and P. H. Mokler, 1978, Z. Phys. A **289**, 333.
Bell, F., H.-D. Betz, H. Panke, E. Spindler, W. Stehling, and M. Kleber, 1975, Phys. Rev. Lett. **35**, 841.
Bell, F., G. Trollmann, and H.-D. Betz, 1982, Phys. Lett. A **88**, 37.
Bell, F., G. Trollmann, H.-D. Betz, and E. Spindler, 1982, Phys. Rev. A **26**, 72.
Bethe, H. A., and E. E. Salpeter, 1957, *Quantum Mechanics of One- and Two-electron Atoms* (Academic, New York).
Betz, H.-D., F. Bell, H. Panke, W. Stehling, E. Spindler, and M. Kleber, 1975, Phys. Rev. Lett. **34**, 1259.
Betz, H.-D., F. Bell, E. Spindler, and M. Kleber, 1976, in *Abstracts of the 2nd International Conference on Inner-shell Excitation,* edited by W. Mehlhorn and R. Brenn (Fakutät f. Physik, Freiburg), p. 11.
Bissinger, G., and L. C. Feldmann, 1973, Phys. Rev. A **8**, 1624.
Bissinger, G., and L. C. Feldmann, 1975, Phys. Rev. Lett. **33**, 1.
Bohr, N., 1948, K. Dan. Vidensk. Selsk. Mat. Fys. Medd. **18**, No. 1.
Bokemeyer, H., *et al.*, 1983, in *Quantum Electrodynamics of Strong Fields,* edited by W. Greiner (Plenum, New York), p. 273.
Bonsen, T. F. M., and L. Vriens, 1970, Physica (Utrecht) **47**, 307.
Bordenave-Montesquieu, A., A. Gleizes, and P. Benoit-Cattin, 1982, Phys. Rev. A **25**, 245.
Briggs, J. S., 1974, J. Phys. B **7**, 47.
Briggs, J. S., and K. Dettmann, 1977, J. Phys. B **10**, 1113.
Briggs, J. S., and M. R. Hayns, 1973, J. Phys. B **6**, 514.
Briggs, J. S., and J. H. Macek, 1972, J. Phys. B **5**, 579.
Briggs, J. S., J. H. Macek, and K. Taulbjerg, 1979, J. Phys. B **12**, 1457.
Bürgy, P., G. Bonani, E. Morenzoni, M. Stöckli, Ch. Stoller, M. Suter, and W. Wölfli, 1981, Z. Phys. A **300**, 105.
Cairns, J. A., A. D. Marwick, J. H. Macek, and J. S. Briggs, 1974, Phys. Rev. Lett. **32**, 509.
Chemin, J. F., S. Andriamonje, J. Roturier, B. Saboya, J. P. Thibaud, S. Joly, S. Plattard, J. Uzureau, H. Laurent, J. M. Maison, and J. P. Shapira, 1979, Nucl. Phys. A **331**, 407.
Chemin, J. F., S. Andriamonje, D. Guezet, J. N. Scheurer, J. P. Thibaud, P. Aguer, F. Hannachi, and J. F. Bruandet, 1985, in *Invited Papers, XIV International Conference on the Physics of Electronic and Atomic Collisions,* edited by D. C. Lorents (North-Holland, Amsterdam) to be published.
Chen, J. C. Y., T. Ishihara, and K. M. Watson, 1975, Phys. Rev. Lett. **35**, 1574.
Chu, T. C., K. Ishii, A. Yamadera, M. Sebata, and S. Morita, 1981, Phys. Rev. A **24**, 1720.
Däppen, W., and W. Baltensperger, 1977, J. Phys. B **10**, 1309.
Davis, C. K., and J. S. Greenberg, 1974, Phys. Rev. Lett. **32**, 1215.
Delos, J. B., 1981, Rev. Mod. Phys. **53**, 287.
Delos, J. B., 1983, private communication.
Devdariani, A. Z., V. N. Ostrovskii, and Yu. N. Sebyakin, 1977, Zh. Eksp. Teor. Fiz. **73**, 412 [Sov. Phys.—JETP **46**, 215 (1977)].
Dunning, T. H., 1970, J. Chem. Phys. **53**, 2833.
Eichler, J., and U. Wille, 1974, Phys. Rev. Lett. **33**, 56.
Eichler, J., and U. Wille, 1975, Phys. Rev. A **11**, 1973.
Eichler, J., U. Wille, B. Fastrup, and K. Taulbjerg, 1976, Phys. Rev. A **14**, 707.
Fano, U., and W. Lichten, 1965, Phys. Rev. Lett. **14**, 627.
Folkmann, F., P. Armbruster, S. Hagmann, G. Kraft, P. H. Mokler, and H. J. Stein, 1976, Z. Phys. A **276**, 15.
Folkmann, F., C. Gaarde, T. Huus, and K. Kemp, 1974, Nucl. Instrum. Methods **116**, 487.
Ford, A. L., J. F. Reading, and R. L. Becker, 1981, Phys. Rev. A **23**, 510.
Frank, W., K.-H. Kaun, and P. Manfrass, 1978, Z. Phys. A **287**, 149.
Frank, W., K.-H. Kaun, P. Manfrass, N. V. Pronin, and Yu. P. Tretyakov, 1976, Z. Phys. A **279**, 213.
Fricke, B., T. Morovic, W.-D. Sepp, A. Rosen, and D. E. Ellis, 1976, Phys. Lett. A **59**, 375.
Fricke, B., and W.-D. Sepp, 1981, J. Phys. B **14**, L549.
Fricke, B., W.-D. Sepp, and T. Morovic, 1984, Z. Phys. A **318**, 369.
Fricke, B., and G. Soff, 1977, At. Data Nucl. Data Tables **19**, 83.
Fricke, B., and J. T. Waber, 1973, Phy. Rev. C **8**, 330.
Fritsch, W., and U. Wille, 1979, J. Phys. B **12**, L335.
Furune, M., F. Koike, and A. Yagshita, 1983, J. Phys. B **16**, 2539.
Garcia, J. D., R. J. Fortner, and T. M. Kavanaugh, 1973, Rev. Mod. Phys. **45**, 111.
Gaukler, G., 1981, Ph.D. thesis (University of Heidelberg).
Gerber, G., and A. Niehaus, 1976, J. Phys. B **9**, 123.
Gerstein, S. S., and V. D. Krivchenkov, 1961, Zh. Eksp. Teor. Fiz. **40**, 1491 [Sov. Phys.—JETP **13**, 1044 (1961)].
Gerstein, S. S., and Ya. B. Zel'dovich, 1969, Lett. Nuovo Cimento **1**, 835.
Gordeev, Yu. S., P. H. Woerlee, H. de Waard, and F. W. Saris,

1981, J. Phys. B **14**, 513.
Gray, T. J., P. Richard, K. A. Jamison, J. M. Hall, and R. K. Gardner, 1976, Phys. Rev. A **14**, 1333.
Greenberg, J. S., C. K. Davis, and P. Vincent, 1974, Phys. Rev. Lett. **33**, 473.
Greenberg, J. S., P. Vincent, and W. Lichten, 1977, Phys. Rev. A **16**, 964.
Greiner, W., and J. Hamilton, 1980, Am. Sci. **68**, 154.
Gros, M., P. T. Greenland, and W. Greiner, 1977, Z. Phys. A **280**, 31.
Gros, M., and W. Greiner, 1975, Z. Phys. A **274**, 165.
Gros, M., B. Müller, and W. Greiner, 1976, J. Phys. B **9**, 1849.
Hagmann, S., P. Armbruster, G. Kraft, P. H. Mokler, and H. J. Stein, 1978, Z. Phys. A **288**, 353.
Hartung, H., and B. Fricke, 1978, Z. Phys. A **288**, 345.
Hartung, H., and B. Fricke, 1979, Phys. Lett. A **71**, 335.
Hartung, H., B. Fricke, T. Morovic, W.-D. Sepp, and A. Rosen, 1979, J. Phys. B **12**, 2193.
Heinig, K. H., H. U. Jäger, H. Richter, and P. Woittennek, 1976, Phys. Lett. B **60**, 249.
Heinig, K. H., H. U. Jäger, H. Richter, P. Woittennek, W. Frank, P. Gippner, K.-H. Kaun, and P. Manfrass, 1977, J. Phys. B **10**, 1321.
Helfrich, K., and H. Hartmann, 1970, Theor. Chim. Acta. **16**, 263.
Hylleraas, E., 1931, Z. Phys. **71**, 739.
Ishii, K., M. Kamiya, K. Sera, S. Morita, and H. Tawara, 1977, Phys. Rev. A **15**, 2126.
Ishii, K., and S. Morita, 1984, Phys. Rev. A **30**, 2278.
Ishii, K., S. Morita, and H. Tawara, 1976, Phys. Rev. A **13**, 131.
Jäger, H. U., 1981, unpublished.
Jäger, H. U., P. Gippner, K. H. Heinig, H. Richter, N. F. Truskova, and H. Woittennek, 1981, J. Phys. B **14**, 701.
Jakubassa, D. H., and M. Kleber, 1975, Z. Phys. A **273**, 23.
Jundt, F., G. Guillaume, P. Fintz, and K. W. Jones, 1976, Phys. Rev. A **13**, 563.
Kaufmann, P., and U. Wille, 1976, Z. Phys. A **279**, 259.
Kaufmann, R. L., J. H. McGuire, P. Richard, and C. F. Moore, 1973, Phys. Rev. A **8**, 1233.
Kessel, Q. C., 1969, in *Case Studies in Atomic Physics I,* edited by E. W. McDaniel and M.R.C. McDowell (North-Holland, Amsterdam), Chap. 7.
Kessel, Q. C., and B. Fastrup, 1973, Case Stud. At. Phys. **3**, 137.
Kienle, P., 1983, in *Quantum Electrodynamics of Strong Fields,* edited by W. Greiner (Plenum, New York), p. 293.
Kienle, P., M. Kleber, B. Povh, R. M. Diamond, F. S. Stephens, E. Grosse, M. R. Maier, and D. Proetel, 1973, Phys. Rev. Lett. **31**, 1099.
Kirsch, J., W. Betz, J. Reinhardt, B. Müller, W. Greiner, and G. Soff, 1979, Z. Phys. A **292**, 227.
Kirsch, J., W. Betz, J. Reinhardt, G. Soff, B. Müller, and W. Greiner, 1978, Phys. Lett. B **72**, 298.
Kissel, L., C. A. Quarles, and R. H. Pratt, 1983, At. Data Nucl. Data Tables **28**, 381.
Kleber, M., and D. H. Jakubassa, 1975, Nucl. Phys. A **252**, 152.
Kraft, G., P. H. Mokler, and H. J. Stein, 1974, Phys. Rev. Lett. **33**, 476.
Kubo, H., F. C. Jundt, and K. H. Purser, 1973, Phys. Rev. Lett. **31**, 674.
Kuhn, H. G., 1934, Philos. Mag. **18**, 987.
Larkins, F. P., 1972, J. Phys. B **5**, 571.
Laubert, R., R. S. Peterson, J. P. Forester, K.-H. Liao, P. M. Griffin, H. Hayden, S. B. Elston, D. J. Pegg, R. S. Thoe, and I. A. Sellin, 1976, Phys. Rev. Lett. **36**, 1574.
Lee, C. M., L. Kissel, R. H. Pratt, and H. K. Tseng, 1976, Phys. Rev. A **13**, 1714.
Lichten, W., 1967, Phys. Rev. **164**, 131.
Lichten, W., 1974, Phys. Rev. A **9**, 1458.
Liesen, D., A. N. Zinoviev, and F. W. Saris, 1982, Phys. Rev. Lett. **47**, 1392.
Lurio, A. L., J. A. Cairns, J. F. Ziegler, and J. H. Macek, 1975, Phys. Rev. A **12**, 498.
Lutz, H. O., W. R. McMurray, R. Pretorius, I. J. van Heerden, R. J. van Reenen, and B. Fricke, 1976, J. Phys. B **9**, L157.
MacDonald, J. R., and M. D. Brown, 1972, Phys. Rev. Lett. **29**, 4.
MacDonald, J. R., M. D. Brown, and T. Chiao, 1973, Phys. Rev. Lett. **30**, 471.
Macek, J. H., and J. S. Briggs, 1974, J. Phys. B **7**, 1312.
Macek, J. H., J. A. Cairns, and J. S. Briggs, 1972, Phys. Rev. Lett. **28**, 1298.
Malkov, E. I., and I. M. Shmushkevich, 1961, Zh. Eksp. Teor. Fiz. **39**, 1837 [Sov. Phys.—JETP **12**, 1282 (1961)].
McDaniel, F. D., J. L. Duggan, P. D. Miller, and G. D. Alton, 1977, Phys. Rev. A **15**, 846.
McMaster, W. H., N. Kerr del Grande, J. H. Mallett, and J. H. Hubbel, 1969, *Compilation of X-ray Cross Sections,* Lawrence Livermore Laboratory Report No. UCRL-50174 (unpublished).
Meron, M., B. M. Johnson, K. W. Jones, R. Schuch, H. Schmidt-Böcking, and I. Tserruya, 1985, Nucl. Instrum. Methods **B10/11**, 64.
Merzbacher, E., and H. W. Lewis, 1958, in *Encyclopedia of Physics,* edited by S. Flügge (Springer, Berlin), Vol. 34, p. 166.
Meyerhof, W. E., 1973, Phys. Rev. Lett. **31**, 1341.
Meyerhof, W. E., 1976, Science **193**, 839.
Meyerhof, W. E., and R. Anholt, 1979, J. Phys. B **12**, 3919.
Meyerhof, W. E., R. Anholt, and T. K. Saylor, 1977, Phys. Rev. A **16**, 169.
Meyerhof, W. E., R. Anholt, T. K. Saylor, S. M. Lazarus, A. Little, and L. F. Chase, Jr., 1976, Phys. Rev. Lett. A **14**, 1653.
Meyerhof, W. E., and J. F. Chemin, 1985, Adv. At. Mol. Phys. **20**, 173.
Meyerhof, W. E., D. L. Clark, Ch. Stoller, E. Morenzoni, W. Wölfli, F. Folkmann, P. Vincent, P. H. Mokler, and P. Armbruster, 1979, Phys. Lett. A **70**, 303.
Meyerhof, W. E., T. K. Saylor, and R. Anholt, 1975, Phys. Rev. A **12**, 2641.
Meyerhof, W. E., T. K. Saylor, S. M. Lazarus, A. Little, B. B. Triplett, and L. F. Chase, Jr., 1973, Phys. Rev. Lett. **30**, 1279; **32**, 502(E).
Meyerhof, W. E., T. K. Saylor, S. M. Lazarus, A. Little, B. B. Triplett, L. F. Chase, Jr., and R. Anholt, 1974, Phys. Rev. Lett. **32**, 1279.
Meyerhof, W. E., and K. Taulbjerg, 1977, Annu. Rev. Nucl. Sci. **27**, 279.
Mokler, P. H., and F. Folkmann, 1978, in *Structure and Collisions of Ions and Atoms,* edited by I. Sellin (Springer, Berlin), p. 201.
Mokler, P. H., S. Hagmann, P. Armbruster, G. Kraft, H. J. Stein, K. Rashid, and B. Fricke, 1975, in *Atomic Physics 4,* edited by G. zu Putlitz, E. W. Weber, and A. Winnacker (Plenum, New York), p. 301.
Mokler, P. H., W. N. Lennard, and I. V. Mitchell, 1980, J. Phys. B **13**, 4607.
Mokler, P. H., H. J. Stein, and P. Armbruster, 1972, Phys. Rev.

Lett. **29**, 827.
Morenzoni, E., G. Bonani, P. Bürgy, Ch. Stoller, and W. Wölfli, 1982, Phys. Lett. A **88**, 131.
Morovic, T., B. Fricke, W.-D. Sepp, A. Rosen, and D. E. Ellis, 1977, Phys. Lett. A **63**, 12.
Mott, N. F., 1931, Proc. Cambridge Philos. Soc. **27**, 553.
Mott, N. F., and H. M. S. Massey, 1965, *The Theory of Atomic Collisions,* 3rd ed. (Oxford University, London).
Müller, B., 1975, in *The Physics of Electronic and Atomic Collisions,* edited by J. S. Risley and R. Geballe (University of Washington, Seattle), p. 481.
Müller, B., 1976, Annu. Rev. Nucl. Sci. **26**, 351.
Müller, B., and W. Greiner, 1974, Phys. Rev. Lett. **33**, 469.
Müller, B., and W. Greiner, 1976, Z. Naturforsch. **31a**, 1.
Müller, B., R. K. Smith, and W. Greiner, 1974, Phys. Lett. B **49**, 219.
Müller, B., R. K. Smith, and W. Greiner, 1975, Phys. Lett. B **53**, 401.
Müller, B., G. Soff, W. Greiner, and V. Ceausescu, 1978, Z. Phys. A **285**, 27.
Mulliken, R. S., 1928, Phys. Rev. **32**, 186.
Northcliffe, L. C., and R. F. Schilling, 1970, Nucl. Data Tables **A7**, 233.
O'Brien, J. J., E. Liarokapis, and J. S. Greenberg, 1980, Phys. Rev. Lett. **44**, 386.
Pratt, R. H., H. K. Tseng, C. M. Lee, L. Kissel, C. MacCallum, and M. Riley, 1977, At. Data. Nucl. Data Tables **20**, 175.
Rafelski, J., L. P. Fulcher, and W. Greiner, 1971, Phys. Rev. Lett. **27**, 958.
Reinhardt, J., G. Soff, and W. Greiner, 1976, Z. Phys. A **276**, 285.
Reinhardt, J., G. Soff, B. Müller, and W. Greiner, 1980, Prog. Part. Nucl. Phys. **4**, 547.
Röhl, S., S. Hoppenau, and M. Dost, 1981, Nucl. Phys. A **369**, 301.
Rosen, A., and D. E. Ellis, 1974, Chem. Phys. Lett. **27**, 595.
Rosen, A., and D. E. Ellis, 1975, J. Chem. Phys. **62**, 3039.
Sakurai, J. J., 1967, *Advanced Quantum Mechanics* (Addison-Wesley, Reading), Sect. 2.4.
Saris, F. W., W. F. van der Weg, H. Tawara, and R. Laubert, 1972, Phys. Rev. Lett. **28**, 717.
Schiff, L. N., 1968, *Quantum Mechanics,* 3rd ed. (McGraw-Hill, New York).
Schmidt-Böcking, H., R. Anholt, R. Schuch, P. Vincent, K. Stiebing, and H. U. Jäger, 1982, J. Phys. B **15**, 3057.
Schmidt-Böcking, H., W. Lichtenberg, R. Schuch, J. Volpp, and I. Tserruya, 1978a, Phys. Rev. Lett. **41**, 859.
Schmidt-Böcking, H., R. Schuch, I. Tserruya, R. Schule, H. J. Specht, and K. Bethge, 1978b, Z. Phys. A **284**, 39.
Schnopper, H. W., H. -D. Betz, J. P. Delvaille, K. Kalata, A. R. Sohval, K. W. Jones, and H. E. Wegner, 1972, Phys. Rev. Lett. **29**, 898.
Schnopper, H. W., J. P. Delvaille, K. Kalata, A. R. Sohval, M. Abdulwahab, K. W. Jones, and H. E. Wegner, 1974, Phys. Lett. A **47**, 61.
Schuch, R., G. Gaukler, G. Nolte, K. W. Jones, and B. M. Johnson, 1980, Phys. Rev. A **22**, 2513.
Schuch, R., H. Schmidt-Böcking, and I. Tserruya, 1981, Phys. Lett. A **82**, 453.
Schuch, R., H. Schmidt-Böcking, I. Tserruya, B. M. Johnson, K. W. Jones, and M. Meron, 1985, Z. Phys. A **320**, 185.
Scofield, J. H., 1969, Phys. Rev. **179**, 9.
Sidis, V., 1973, J. Phys. B **6**, 1188.
Slater, J. C., 1963, *Quantum Theory of Molecules and Solids* (McGraw-Hill, New York), Appendix 1.
Smith, Kent, B. Müller, and W. Greiner, 1975, J. Phys. B **8**, 75.
Smith, R. Kent, B. Müller, W. Greiner, J. S. Greenberg, and C. K. Davis, 1975, Phys. Rev. Lett. **34**, 117.
Spindler, E., H.-D. Betz, and F. Bell, 1977, J. Phys. B **10**, L561.
Spindler, E., H.-D. Betz, and F. Bell, 1979, Phys. Rev. Lett. **42**, 832.
Stiebing, K. E., H. Schmidt-Böcking, W. Schadt, K. Bethge, R. Schuch, P. H. Mokler, F. Bosch, D. Liesen, S. Hagmann, and P. Vincent, 1984, Z. Phys. A **319**, 239.
Stöckli, M., 1979, Ph.D. thesis (ETH-Zurich).
Stöckli, M., and R. Anholt, 1984, Phys. Lett. A **106**, 130.
Stoller, Ch., R. Anholt, and W. E. Meyerhof, 1981, Z. Phys. A **302**, 95.
Stoller, Ch., E. Morenzoni, W. Wölfli, W. E. Meyerhof, F. Folkmann, P. Vincent, P. H. Mokler, and P. Armbruster, 1980, Z. Phys. A **297**, 93.
Stoller, Ch., W. Wölfli, G. Bonani, E. Morenzoni, and M. Stöckli, 1978, Z. Phys. A **287**, 33.
Stoller, Ch., W. Wölfli, G. Bonani, M. Stöckli, and M. Suter, 1977, J. Phys. B **10**, L347.
Taulbjerg, K., and J. S. Briggs, 1975, J. Phys. B **8**, 1895.
Taulbjerg, K., J. S. Briggs, and J. Vaaben, 1976, J. Phys. B **9**, 1351.
Thoe, R. S., I. A. Sellin, M. D. Brown, J. P. Forester, P. M. Griffin, D. J. Pegg, and R. S. Peterson, 1975, Phys. Rev. Lett. **34**, 64.
Thorson, W. R., and J. H. Choi, 1977, Phys. Rev. A **15**, 550.
Thorson, W. R., and H. J. Levy III, 1969, Phys. Rev. **181**, 232.
Tokoro, N., S. Takenouchi, J. Urakawa, and N. Oda, 1982, J. Phys. B **15**, 3737.
Tseng, H. K., R. H. Pratt, and C. M. Lee, 1979, Phys. Rev. A **19**, 187.
Tserruya, I., H. Schmidt-Böcking, R. Schule, K. Bethge, R. Schuch, and H. J. Specht, 1976, Phys. Rev. Lett. **36**, 1451.
Tserruya, I., R. Schuch, H. Schmidt-Böcking, J. Barrotte, W. Da-Hai, B. M. Johnson, M. Meron, and K. W. Jones, 1983, Phys. Rev. Lett. **50**, 30.
Trautvetter, H. P., J. S. Greenberg, and P. Vincent, 1976, Phys. Rev. Lett. **37**, 202.
Vincent, P., 1977, Ph.D. thesis (Yale University).
Vincent, P., 1985, in *Atomic Inner-Shell Physics,* edited by B. Crasemann (Plenum, New York).
Vincent, P., C. K. Davis, and J. S. Greenberg, 1978, Phys. Rev. A **18**, 1878.
Vincent, P., and J. S. Greenberg, 1979, J. Phys. B **12**, L641.
Vincent, P., D. Schwalm, H. Bokemeyer, H. Emling, E. Grosse, and J. S. Greenberg, 1985, unpublished.
Weisskopf, V. F., 1933, Phys. Zeit. **34**, 1.
Woerlee, P. H., Yu. S. Gordeev, H. de Waard, and F. W. Saris, 1981, J. Phys. B **14**, 527.
Wölfli, W., E. Morenzoni, Ch. Stoller, G. Bonani, and M. Stöckli, 1978, Phys. Lett. A **68**, 217.
Wölfli, W., Ch. Stoller, G. Bonani, M. Stöckli, M. Suter, and W. Däppen, 1976, Phys. Rev. Lett. **36**, 309.
Wölfli, W., Ch. Stoller, G. Bonani, M. Stöckli, M. Suter, and W. Däppen, 1978, Z. Phys. A **286**, 249.
Wölfli, W., Ch. Stoller, G. Bonani, M. Suter and M. Stöckli, 1975, Phys. Rev. Lett. **35**, 656.
Wölfli, W., Ch. Stoller, E. Morenzoni, G. Bonani, and M. Stöckli, 1978, in *Superheavy Elements,* edited by M. A. K. Lodhi (Pergamon, New York), p. 429.
Yagishita, A., K. Wakiya, T. Takayanagi, H. Suzuki, S. Ohtani, and F. Koike, 1980, Phys. Rev. A **22**, 118.

Yamadera, A., K. Ishii, K. Sera, M. Sebata, and S. Morita, 1981, Phys. Rev. A **23**, 24.
Zel'dovich, Ya. B., and V. S. Popov, 1972, Usp. Fiz. Nauk **105**, 403 [Sov. Phys.—Usp. **14**, 673 (1972)].
Zener, C., 1932, Proc. R. Soc. London, Ser. A **137**, 696.
Zouros, T. J. M., J. S. Greenberg, and N. Tsoupas, 1984, J. Phys. B **17**, L289.